

THE UNIVERSITY OF CALGARY

**OBSERVATIONS AND TRAJECTORY SIMULATIONS OF
TERRESTRIAL ION OUTFLOW**

by

Christopher M. Cully

A THESIS

**SUBMITTED TO THE FACULTY OF GRADUATE STUDIES
IN PARTIAL FULFILLMENT OF THE REQUIREMENTS FOR THE
DEGREE OF MASTER OF SCIENCE**

DEPARTMENT OF PHYSICS AND ASTRONOMY

CALGARY, ALBERTA

SEPTEMBER, 2001

© Christopher M. Cully 2001



**National Library
of Canada**

**Acquisitions and
Bibliographic Services**

**395 Wellington Street
Ottawa ON K1A 0N4
Canada**

**Bibliothèque nationale
du Canada**

**Acquisitions et
services bibliographiques**

**395, rue Wellington
Ottawa ON K1A 0N4
Canada**

Your file Votre référence

Our file Notre référence

The author has granted a non-exclusive licence allowing the National Library of Canada to reproduce, loan, distribute or sell copies of this thesis in microform, paper or electronic formats.

The author retains ownership of the copyright in this thesis. Neither the thesis nor substantial extracts from it may be printed or otherwise reproduced without the author's permission.

L'auteur a accordé une licence non exclusive permettant à la Bibliothèque nationale du Canada de reproduire, prêter, distribuer ou vendre des copies de cette thèse sous la forme de microfiche/film, de reproduction sur papier ou sur format électronique.

L'auteur conserve la propriété du droit d'auteur qui protège cette thèse. Ni la thèse ni des extraits substantiels de celle-ci ne doivent être imprimés ou autrement reproduits sans son autorisation.

0-612-65098-7

Canada

Abstract

The statistics of thermal-energy O^+ and H^+ observations made by the Akebono satellite are reported, and the contribution of this ion population to the central plasma sheet is examined. The dependence of the total ion outflow rate (fluence) on both solar wind conditions and geophysical conditions is detailed, and the instantaneous temporal variance of this quantity is statistically modelled. Although a clear dependence on solar wind pressure (magnetic or ram) is seen, no significant correlation is found with the clock angle of the Interplanetary Magnetic Field (IMF). The instantaneous fluence is found to be typically within a factor of three of the mean fluence under similar geomagnetic and solar conditions.

The supply of ions to the plasma sheet is shown to be substantial and largely controlled by the electric field. The supply of oxygen ions to the region where substorm activity is thought to originate is shown to depend critically on IMF orientation. It is postulated that the instantaneous response of the “in-transit” oxygen ions to a northward turning of the IMF could potentially act as a substorm trigger.

Acknowledgements

Foremost, I would like to express my deep gratitude to my supervisor and friend, Eric Donovan. His approaches to scientific problems have changed my outlook on science and philosophy, and his unflagging dedication to his work and those around him has been inspirational.

This work would not have been possible were it not for the substantial efforts of a large group of individuals. In particular, Greg Arkos developed and implemented the algorithm for constructing the VDFs presented in section 3.3. Andrew Yau spent countless hours discussing the subtle nuances of interpreting the SMS data, as well as providing a number of specific technical contributions such as the instrument calibration and code for the implementation of spacecraft potential determination. Brian Jackel's scientific insight and skill with computers and numerical methods was a constant encouragement.

The group here at the Institute for Space Research has provided a tremendously fertile work environment, and I would like to thank all those involved. In particular, Leroy Cogger's work to keep it all running and Cliff Marcellus' work with the computers are especially appreciated. Natalya Nicholson, Greg Baker, Johnathan Burchill, Kent Dougall, Brenda Tschanz, Dave Knudsen, Trond Trondsen, Greg Enno and many others have made this a great place to work. I am grateful to Jo-Anne Brown for help with several figures, especially figure 3.4, and to Sandy Murphree and Rita Aggarwala for their thought-provoking comments on this work.

Roughly seven months of my degree were spent in Uppsala, Sweden, as a guest of the Swedish Institute of Space Physics. Their hospitality was exceptional, and I

would like to thank Hermann Opgenoorth and Mats André for the exciting opportunities that working there presented. Frédéric Pitout, Tobia Carozzi, Rico Behlke and Eva Borälv all contributed both to the work I did there and to the good times I had. Miia Riihmaki, Malin Engelmark and especially Annika Lindh welcomed me into their home.

Meghan Blades, Robb Nethery and Dawn Dittman provided a much-needed personal outlet through mountain biking. Paul Kelly and Christen Grow have taught me important lessons in perspective, and Jodie Smith put up with my increasingly nocturnal schedule in the final months of writing. Austen Chongpison, Jennifer MacLeod and Mike Hofer have been there since the very beginning.

Funding has been provided by several sources, and I would like to acknowledge the support of the Canadian Natural Sciences and Engineering Research Council, the Alberta Heritage Scholarship Fund, the Canadian Space Agency, the University of Calgary and the Institute for Space Research. Akebono data has been provided by the Canadian Space Agency; solar wind data is courtesy of NASA through the OMNI program of the National Space Science Data Center.

Most of all, I would like to thank my family for their lifelong support.

Table of Contents

Approval Page	ii
Abstract	iii
Acknowledgements	iv
Table of Contents	vi
1 Introduction	1
1.1 Coordinate Systems, Scale Sizes, and Activity Indices	8
2 Motion of Charged Particles and the Guiding Centre Equations of Motion	12
2.1 Introduction	12
2.2 The Concept of Guiding Center Motion	14
2.3 Electric Fields and the “E Cross B” Drift	17
2.4 Nonuniform Magnetic Fields and the ∇B Drift	23
2.5 First Adiabatic Invariant of the Motion	25
2.6 Example 1: Motion of Particles in the Magnetospheric Equatorial Plane	27
2.7 Example 2: Particle Heating and Faraday’s Law	32
2.8 Example 3: An Alternative Derivation of the ∇B Drift	38
2.9 The Guiding Centre Equations of Motion	40
3 The Suprathermal Mass Spectrometer (SMS) and Initial Data Reduction	42
3.1 The Akebono (EXOS-D) Satellite	42
3.2 SMS Design and Thermal/Suprathermal Mode Operation	44
3.2.1 Aperture and Energy Selector	46
3.2.2 Bennet-type Velocity Selector	47
3.2.3 Energy Analyser and Detector	48
3.3 Construction of Velocity Distribution Functions	49
3.3.1 Spin Plane Count Distribution Functions	51
3.3.2 Differential Flux	54
3.3.3 Adiabatic Correction	55
3.4 Definition of Flux, Unidirectional Flux, Net Fluence and Unidirectional Fluence	57
3.5 Data Selection Criteria and Coverage	59

4	Observations of Ion Outflow from SMS: Statistical Theory and Model Formulation	62
4.1	Characterization of ion outflow	62
4.2	Probability distribution of unidirectional flux	64
4.3	Calculation of Mean Globally-Integrated Fluences	66
4.3.1	Division of the Polar Ionosphere into Regions	68
4.4	Error analysis of fluence estimates: Is there a significant trend?	70
4.4.1	The Bootstrap	71
4.4.2	The Block Bootstrap	73
4.4.3	Trend Analysis in the Fluence Data Using the Block Bootstrap	75
4.5	Calculation of "Instantaneous" Fluence	77
4.5.1	Definition and Detection of Plasma Cells	78
4.5.2	Cell Areas and the Wicksell Problem	80
4.5.3	Cell Shapes	83
4.5.4	Monte Carlo Estimation of Instantaneous Fluence	84
5	Observations of Ion Outflow from SMS: Results	88
5.1	Factors that may affect ion fluence	88
5.2	Global Fluence as a Function of Magnetic and Solar Activity	90
5.2.1	Curve Fit to $F_{10.7}$ and Kp Dependence	95
5.2.2	Dst Dependence	98
5.3	Global Fluence as a Function of Solar Wind Parameters	98
5.3.1	Dependence on IMF Orientation	100
5.3.2	Dependence on IMF Magnitude	101
5.3.3	Dependence on Solar Wind Dynamic Pressure	102
5.4	Seasonal Dependencies of Global Fluence	104
5.5	Summary of results	105
6	Trajectories of Outflowing Ions	107
6.1	Trajectory Tracing Technique	108
6.2	General Characteristics of the Trajectories	109
6.3	Flux at the Plasma Sheet: Dependence on the Form of the Source Velocity Distribution Function	113
6.4	Simulation Method	115
6.5	Ionospheric Flux Seen at the Plasma Sheet	116
7	Discussion and Conclusions	122
7.1	Implications for Magnetospheric Dynamics	122
7.1.1	Mass Budget: Is this an Important Plasma Population?	122
7.1.2	Geophysical Dependencies: What Controls the Supply?	123

7.1.3	Dynamic Responses: Possible Substorm Connections	125
7.1.4	A Conjecture	126
7.2	Evaluation of the Source Model	128
7.2.1	Comparison with Other Reported Measurements	128
7.2.2	Strengths and Weaknesses	130
7.3	Evaluation of the Tracing Model	131
7.3.1	Comparison with Other Reported Results	131
7.3.2	Strengths and Weaknesses	131
7.4	Main Conclusions	132
7.5	Directions for Further Study	133

List of Tables

3.1	Physical SMS parameters needed for differential flux calculation. . . .	55
4.1	Characteristics of the net O ⁺ flux distribution.	66
4.2	Regional boundaries for fluence analysis.	69
5.1	List of some external factors which may affect global fluence.	89
5.2	Regional dependence of upward fluence for low Kp.	95
5.3	Regional dependence of upward fluence for high Kp.	96
5.4	Coefficients of best fit for fluence as a function of Kp and F _{10.7}	97
5.5	Seasonal dependence of fluence.	105
5.6	Observed factors affecting unidirectional fluence.	106
7.1	Effective CPS particle supply Earthward of the distances indicated. .	126

List of Figures

1.1	A dipole magnetic field.	1
1.2	Schematic view of the magnetosphere	4
1.3	The northern hemisphere in geomagnetic coordinates.	9
1.4	The $F_{10.7}$ flux as a function of time.	11
2.1	Helical trajectory in a uniform magnetic field ($\vec{E} = 0$).	16
2.2	Arbitrary helix-like trajectory and the motion of its guiding center.	16
2.3	Trajectory of a positively charged particle subject to $\vec{E} \times \vec{B}$ drift.	22
2.4	Magnetic lines of force in the noon-midnight meridian of the Earth's magnetosphere.	29
2.5	Contour plot of magnetic field strength in the Earth's equatorial plane.	30
2.6	Particle trajectories in the equatorial plane.	33
2.7	Electric field in the moving frame.	36
3.1	The Akebono satellite.	42
3.2	Schematic view of the SMS instrument.	45
3.3	The efficiency of the microchannel plate detector as a function of time.	50
3.4	Flowchart for constructing velocity distribution functions from the SMS data.	52
4.1	Histograms of measured O^+ net flux values	65
4.2	Polar cap regional boundaries for differing Kp conditions.	68
4.3	Performance of the block bootstrap on synthetic data.	74
4.4	Some trends in the SMS data, with errors from block bootstrap.	76
4.5	Cellular structure seen in the SMS data.	80
4.6	"Unfolding" the chord length distribution to a diameter distribution.	82
4.7	Conditional probability of flux given cell size.	86
5.1	Relationship between Kp and upward O^+ and H^+ fluence for both solar minimum and solar maximum conditions.	91
5.2	Relationship between Kp and net fluence.	92
5.3	Regional dependence of upward O^+ and H^+ fluence, as a function of Kp and $F_{10.7}$	94
5.4	Dst dependence of the upward O^+ and H^+ fluence.	99
5.5	O^+ fluence as a function of interplanetary magnetic field strength.	102
5.6	Dependence of H^+ and O^+ fluence on solar wind dynamic pressure.	103

6.1	Electric potential contour plot of the high-latitude ionosphere under southward IMF conditions, using the Weimer [1995] model.	110
6.2	Trajectory of typical CPS-populating H ⁺ and O ⁺ ions	111
6.3	Locations, energies and pitch angles of O ⁺ ions that will eventually reach the plasma sheet near $(x, y)_{GSM} = (-10, 2)R_E$	114
6.4	Supply of ionospheric H ⁺ to the CPS.	118
6.5	Supply of ionospheric O ⁺ to the CPS.	119

Chapter 1

Introduction

The magnetic field in the region of space around the Earth owes its origin to electric currents flowing within the Earth, in the Earth's atmosphere, and in outer space. The internal sources produce a magnetic field which, looked at on the scale size of several times the Earth's radius, is roughly dipolar. Higher order multipole terms are certainly present, and result from the finite spatial extent of the internal currents, as well as the magnetic effects of large ferromagnetic objects in the crust. Figure 1.1 shows the field lines from an appropriate dipole. If no other electric currents were present in the Earth's vicinity then the magnetic field topology in the region of space around the Earth would be roughly that indicated by this model.

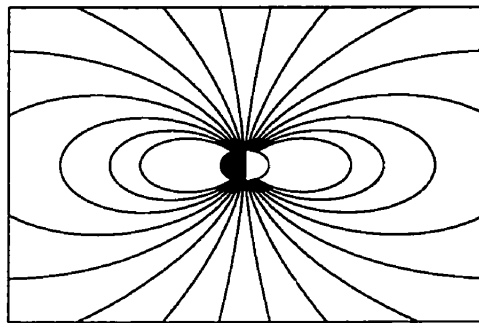


Figure 1.1: A dipole magnetic field.

The existence of the *solar wind* was inferred on the basis of observations of sudden changes of the magnetic field measured on the surface of the Earth [Chapman and Ferraro, 1932], observations of the ionic comet tails [Hoffmeister, 1943; Biermann,

1951], and theoretical studies of the physics of the solar atmosphere [Parker, 1958], and later confirmed through numerous *in situ* observations. The solar wind is a gas of electrons and ions, predominantly ionized hydrogen, with much smaller amounts of singly and doubly ionized helium and other heavier ionic constituents. It is formed by the constant (though highly variable) outward expansion of the solar corona into interplanetary space. At the Earth's orbit, solar wind speeds, densities and temperatures are highly variable. Typical values of the speed ranges from several hundred to over a thousand km/sec, densities range from one to more than 30 particles per cubic centimeter, and temperatures are on the order of 10^5 degrees Kelvin (corresponding to typical electron and proton characteristic energies of several eV). Magnetic flux in the solar wind plasma obeys the *frozen in* criterion [Nicholson, 1983]. Thus, the solar wind plasma entrains magnetic flux from the corona, carrying it outward through the interplanetary medium. This is the *interplanetary magnetic field*, or IMF, and has typical magnitudes of several to tens of nanoTeslas.

Due to the fact that the frozen in condition holds in the solar wind plasma, the terrestrial magnetic field presents an obstacle to solar wind flow. The Earth's field carves out a cavity in the solar wind, forming a region of space that we call the Earth's *magnetosphere*. The magnetosphere is traditionally defined to be the region of space in which the terrestrial magnetic field dominates the motion of charged particles [Gold, 1959]. For practical reasons, it is preferable to use a somewhat modified definition, such as "the region of space which is threaded by magnetic field lines that can *reasonably* be traced back to the Earth" [Donovan, 1993].

Figure 1.2 is a schematic diagram of the magnetosphere. Based on the nature of plasma populations, and the magnetic field topology, it is useful to recognize mag-

netospheric regions. Several of these are of particular interest in terms of my thesis work. The *central plasma sheet* (CPS) contains an ion population of several to tens of KeV and an electron population of hundreds of eV to several KeV, on *closed magnetic field lines*. CPS field lines cross the *neutral sheet* at roughly their most distant point from the Earth. The neutral sheet is the location of the smallest radius of curvature of field lines in the CPS, and the lowest magnetic field strengths. In a magnetosphere that is north-south symmetric, the neutral sheet is also the *magnetic equatorial plane*. The *tail lobes* are threaded by *open magnetic field lines*, and are populated mostly by a non-energetic plasma population (the picture is actually a bit more complicated, as the details of the lobe plasma population actually depend on the direction of the solar wind magnetic field). Solar wind plasma enters the magnetosphere through the *cusps*, and at locations along the *magnetopause* where the *magnetosheath* magnetic field is relatively antiparallel to the adjacent magnetospheric field¹. Typical number densities in the CPS and lobe are 1/cc and 0.1/cc, respectively. The magnetic field in the magnetosphere is the sum of the terrestrial field, and the field due to differential charged particle motion in the magnetosphere. The magnetic topology, field strength, and *all* of the plasma parameters vary significantly on time scales ranging from seconds (*sudden storm commencements*), to minutes (*substorms*), to hours and days (short term solar wind variations), and ultimately over years (the eleven year *solar cycle*).

The boundary between the solar wind (actually the *magnetosheath*, which consists of shocked solar wind plasma) and the magnetosphere is the *magnetopause*. In general, this boundary is both easily defined, and easily identified in data from

¹Entry is also possible through *grad B capture* (see, e.g. Baumjohann and Treumann [1987])

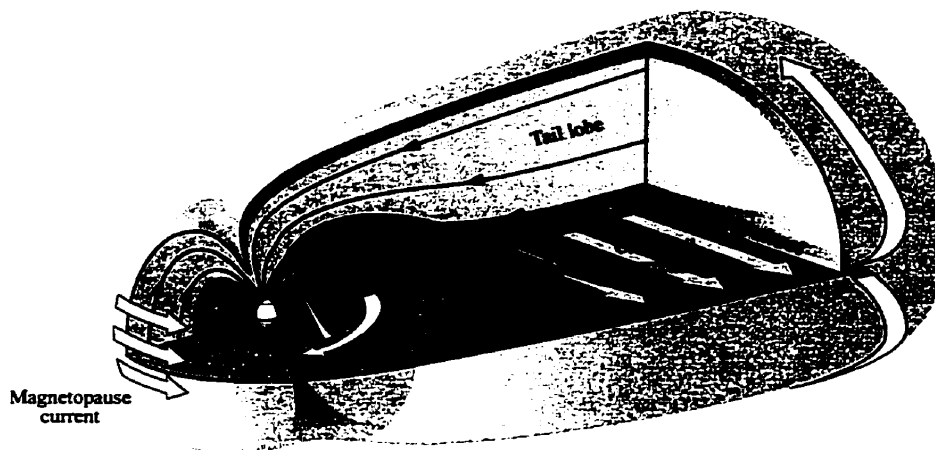


Figure 1.2: Schematic view of the magnetosphere, courtesy of Dr. J. Teemu T. Mäkinen, Finnish Meteorological Institute.

satellite crossings. The low altitude boundary of the magnetosphere is not so easily defined, however. For my purposes, it is reasonable to think of the magnetosphere as terminating in the terrestrial *ionosphere*. The ionosphere is the region of space (roughly between 95 and 500 or more kilometers), where ionized particles are present in sufficient quantity to affect radio wave propagation [Rishbeth and Garriott, 1969]. At least on the sun-lit side of the Earth, this ionization is created by solar Extreme Ultraviolet (EUV) and Ultraviolet (UV) radiation. On the night side, the ionization is a combination of residual ionization from the day side and ionization due to collisions resulting from the precipitation of magnetospheric particles (i.e. due to *auroral* processes).

The magnetosphere is a dynamic system. Energy input to the magnetosphere from the solar wind drives electric currents in the ionosphere (causing Joule heating) and heats the plasma sheet population. The power delivered by the solar wind often

outstrips the power dissipated, and this excess energy causes changes in the magnetospheric topology. One of these changes is an increase in the magnetic field strength in the lobes, and a corresponding thinning of the plasma sheet and enhancement of the cross-tail current that flows through the CPS. This *magnetotail stretching* usually takes place during times when the IMF is directed antiparallel to the terrestrial field (i.e. during times of *southward IMF*). These periods can last minutes, hours, or even days. Northward turnings of the IMF shut off this stretching, and often result in a violent collapse of the ability of the CPS to carry the cross-tail current. The current diverts along magnetic field lines and through the ionosphere. There are a number of dramatic consequences of this, including a transient brightening of the aurora, significant heating of the ionosphere, significant energization of magnetospheric plasma, and a return of the overall magnetospheric configuration to a more “relaxed” state. This cycle of growth and explosive breakdown of the cross-tail current, and return to a lower energy magnetospheric configuration, is called the *magnetic substorm*. The details of how the energy is initially stored in the magnetosphere, exactly how the current carrying capacity of the CPS breaks down, and how the system recovers are topics of intense study in space physics.

Temperatures vary systematically throughout the magnetosphere. In the *mantle* and lobes, the temperature of the ion population is $\sim 10^6$ degrees Kelvin, while in the CPS it is $\sim 10^7$ degrees Kelvin. Throughout the magnetosphere, the electron temperature is lower than the ion temperature by a factor of roughly two [Lui, 1987]. At roughly 1000 degrees Kelvin (~ 0.1 eV), ionospheric temperatures are significantly lower than those in the magnetosphere. It is customary to refer to the ionospheric plasma as being *thermal*, and the magnetospheric plasma as being

energetic. Furthermore, ionospheric processes often impart energy to a significant fraction of the ionospheric ions, creating a *suprathermal* population of several to tens of eV ions. Ionospheric ions in the energy range corresponding to ionospheric temperatures have characteristic speeds that are typically lower than, but on the order of, escape velocity. For example, a 1eV proton has a speed of 14 km/sec, which is greater than escape velocity (which is ~ 11 km/sec). As a consequence of the suprathermal ion population, there is an ever present (though highly variable and hard to quantify) flux of escaping ionospheric ions. Some of these are drawn upwards by the electric field created by escaping *photoelectrons*², in a process referred to as the *polar wind* [Axford, 1968]. Some acquire excess energy due to heating that results from microphysical processes associated with the aurora, flowing upwards with characteristic *conic* distributions [Ungstrup et al., 1979].

Magnetospheric plasma must originate within either the solar wind or the ionosphere. Historically, the solar wind has been viewed as the only significant source of energetic plasma in the magnetosphere. This has been supported by observations of composition (eg., Sharp et al. [1982]) and correlations between solar wind and CPS number density (eg., Borovsky et al. [1998]). On the other hand, observations of significant amounts of KeV He⁺ and O⁺ ions in the CPS, which cannot have come from the solar wind, demonstrated that at least some of the time, the ionosphere can contribute to the energetic magnetospheric population [Shelley et al., 1972; Chappel et al., 1987]. At present, the issue of whether the ionosphere contributes significantly to the magnetospheric plasma is unresolved. This is a difficult question to answer

²Photoelectrons are electrons that have been stripped from a neutral atom by an energetic photon (usually UV or EUV).

decisively, both from an observational and a theoretical point of view. Difficulties with answering this question observationally stem from the fact that, for example, an ionospheric proton and a solar wind proton can easily end up in the near-Earth magnetotail with comparable energies. All relevant energies are also difficult to observe. The mechanism by which solar wind particles enter the magnetosphere is not entirely clear and is the subject of current research programs. The details of ionospheric outflow, particularly at lower energies, are sketchily known, at best. Theoretical approaches to answering this question are limited by how well we understand the electrodynamic environment of the near-Earth space and the microphysics related to processes that accelerate and heat ionospheric particles and that lead to the trapping of both ionospheric and solar wind particles in the magnetosphere.

My objective in carrying out my thesis work was to explore the contribution of ionospheric plasma to magnetospheric dynamics. I approached this problem in two stages. The first was to use a large data base of observations of thermal and suprathermal upflowing ions, at altitudes ranging from 6 000 to 10 000 kilometers, obtained during the flight of the Canadian Suprathermal Mass Spectrometer (SMS) on board the Japanese Akebono spacecraft to *characterize the ionospheric source.* The second was to use that information as input to a *test-particle simulation of charged particle motion in the magnetosphere,* to determine the characteristics and flux of ionospheric-origin ions at the neutral sheet.

1.1 Coordinate Systems, Scale Sizes, and Activity Indices

As is the case in all fields of science, space physics has a vocabulary that one must come to terms with. Distances in the magnetosphere are generally expressed in terms of Earth Radii (R_E). The *subsolar point* is roughly $10 R_E$ from the Earth, and the cross-section of the magnetosphere is roughly $40 R_E$ in diameter, though these quantities can vary significantly as a consequence of solar wind pressure, temperature, and magnetic field variations. The *magnetotail* is drawn away from the Sun, parallel to the solar wind, roughly along the *Sun-Earth line*. The angle between the axis of the magnetotail and the Sun-Earth line is determined by the solar wind speed (typically 400 km/sec) relative to the orbital speed of the Earth (roughly 30 km/sec), and hence is typically 4° . As the solar wind speed can fall to values of 200 km/sec and often exceeds 800 km/sec , this angle varies accordingly. There are several coordinate systems that are commonly used in order to report, for example, the locations of relevant satellite observations. One of these is the Geocentric Solar Magnetospheric (GSM) system. The GSM X-axis is the sun-Earth line, with positive being towards the sun. The Z-axis is chosen so that the north dipole magnetic pole (defined by the orientation of the centred dipole moment of the terrestrial magnetic field) lies in the X-Z plane. By north, I mean that the positive Z-direction is towards the geographic northern hemisphere. The Y-axis is then determined by completing the right hand Cartesian system. The Earth rotates inside of the magnetospheric cavity, and the Y-GSM axis points along the *dawn-dusk* line, with positive Y pointing towards the dusk side. Generally speaking, southward IMF corresponds to the IMF vector having a negative Z-component in the GSM system.

Locations in the ionosphere are typically reported in terms of *geomagnetic coordinates*. This is a natural consequence of the dominant role of the terrestrial magnetosphere in ionospheric electrodynamic and auroral processes. Several magnetic coordinate systems are in wide use today. All of these have been developed to take advantage of the topology of the magnetic field due to sources inside the Earth, and for their utility in terms of ordering data from space science observations. One widely used example is the PACE coordinate system [Baker and Wing, 1989]. Locations in this coordinate system are quoted in *magnetic latitude*, and *magnetic local time* (MLT). Figure 1.3 is a map of the northern hemisphere with constants of magnetic latitude and MLT overlaid. Space physical processes at locations with common geomagnetic latitude are expected to have similar phenomenology. For example, the aurora is most commonly observed at geomagnetic latitudes from $\sim 65^\circ$ to $\sim 70^\circ$.

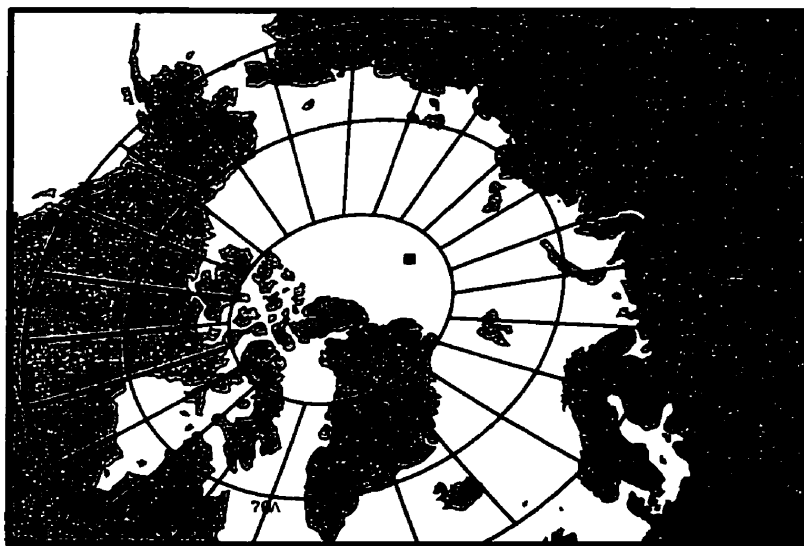


Figure 1.3: The northern hemisphere in geomagnetic coordinates. The geographic and geomagnetic north poles are marked.

In order to facilitate statistical studies, and the comparison of data obtained at different times, a number of numerical indicators of magnetospheric activity have been developed by the space science community. Two examples are *Kp* and *Dst*. The *Kp*, or *planetary index*, is derived from ground-based magnetic field measurements from a number of mid-latitude observatories. The data from these stations is used to identify how active the sources of the magnetic field fluctuations are, with numbers ranging from 0 (for virtually no activity) to 9 (for extreme activity). The *Kp* index is a three hour average over all stations. The *Dst* index is also derived from measurements from a (different) network of mid-latitude magnetic observatories. In this case, the horizontal (i.e., parallel to the Earth's surface) component of the magnetic field from all the contributing stations is averaged, over a one hour period. The index is then reported in nT (nanoTesla). Large negative deviations of *Dst* (on the order of -50 nT to -100 nT or more) indicate enhanced magnetic fields due to magnetospheric current systems. These magnetic field deviations are often due to an increased ring current, and usually indicate magnetic storms that result from sustained periods (tens of hours) of enhanced solar wind dynamic pressure. A summary of magnetic indices, their appropriate use, and some of their pitfalls, can be found in Rostoker [1972].

Variations in solar EUV flux have a significant impact on the state of the ionosphere. As well, these variations correlate rather well with solar activity. The EUV flux is larger during *solar maximum* and smaller during *solar minimum*, and varies systematically throughout the 11 year solar cycle. A simple but effective means of characterizing the EUV flux has been developed by Canadian solar researchers. This involves measuring the 10.7 cm radio flux, at the Earth, three times daily, with a

calibrated receiver and a specific radio dish. The so-called $F_{10.7}$ cm flux is one of the most widely used quantitative indicators of solar activity. The index has been reliably recorded for more than the last fifty years. A time series of the $F_{10.7}$ cm flux is plotted in figure 1.4.

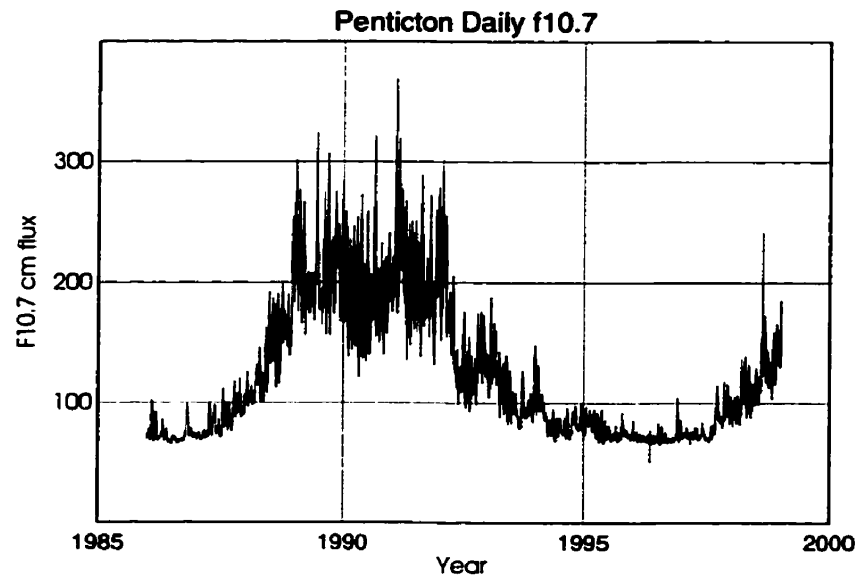


Figure 1.4: The $F_{10.7}$ flux as a function of time.

Chapter 2

Motion of Charged Particles and the Guiding Centre Equations of Motion

2.1 Introduction

A plasma is an ionized gas (see Chen [1984] for a more complete definition of a plasma). While it is true that most plasma research focuses on the collective behavior of the particles that make up a plasma, it is often instructive to consider the motion of individual charged particles in background magnetic and electric fields. In many cases, a good understanding of these motions can facilitate insight into the collective behavior of the plasma. This is certainly true in many situations that arise in plasmas in the Earth's upper atmosphere, the magnetosphere and the solar wind.

Studies of individual particle motion in the Earth's magnetosphere provide us with valuable information about a number of interesting processes in the near-Earth space environment. For example, the northern lights or *aurora borealis* are produced by energetic electrons and protons moving down magnetic lines of force into the Earth's ionosphere where they collide with, and collisionally excite, ionospheric ions and neutral atoms and molecules. The ions and neutrals give off photons as they relax to their ground states. The collective luminosity due to this process is the visible aurora. The protons and electrons that rain down on the ionosphere are known as *precipitating* particles. In order to understand where the precipitating

particles come from and how they are energized, one must have an understanding of their trajectories in the region of space around the Earth. The work presented in this thesis involves the interpretation of data and particle simulations relevant to the escape of positive ions (namely protons and O^+) from the upper atmosphere, and their contribution to magnetospheric plasmas. It was thus necessary for me to develop computational techniques that would allow me to deal appropriately with the trajectories of these ions in the complicated electric and magnetic fields that permeate the near-Earth magnetosphere. In turn, this required the development and implementation of appropriate model electric and magnetic fields, as well as methods for simulating the trajectories of charged particles in those fields. I did not attempt to develop self-consistent electromagnetic fields and plasmas, although some aspects of the process of terrestrial ion outflow are best treated in such a fashion. Rather, I restricted my attention to ions that are (hopefully) at altitudes that are high enough that collisions are unimportant in their motions, and carry out “test-particle” simulations, in pre-specified empirical electric and magnetic fields. Furthermore, I also restricted my attention to parts of trajectories during which the so-called “guiding centre approximation” holds.

Providing certain conditions are satisfied, by invoking the guiding center approximation [Alfvén, 1950], one can greatly simplify the problem of determining the trajectory of a charged particle in complicated electric and magnetic fields. The most important of these required conditions is that the electric and magnetic fields do not vary significantly over time and spatial scales on the order of the particle gyroperiod and gyroradius, respectively. In such cases, we say that the “guiding center approximation holds”, and that the motions of the particles are “adiabatic”. In this

case, the particle motion can be thought of as being comprised of a (nearly) circular gyro-motion about, and a “drift” of, the “guiding center”. In the guiding center equations of motion, the details of the gyro-motion are replaced by terms involving the kinetic energy of the particle in a frame moving with the guiding center. These are truly gyro-averaged equations of motion.

In this chapter, I introduce the concept of guiding center motion, with some simple examples to illustrate the idea of “drifts”. I conclude the chapter with a statement of the complete guiding center equations of motion, without derivation. Using the guiding center approximation to simulate particle trajectories typically involves two levels of assumption. The first is that the relevant fields satisfy the guiding center approximation for the relevant particles, and must hold true if one is to use this approach meaningfully. The second level of approximation is to neglect some of the terms in the full guiding center equations, and is predicated on the fact that these are typically negligible in comparison with the other, more commonly used terms.

2.2 The Concept of Guiding Center Motion

The simplest field configuration that I consider is a uniform magnetic field with no applied electric field. The force on a particle moving in this field is given by the Lorentz force equation

$$\vec{F} = q(\vec{E} + \vec{V} \times \vec{B}) \quad (2.1)$$

where in this case, $\vec{E} = 0$. Since the force is perpendicular to the velocity, no work

can be done on the particle, so the energy and therefore the speed is constant. Since \vec{B} is also constant, the force is constant in magnitude and normal to the direction of motion. Therefore, the particle moves in a circle that is in a plane orthogonal to \vec{B} . The radius of this circle is given by the Larmor radius,

$$R_L = \frac{mV_{\perp}}{|q|B} . \quad (2.2)$$

Here, V_{\perp} indicates the magnitude of the part of the velocity vector that is perpendicular to the magnetic field. Now, if the initial velocity has a non-zero component parallel to the magnetic field, then since there is no force in this direction, the velocity in this direction is constant. The resulting trajectory is a helix, as shown in figure 2.1.

This motion can be thought of as the superposition of two motions:

$$\vec{X} = \vec{X}_c + \vec{X}_{GC} \quad (2.3)$$

where \vec{X}_c is the location of the particle in its circular motion about the magnetic line of force and \vec{X}_{GC} is the position of the center of this circle, known as the guiding center. In this particular case, \vec{X}_{GC} follows a straight line. In general, any arbitrary trajectory can be decomposed in this same manner; one term represents circular motion about the guiding center and another term represents the motion of the guiding center itself. Figure 2.2 shows a much more complicated trajectory (where $\vec{E} \neq 0$) with its guiding center.

In many applications, trajectories of interest are typically much longer than the Larmor radius. For example, in the Earth's magnetosphere, one might be interested

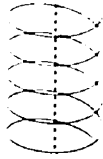


Figure 2.1: Helical trajectory in a uniform magnetic field ($\vec{E} = 0$).

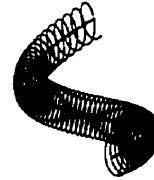


Figure 2.2: Arbitrary helix-like trajectory and the motion of its guiding center.

in tracing the trajectory of an electron with a gyroradius of as little as a few meters over a distance of many Earth radii. In these types of situations, \vec{X}_c is of little importance; a small oscillation about the position of the guiding center can be ignored relative to the large motion of the guiding center itself and one can still understand the important details of the particle's motion. Moreover, it is most often the case that the trajectory of the guiding center is much simpler than the trajectory of the particle. For example, in the case of a uniform magnetic field and no electric field, the guiding center trajectory is a straight line rather than a helix. Of course, if the actual particle trajectory does not somewhat resemble a helix, then the trajectory of the guiding center is no simpler than that of the particle, and the guiding center approach is of little practical value. This will happen if the electric or magnetic fields change significantly over the course of one "gyration".

What is found from a careful derivation of the guiding center motion in arbitrary field configurations (see Northrop [1963]) is that to a very good approximation, the motion can be described by a small number of forces acting parallel to the local magnetic field and a small number of drifts that move the particle in a direction

perpendicular to the magnetic field. In this chapter I will discuss two such drifts. The first is the $\vec{E} \times \vec{B}$ drift which occurs in orthogonal electric and magnetic fields. The second is the ∇B drift which occurs in magnetic fields where there is a gradient in the strength of the field orthogonal to the field direction.

2.3 Electric Fields and the “E Cross B” Drift

In section 2.2, I talked about motion in a uniform magnetic field. I would like to move towards a description that is valid for more complicated fields. The first step is to introduce a uniform electric field, in addition to the uniform magnetic field. In typical plasmas, charged particles have much more mobility parallel to the magnetic lines of force than perpendicular to them. For example, the guiding center of a particle in a uniform magnetic field with $\vec{E} = 0$ is constrained to a single magnetic line of force (field line) while being free to move with arbitrary velocity along that line. One consequence of this directionally limited mobility is that, in plasmas, magnetic lines of force can often be treated as equipotentials. Thus, for many situations of interest in plasma physics, the electric field can be treated as everywhere perpendicular to the magnetic field.

Consider the case where the magnetic field is uniform in the positive \hat{z} direction and the electric field is uniform in the positive \hat{x} direction. What will be the trajectory of a charged particle in this field configuration? There are several approaches that can be used to answer this question. One interesting approach is to ask if there is a moving reference frame in which the electric field is zero. In this moving frame, the force acting on the particle would simply be the magnetic force. If this is a

nonrelativistic transformation, then the magnetic field in the moving frame is just the magnetic field in the original (rest) frame. Since that magnetic field is uniform, the particle's trajectory in the moving frame would be the helix discussed in section 2.2. A simple transformation would then give the particle's trajectory in the rest frame.

In the non-relativistic case, the electric field in a moving frame is given by

$$\vec{E}' = \vec{E} + \vec{U} \times \vec{B} \quad (2.4)$$

where \vec{U} is the velocity of the primed frame relative to the unprimed frame¹. With the field configuration

$$\begin{aligned} \vec{E} &= E\hat{x} \\ \vec{B} &= B\hat{z}, \end{aligned} \quad (2.5)$$

I would like to find, if possible, a velocity such that \vec{E}' is zero. In mathematical form:

$$E\hat{x} + \vec{U} \times B\hat{z} = 0. \quad (2.6)$$

Clearly, equation 2.6 is satisfied if \vec{U} is in the $-\hat{y}$ direction and has magnitude E/B . Thus the electric field is zero in the frame moving with velocity \vec{U} , where \vec{U} is perpendicular to both the electric and magnetic fields in the rest frame and has magnitude E/B .

¹For the relativistic formulation, see Jackson [1975]

More generally, I can consider any situation in which there is a uniform electric field perpendicular to a uniform magnetic field. In order for the electric field in a moving frame to be zero, then

$$\vec{E} + \vec{U} \times \vec{B} = 0. \quad (2.7)$$

If this is true, then certainly the following is as well:

$$(\vec{E} + \vec{U} \times \vec{B}) \times \vec{B} = 0. \quad (2.8)$$

I can rearrange this to obtain

$$\vec{U} = \frac{\vec{E} \times \vec{B}}{B^2} + (\vec{U} \cdot \hat{b})\hat{b} \quad (2.9)$$

where \hat{b} is the unit vector in the direction of the magnetic field. Expressing the velocity of the moving frame as the sum of two vectors, one parallel to and the other perpendicular to the magnetic field:

$$\vec{U} = \vec{U}_\perp + \vec{U}_\parallel \quad (2.10)$$

where \vec{U}_\parallel is equal to the product of the component of \vec{U} in the direction of the magnetic field and \hat{b} :

$$\vec{U}_\parallel = (\vec{U} \cdot \hat{b})\hat{b}. \quad (2.11)$$

Thus, equation 2.9 gives the following relation for \vec{U}_\perp :

$$\vec{U}_\perp = \frac{\vec{E} \times \vec{B}}{B^2}. \quad (2.12)$$

The electric field is therefore zero in any reference frame moving with a velocity \vec{U} , provided the part of this velocity that is perpendicular to the magnetic field satisfies equation 2.12. There is no constraint imposed upon the component of \vec{U} in the direction parallel to \vec{B} . In particular, the electric field is zero in the reference frame that is moving with a velocity $\vec{U} = \vec{U}_\perp + \vec{V}_\parallel$, where \vec{V}_\parallel is the velocity of the guiding center in the direction of the magnetic lines of force (in this case, a constant):

$$\vec{U} = \frac{\vec{E} \times \vec{B}}{B^2} + \vec{V}_\parallel. \quad (2.13)$$

As an aside, the electric field in the moving frame does not depend on \vec{U}_\parallel (see equation 2.4). Thus, it is not surprising that requiring the electric field to be zero in the moving frame only constrains \vec{U}_\perp .

In the last paragraphs, I have shown that in the situation where there is orthogonal uniform electric and magnetic fields, there exists (in the nonrelativistic limit) a frame moving in a direction orthogonal to both the electric and magnetic fields in which the electric field is zero. The trajectory of any particle, when analyzed in this moving frame, is just that of a charged particle moving in a uniform magnetic field. This motion, of course, is the helical motion discussed in section 2.2. Moreover, I am free to choose the component of the frame's velocity parallel to the magnetic field to be equal to the particle's velocity in this direction (as in equation 2.13). In this case, the helix becomes a simple circle and the frame moves at exactly the velocity of the guiding center. In this situation, it is easy to picture the motion in the rest frame as being the combined motion of the guiding center (which is moving with the velocity \vec{U}) and an *exactly* circular motion about the guiding center. The motion of

the guiding center is the $\vec{E} \times \vec{B}$ drift:

$$\vec{V}_{\vec{E} \times \vec{B}} = \frac{\vec{E} \times \vec{B}}{B^2} \quad (2.14)$$

plus some (constant) velocity parallel to the magnetic field. An interesting feature of this drift is that it is independent of both charge, mass and (in the nonrelativistic case) the kinetic energy of the particles. As well, the $\vec{E} \times \vec{B}$ drift is obviously orthogonal to the electric field. As I will discuss in the following paragraph, as the particle gyrates about the guiding center it gains and loses energy due to work being done by the electric field. However, the motion of this particle averaged over many gyrations is the guiding center motion. This is orthogonal to the electric field and hence, on average, the particle neither gains, nor loses, kinetic energy. In fact, if the particle's motion is only due to the $\vec{E} \times \vec{B}$ drift, then its guiding centre trajectory is an equipotential.

One can gain insight into the reason why this drift occurs by considering the motion of the particle in the rest frame. Figure 2.3a shows one “gyration” of a particle in uniform crossed electric and magnetic fields. The magnetic and electric fields point out of and towards the top of the page, respectively. There is a systematic variation of the radius of curvature of the trajectory. The average radius of curvature is larger above the horizontal axis than below it. The net result is that, after one gyration, the particle intercepts the x-axis a small distance to the right. This motion repeats over and over (see figure 2.3b) and the average motion of the particle is to the right (this is the drift). Most textbook treatments of the $\vec{E} \times \vec{B}$ drift ascribe the variation in radius of curvature to a variation in the local Larmor radius due

to changes in the particle's kinetic energy [Nicholson, 1983, e.g.]. This is not quite correct. If there is an electric field present, then the local radius of curvature of the particle's trajectory is *not* in general equal to the Larmor radius. Counterexamples include the standard freshman physics example of a velocity *selector* or *filter* (e.g. Lea and Burke [1997]). In this case, the particle trajectory is a straight line (ie. infinite radius of curvature), yet it is definitely an example of an $\vec{E} \times \vec{B}$ drift in a situation with a finite Larmor radius.

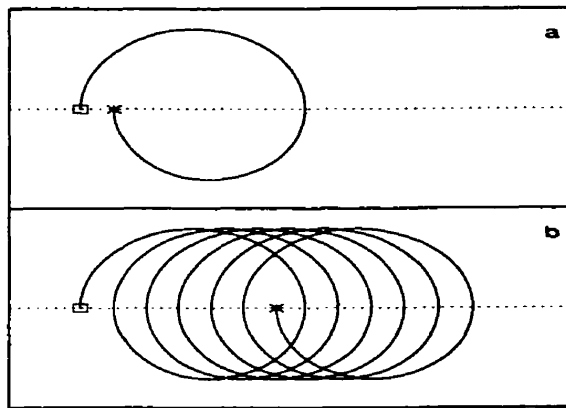


Figure 2.3: Trajectory of a positively charged particle subject to $\vec{E} \times \vec{B}$ drift. The electric field is directed towards the top of the graph and the magnetic field out of the page. Panel (a) shows the path followed over one “gyration”; panel (b) shows the path over six “gyrations”. The drift is the “gyro-averaged” motion to the right in the figures. The drift arises as a result of a systematic variation of the radius of curvature of the trajectory over a gyration. The radius of curvature increases in the direction of the electric field for positive charges, as shown here, and decreases in that direction for negative charges. Positive and negative charges orbit in opposite directions in the magnetic field. The result is that the $\vec{E} \times \vec{B}$ drift is in the same direction for both positive and negative charges.

2.4 Nonuniform Magnetic Fields and the ∇B Drift

There are other reasons why the radius of curvature of the trajectory might vary systematically in some direction. Consider the case where the magnetic field is given by

$$\vec{B} = (B_o + \alpha y)\hat{z} \quad (2.15)$$

so that there is a gradient in the magnetic field strength orthogonal to the magnetic field direction. For simplicity, set $\vec{E} = 0$. In this situation, the radius of curvature is the Larmor radius. Since the Larmor radius depends inversely on the magnetic field strength, there is again qualitatively the same type of situation as caused the $\vec{E} \times \vec{B}$ drift. Here, the Larmor radius decreases in the direction of the gradient in the magnetic field strength (∇B). The guiding center motion, called the gradient drift or the “grad-B” drift, is thus orthogonal to ∇B . The ∇B drift velocity can be calculated approximately by using a perturbation technique (see Jackson [1975]; Nicholson [1983]; Chen [1984]). The drift velocity found is

$$\vec{V}_{\nabla B} = \frac{\varepsilon_{\perp}}{qB} \frac{\vec{B} \times \nabla B}{B^2} \quad (2.16)$$

where B is magnetic field strength and ε_{\perp} is that part of the particle’s kinetic energy in a frame moving with the guiding center. In other words, this is the part of the kinetic energy that can be ascribed to the *nearly* circular motion about the guiding center. This expression for the drift velocity is only valid in situations where the magnetic field does not change appreciably during one gyration of the particle. In turn, in a particular magnetic field, this expression is valid only if the Larmor radius

of the particle in question, and hence its kinetic energy, is *small enough*.

There is no exact analytic solution to the equation of motion of a charged particle moving in such a magnetic field. This drift velocity is approximate, rather than exact as was the case for the $\vec{E} \times \vec{B}$ drift. The particle motion in a frame moving at the ∇B velocity is nearly circular. In the case of the $\vec{E} \times \vec{B}$ drift, the motion about the guiding center is *exactly* circular. Also unlike the $\vec{E} \times \vec{B}$ drift, the ∇B drift velocity depends on the charge to mass ratio of the particle, as well as its kinetic energy.

I now have expressions for the velocities of the $\vec{E} \times \vec{B}$ and ∇B drifts. What happens in the situation where there are orthogonal electric and magnetic fields *and* there is a gradient in the magnitude of the magnetic field? Although I will not attempt a proof of this here, it turns out if the conditions assumed in the derivation of each drift are met, then the combined drift can be found by a simple vector addition of the $\vec{E} \times \vec{B}$ and ∇B drifts [Northrop, 1963].

In more complicated field configurations, other drifts can arise as well. Some of the other drifts include curvature drift and polarization drift. Curvature drift arises when the charged particle has a finite gyroradius and component of velocity along a magnetic field which is locally curved, and charged particles undergo polarization drift in orthogonal magnetic and electric fields if the electric field in the particle's frame of reference changes in time. While it is more complicated to do so, these other drifts can also be understood in terms of gradients in the Larmor radius that are perpendicular to the local magnetic field. For a complete analysis of these and other drifts, see Northrop [1963] or Kruskal [1965a,b].

2.5 First Adiabatic Invariant of the Motion

The study of particle motion in complicated electric and magnetic fields is often made much simpler if one employs the concept of invariants of the motion. In particular, there are quantities referred to as “adiabatic” invariants. In the current context, an adiabatic invariant is a quantity that, when averaged over a number of gyroperiods, is conserved during the motion of the particle². In cases where this applies, trajectories can often be found simply by requiring conservation of this quantity, without the need for integrating the equations of motion at all. The most commonly used adiabatic invariant is the so-called “first” adiabatic invariant. There are derivations illustrating the conservation of this particular quantity in numerous texts and articles [Northrop, 1963; Kruskal, 1965a,b; Kelley, 1989]. In this section, I will present a derivation that is unique and instructive in that it leads directly from the equations expressing the $\vec{E} \times \vec{B}$ and ∇B drift velocities to an expression that clearly shows that the particle is constrained to move along contours of constant first adiabatic invariant.

Consider a particle moving in a field configuration such that the motion of the guiding center can be described by the sum of the $\vec{E} \times \vec{B}$ drift and the ∇B drift:

$$\vec{V}_{\text{drift}} = \frac{\vec{E} \times \vec{B}}{B^2} + \frac{\varepsilon_{\perp}}{qB} \frac{\vec{B} \times \nabla B}{B^2} . \quad (2.17)$$

Now, since the magnetic force does not do work on the particle, the total energy of the particle is

$$\varepsilon = -q\phi' + \varepsilon_o \quad (2.18)$$

²Adiabatic invariants can be much more general than this (see, e.g., Goldstein [1980]), but this definition suffices in the current context.

where ε is the kinetic energy, ϕ' is the electrical potential relative to the initial position and ε_o is the initial kinetic energy. Furthermore, since there are no forces acting along the magnetic field lines, the kinetic energy parallel to the line remains constant, so that

$$\varepsilon_{\perp} = -q\phi' + \varepsilon_{\perp o}. \quad (2.19)$$

If the zero point of the electric potential is now re-defined so that $\phi = \phi' - \varepsilon_{\perp o}/q$ then $\varepsilon_{\perp} = -q\phi$ and equation 2.17 can be rewritten as:

$$\vec{V}_{\text{drift}} = \frac{\vec{B} \times \nabla \phi}{B^2} - \frac{\phi \vec{B} \times \nabla B}{B^3}. \quad (2.20)$$

Then, using the fact that $\nabla B = -B^2 \nabla \frac{1}{B}$,

$$\begin{aligned} \vec{V}_{\text{drift}} &= \frac{1}{B^2} \left\{ \vec{B} \times \nabla(\phi) + B[\phi \vec{B} \times \nabla \left(\frac{1}{B} \right)] \right\} \\ &= \frac{1}{B} \left\{ \frac{\vec{B} \times \nabla(\phi)}{B} + \phi \vec{B} \times \nabla \left(\frac{1}{B} \right) \right\}. \end{aligned} \quad (2.21)$$

Finally, using $\nabla(\phi/B) = (1/B)\nabla\phi + \phi\nabla(1/B)$,

$$\vec{V}_{\text{drift}} = \frac{1}{B} \vec{B} \times \nabla \left(\frac{\phi}{B} \right). \quad (2.22)$$

Therefore, the direction of motion of the particle is always perpendicular to $\nabla(\phi/B)$, so that ϕ/B is a constant of the motion. Since the kinetic energy (ie., ε_{\perp}) is proportional to the potential, it follows that the quantity

$$\mu = \frac{\varepsilon_{\perp}}{B} \quad (2.23)$$

is also a constant of the motion. It can be easily shown [Nicholson, 1983] that the magnetic moment of this gyrating charged particle is equal to μ , which is the so-called “first” adiabatic invariant:

$$\mu = \text{constant.} \quad (2.24)$$

Although it was derived above incorporating only the $\vec{E} \times \vec{B}$ and ∇B drifts, the invariance of μ holds in much more general conditions [Northrop, 1963; Kruskal, 1965a; Kelley, 1989].

2.6 Example 1: Motion of Particles in the Magnetospheric Equatorial Plane

In this section, I will present an example of particle motion in simplified fields where this motion can be completely determined by invoking conservation of the first adiabatic invariant. This particular example is widely used in magnetospheric physics and, as I will point out at the beginning of the next section, can be used to explain some observed properties of the magnetospheric plasma and the aurora.

In some circumstances, no detailed knowledge of the particle’s motion about the guiding center is needed and an understanding of the trajectory of the guiding center is sufficient. For example, a 1 keV electron located roughly 10 Earth radii from the Earth on the nightside of the magnetosphere will have a gyroradius on the order of 5 km. If one is interested in how this particle moves around in a system that is tens of R_E in extent, then these small gyrations can often be ignored. In the previous section, I showed that μ is conserved during the motion of the particle, provided the

conditions necessary for the ∇B drift are satisfied. In many situations of physical interest, this allows an extremely efficient way of determining particle trajectories. If the motion under consideration can be constrained in another, independent way (for example, if a second invariant of the motion can be found or if the motion is constrained to a plane), then the trajectory of the guiding center can be obtained simply by tracing out a locus of points that is everywhere orthogonal to the gradient in μ and follows the other constraint. The motion of charged particles in the Earth's magnetosphere provides an excellent example of the use of such a technique.

As stated above, I will use conservation of the first adiabatic invariant to examine one type of particle trajectory in the terrestrial magnetosphere. This will require models of both the electric and magnetic fields in the region of interest. One numerical model of the magnetospheric magnetic field that is widely used in space physics research is the Tsyganenko model [Tsyganenko, 1987]. Figure 2.4 shows magnetic lines of force, calculated using the Tsyganenko model, in the “noon-midnight meridional plane”, which is the plane that contains the Earth's magnetic axis and the Sun-Earth line. In this diagram, the solar wind arrives from the right and stretches the Earth's magnetic field out into a long tail. The “magnetic equatorial plane” is orthogonal to the Earth's magnetic axis (and contains the sun-Earth line). The magnetic field is everywhere orthogonal to this plane. Figure 2.5 shows a contour plot of the strength of the Tsyganenko model magnetic field in the magnetic equatorial plane.

Although the magnetospheric electric field can be difficult to observe, the task is somewhat simpler at lower altitudes. Fortunately, as discussed in section 2.3, magnetic lines of force can be treated as electric equipotentials. This allows the

projection of ionospheric potential models (e.g. Volland [1978]; Weimer [1995]) into the magnetosphere. In the tail, the electric field in the magnetic equatorial plane is generally in the dawn-dusk direction, does not vary greatly in strength over much of the plane and typical values of this strength are $\sim 10^{-4}$ V/m.

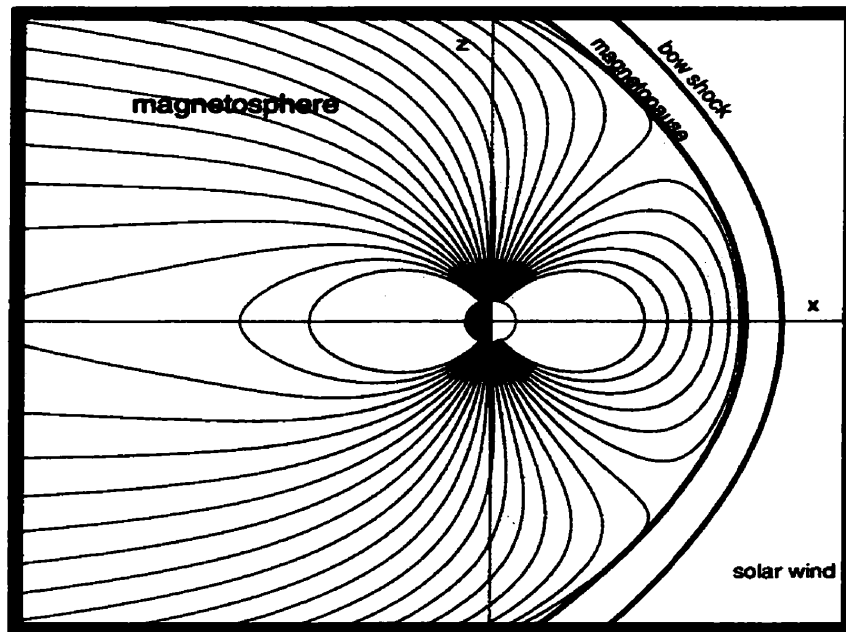


Figure 2.4: Magnetic lines of force in the noon-midnight meridian of the Earth's magnetosphere. These “field lines” were integrated using the Tsyganenko magnetic field model. The vertical axis is parallel to the Earth's magnetic axis. North is upward in this figure and corresponds to the positive z direction (see text). The sun-Earth line is the horizontal axis. This is the x -axis (see text), with \hat{x} pointing towards the sun.

For the remainder of this chapter, I will confine my attention to the motion of charged particles in the magnetic equatorial plane. Based on the information in the

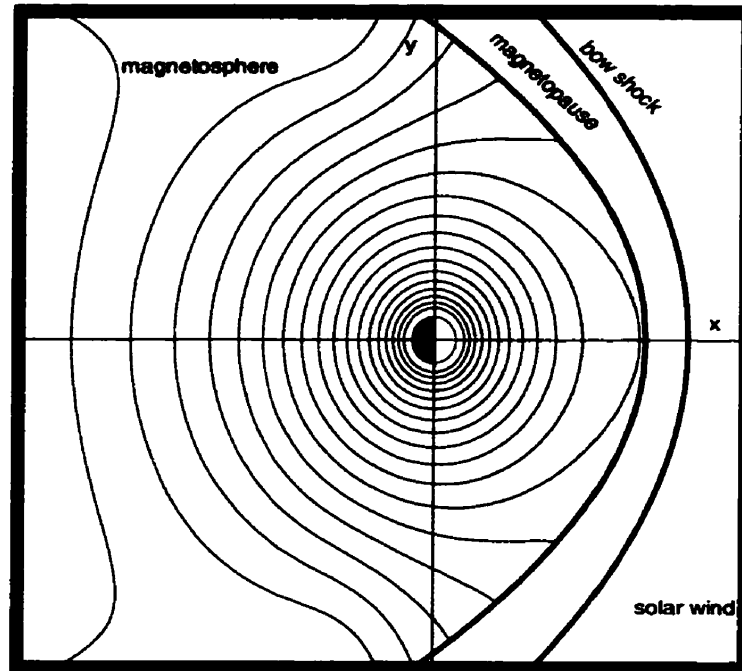


Figure 2.5: Contour plot of magnetic field strength in the Earth's equatorial plane, according to the Tsyganenko magnetic field model. The spacing of the contours is logarithmic: the magnetic field falls off roughly with the third power of the radial distance from the Earth in the equatorial plane. The horizontal axis is the sun-Earth line, which is the x -axis referred to in the text. The vertical axis is the dawn-dusk axis, which is the y -axis referred to in the text. The view is from above the north magnetic pole, looking "down" on the Earth. The day and night sides of the Earth are indicated by the shading in the circle, which represents the Earth. The magnetospheric electric field discussed in the text is in the dawn-dusk direction and is directed towards the top of the figure. The ∇B drift is orthogonal to the gradient in the strength of the magnetic field. Consequently, it is tangent to contours of constant magnetic field strength.

previous paragraph, I have a usable model of the electric and magnetic fields in this plane. The magnetic field is everywhere normal to the plane, with the strength given by the Tsyganenko model. I will take the electric field to be constant in strength, perpendicular to the magnetic field (ie, in the plane) and pointing in the dawn-dusk direction. In Geocentric Solar Magnetospheric (GSM) coordinates (at times of 0 dipole tilt) the direction of the magnetic vector is the \hat{z} direction (ie., $\vec{B} = B\hat{z}$). The electric field is directed so that $\vec{E} = E\hat{y}$. Thus, in the equatorial plane, with the simplistic electric field model described above, electric equipotentials are straight lines parallel to the x -axis.

Consider a particle moving in the equatorial plane with no component of its velocity normal to the plane. For a wide range of initial conditions (ie., kinetic energy and position), its motion can be described by the vector sum of the $\vec{E} \times \vec{B}$ and ∇B drifts. Since both of these drifts involve a cross product with \vec{B} (see equations 2.14 and 2.16), and since \vec{B} is normal to the plane, the motion of the particle will be in the equatorial plane.

The only force that does work on the particle is the electrostatic force. The particle's kinetic energy ε in the electric field is, therefore,

$$\varepsilon = \varepsilon_o + qE(y - y_o) \quad (2.25)$$

where E is the electric field strength, y is the particle's position along the y axis and y_o is its initial y position. Then, since there is no parallel kinetic energy, the magnetic moment (first adiabatic invariant) can be written as:

$$\mu = \frac{\varepsilon_o + qE(y - y_o)}{B}, \quad (2.26)$$

which is a function only of the position and the initial conditions. As stated above, the trajectory of this particle's guiding center can be determined by simply following a locus of points that is everywhere perpendicular to the gradient in μ .

Figure 2.6 shows several trajectories computed in this manner. The particles were all initiated at a the position $(x,y)=(-20,-5)$, in units of Earth radii. At this location, the $\vec{E} \times \vec{B}$ velocity dominates. This drift is in the \hat{x} direction, which is to the right in figure 2.6. As the particles move Earthwards, the gradient in the magnetic field increases, and hence the relative importance of the ∇B drift. The ∇B drift is in opposite directions for electrons and protons. Hence, electrons and protons are swept towards the dawn and dusk sides of the magnetosphere, respectively. As the ∇B drift is larger for particles with larger kinetic energies, more energetic particles are swept further towards dawn or dusk than are less energetic ones. This is a real effect, readily observed in the magnetosphere. The net result is a distributed *space charge*, positive on the dusk side and negative on the dawn side. The building up of this space charge can be thought of as the dielectric response of the magnetosphere to the impressed electric field.

2.7 Example 2: Particle Heating and Faraday's Law

In figure 2.6, it can be seen that the guiding center velocities have, at times, components in the y direction. This means that the particles are crossing equipotentials of the electric field and are therefore gaining or losing energy. One way to understand

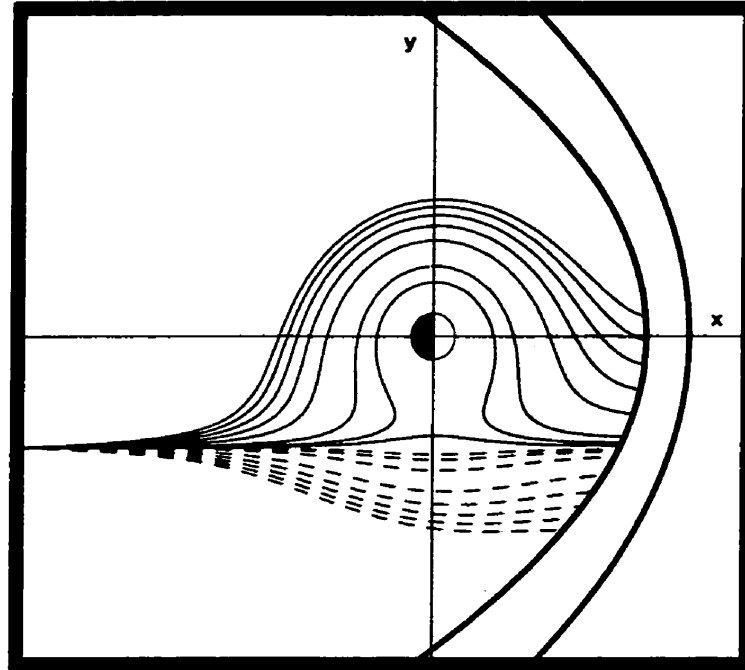


Figure 2.6: Particle trajectories in the equatorial plane. Solid lines are proton trajectories; dashed lines are electrons. The electric field is directed towards to the top of the figure and the magnetic field out of the page. The electric field used corresponds to an 80 kV potential drop across a distance of 40 Earth radii. This corresponds to an electric field strength of roughly 0.3 mV/m. The particle energies are 10 eV, 20 eV and then 50 eV to 550 eV in steps of 100 eV. All particle trajectories were initiated at the same point at the left side of the figure. The $\vec{E} \times \vec{B}$ velocity is towards the right hand side of the figure. Both protons and electrons move toward the right in response to the $\vec{E} \times \vec{B}$ drift. Any motion in the dawn-dusk direction is a consequence of the ∇B drift (see caption for previous figure). The direction of the ∇B drift is opposite for electrons and protons: protons are swept duskward (up) and electrons dawnward (down). The ∇B drift is larger for more energetic particles, which accounts for the spread in the trajectories.

this is by noting that the direction of the gradient in the magnetic field is roughly directed radially toward the Earth. Therefore, the direction of the ∇B drift as the particle moves along the x axis early in the trajectory is roughly in the $\pm\hat{y}$ direction. This motion causes the particle to cross equipotential lines and therefore change energy. In particular, as particles move in the sunward direction on the night side of the magnetosphere, they gain kinetic energy. As an aside, this means that plasma closer to the Earth on the night side tends to be “hotter” than more distant plasma. This heating is readily observed with the use of particle detectors on spacecraft [Lui, 1992].

One can understand this particle energization by considering how the gradient drift causes motion in the direction of the electric field. There is, however, another way that I can look at how these particles gain (or lose) energy. This involves transforming into a frame of reference moving at the local $\vec{E} \times \vec{B}$ drift velocity. In this frame, the electric field is not curl free. This is a concrete, easily visualized example of a physical situation where there is a time changing magnetic field (in the moving frame) and hence an electric field with a non-zero curl. Particles undergoing cyclic motion in this electric field gain (or lose) kinetic energy.

In order for the guiding center approach to be applicable, the magnetic field can vary only slightly over distances on the order of the local gyroradius. If this is true (it is in this case), and if only a few gyrations of the particle are considered, then I can express the magnetic field strength as a function that varies linearly in space. For simplicity, consider a location on the x-axis. On the x-axis, on the night-side of the magnetosphere, the gradient in the magnetic field strength is in the direction of \hat{x} (see figure 2.5). In this case, the electric and magnetic fields are

$$\begin{aligned}\vec{E} &= E\hat{y} \\ \vec{B} &= B_o(1 + \alpha x)\hat{z}.\end{aligned}\tag{2.27}$$

Here, the coordinate system has its origin located *at* the guiding center, but is not moving with the guiding center. B_o is the magnetic field strength *at* the guiding center. I will now transform into the frame that is moving at the $\vec{E} \times \vec{B}$ drift velocity consistent with the fields at the location of the guiding center. That is,

$$\vec{U} = \frac{\vec{E} \times \vec{B}_o}{B_o^2}.\tag{2.28}$$

As well, the origin of the moving frame is at the location of the guiding center. The electric field in the moving frame is

$$\begin{aligned}\vec{E}' &= \vec{E} + \frac{\vec{B} \times (\vec{B}_o \times \vec{E})}{B_o^2} \\ &= \vec{E} + \frac{1}{B_o^2} \{(\vec{E} \cdot \vec{B})\vec{B}_o - \vec{E}(\vec{B} \cdot \vec{B}_o)\} \\ &= \vec{E} \left\{1 - \frac{B}{B_o}\right\} \\ &= -E\alpha x\hat{y}.\end{aligned}\tag{2.29}$$

Note that the electric field in this frame is zero at the x-position of the guiding center. Taking the curl of this electric field, it is not curl free:

$$\vec{\nabla} \times \vec{E}' = -E\alpha\hat{z}.\tag{2.30}$$

That this must be the case is clear by considering Faraday's law:

$$\vec{\nabla} \times \vec{E}' = -\frac{\partial \vec{B}'}{\partial t}. \quad (2.31)$$

As the guiding center moves in the nonuniform magnetic field, the time derivative of the magnetic field strength in the moving frame is clearly not equal to zero. The curl of the electric field in this frame will not be zero, even though the magnetic field is static and the electric field is curl free in the lab frame. Figure 2.7 shows the vector electric field in the moving frame, in the vicinity of the guiding center.

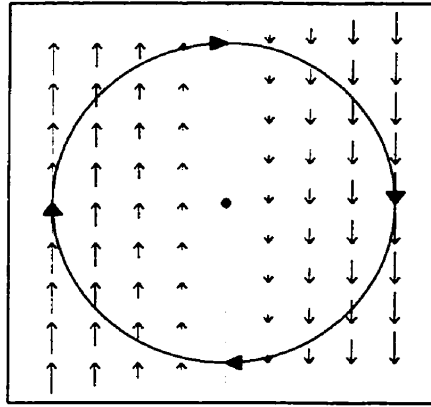


Figure 2.7: Electric field in the moving frame (see text). The magnetic field points out of the page. The trajectory shown is for a positively charged particle. As it follows the nearly circular path, it is accelerated due to work done by the electric field. It is clear that the electric field in the moving frame is not curl-free.

The electromotive force (EMF) around a closed contour is defined by the following path integral:

$$\text{EMF} = \oint_{\Gamma} \vec{E}' \cdot d\ell. \quad (2.32)$$

Using Stokes' theorem, I can express the EMF as a surface integral:

$$\text{EMF} = \int \int_s (\vec{\nabla} \times \vec{E}) \cdot d\vec{a}. \quad (2.33)$$

The integration contour in equation 2.33 is the (nearly) circular path followed by a proton during one gyration in the moving frame (this is shown in figure 2.7). I can then evaluate the double integral in equation 2.33 over the surface bounded by this circle. The EMF is then the area of this circle (πR_L^2 , where the radius of the circle is approximated by the Larmor radius R_L) multiplied by the magnitude of the curl of the electric field (αE). One must think a bit about the appropriate direction of $d\vec{a}$, which is the $-\hat{z}$ direction, in this case. The amount of kinetic energy the particle picks up during one gyration is $q\text{EMF}$. This is the work done on the particle by the electric field during one gyration:

$$\begin{aligned} \Delta W &= q\text{EMF} \\ &= qE\alpha\pi R_L^2 \\ &= E\alpha\pi m^2 V_\perp^2 / (qB_o^2) \\ &= 2E\alpha\pi m\varepsilon_\perp / (qB_o^2). \end{aligned} \quad (2.34)$$

Here, and throughout section 2.8, take ΔW to be a positive number, and q and E to be the magnitudes of the charge and electric fields, respectively. As well, I have used ε_\perp to represent that part of the kinetic energy that determines the local Larmor radius. In the next section, I will use this relation in an indirect derivation of the ∇B drift.

2.8 Example 3: An Alternative Derivation of the ∇B Drift

In the situation discussed in section 2.7, a charged particle moves in orthogonal electric and magnetic fields. The magnetic field strength increases linearly in the $\vec{E} \times \vec{B}$ direction. Charged particles moving in this field configuration gain kinetic energy. In the rest frame, this can be understood in terms of the ∇B drift carrying the particle across a potential difference (ie., in this situation, the ∇B drift is parallel to the electric field). In the moving frame, an EMF induced by a time changing magnetic field does the work. The gain in kinetic energy in both frames must be the same. This fact provides an easy way of deriving an expression for the ∇B drift [Cully and Donovan, 1999].

The time for one gyration is the gyroperiod:

$$T_G = \frac{2\pi m}{q B_0} \quad (2.35)$$

where I am again taking q to be the magnitude of the charge. In this time, the particle moves a distance in the direction of the electric field in the rest frame given by

$$\Delta y = V_{\nabla B} T_G \quad (2.36)$$

and gains an amount of energy given by

$$\Delta W = V_{\nabla B} T_G q E. \quad (2.37)$$

This is just the (positive) amount of work done by the electric field in the rest frame due to motion of the particle in the direction of that electric field. This is also the

amount of work done by the EMF in the moving frame (see equation 2.34). Equating the energy gained during one gyration in the moving and rest frames,

$$V_{\nabla B} T_G q E = 2 \frac{E \alpha \pi m \varepsilon_{\perp}}{q B^2}. \quad (2.38)$$

I have dropped the subscript on the magnetic field magnitude. The latter is justified in any situation where the ∇B drift is a reasonable approximation of the average motion due to the gradient in the magnetic field strength. Since α is the linear variation in the magnetic field,

$$\alpha = \frac{|\nabla B|}{B}. \quad (2.39)$$

Using the expressions for α and T_G in equation 2.38,

$$V_{\nabla B} \frac{2\pi m}{q B} q E = 2 \frac{E |\nabla B| \pi m \varepsilon_{\perp}}{q B^3} \quad (2.40)$$

which leads to the following expression for the magnitude of the ∇B drift velocity:

$$V_{\nabla B} = \frac{|\nabla B|}{q B^2} \varepsilon_{\perp}. \quad (2.41)$$

Consideration of how the Larmor radius varies due to the gradient in the strength of B shows that the direction of the drift is orthogonal to this gradient and is opposite for charges of opposite sign. This allows me to write down a vector expression for the ∇B drift:

$$\vec{V}_{\nabla B} = \frac{\varepsilon_{\perp}}{q B} \frac{\vec{B} \times \nabla B}{B^2}. \quad (2.42)$$

In this final equation, the symbol q includes the sign of the charge. This equation is identical to equation 2.16.

2.9 The Guiding Centre Equations of Motion

In addition to the $\vec{\mathbf{E}} \times \vec{\mathbf{B}}$ and ∇B drifts, there are a host of other drifts that arise in various electric and magnetic field topologies. Some of these other drifts include the curvature drift, the generalized polarization drift, the convective curvature drift and the “g cross B” drift which arises in the presence of a gravitational field. There are methods for deriving each of these drifts separately. However, it is also possible to expand the motion in Taylor series and derive the guiding centre equations of motion in a general way [Northrop, 1963]. The expansion is done with a “smallness parameter” m/q . All of the drifts mentioned above are first order drifts, with the exception of the $\vec{\mathbf{E}} \times \vec{\mathbf{B}}$ drift, which is of order zero (and hence, in many cases, the only drift that needs to be considered). In the general case, there are two equations, one for motion parallel to the field line and one perpendicular to the field line. To first order, these equations are [Northrop, 1963]:

$$\begin{aligned}
 m \frac{dV_{\parallel}}{dt} &= mg_{\parallel} + qE_{\parallel} - \mu \frac{\partial B}{\partial s} + m \vec{V}_{\vec{\mathbf{E}} \times \vec{\mathbf{B}}} \cdot \frac{d\hat{\mathbf{B}}}{dt} + O(\varepsilon^2) \\
 \vec{V}_{\perp} &= \frac{\vec{\mathbf{E}} \times \vec{\mathbf{B}}}{B^2} + \frac{\mu}{q} \frac{\vec{\mathbf{B}} \times \nabla B}{B^2} + \frac{m}{q} \frac{\vec{\mathbf{g}} \times \vec{\mathbf{B}}}{B^2} \\
 &\quad - \frac{m}{qB^2} \left[V_{\parallel} \frac{d\hat{\mathbf{B}}}{dt} + \frac{d\vec{V}_{\vec{\mathbf{E}} \times \vec{\mathbf{B}}}}{dt} \right] \times \vec{\mathbf{B}} + O(\varepsilon^2).
 \end{aligned} \tag{2.43}$$

In the above equations, ε is the expansion parameter m/q , and total time derivatives are *convective derivatives*:

$$\frac{d}{dt}X = \left[\frac{\partial}{\partial t} + V_{\parallel} \frac{\partial}{\partial s} + (\vec{V}_{\vec{E} \times \vec{B}} \cdot \nabla) \right] X \quad (2.44)$$

While the derivation of these equations is both tedious and, quite frankly, not overly enlightening, it is instructive to consider how particular terms arise. For example, the third term in the parallel equation is the consequence of the *centrifugal* force acting in the non-inertial reference frame of the guiding center. This allows, for example, the diversion of perpendicular energy into energy along the magnetic field, a process through which outflowing ionospheric ions pick up energy. Similarly, the fifth term in the perpendicular equation represents drifts that arise when the particles are carried (by a combination of convection via the $\vec{E} \times \vec{B}$ drift and motion along the field line) across a gradient in the $\vec{E} \times \vec{B}$ drift. This, in turn, creates a secondary drift (the generalized polarization drift) that occurs when the electric field seen by the gyrating particle (i.e., in the guiding center frame of reference) changes in time. A simplified version of this drift is derived by Nicholson [1983].

In most introductory space physics texts, treatments of adiabatic motions are restricted to the derivation of the $\vec{E} \times \vec{B}$, grad-B, and curvature drifts, and the mirror force (via conservation of the first adiabatic invariant). Although this is sufficient for many space physics applications, ion outflow applications such as those I present in chapter 6 require all terms shown in equation 2.43³. Neglecting terms would leave out much of the essential physics, particularly the resulting particle energization.

³Note that the time-stationary fields used in the tracing in chapter 6 imply that *partial* derivatives of field quantities with respect to t are zero, although total derivatives are generally not.

Chapter 3

The Suprathermal Mass Spectrometer (SMS) and Initial Data Reduction

3.1 The Akebono (EXOS-D) Satellite



Figure 3.1: The Akebono satellite, with antennae and booms retracted¹.

In February, 1989, the Japanese Institute of Space and Astronautical Science (ISAS) launched the fourth in their “EXOS” series of satellites from the Kagoshima Space Center in southern Japan. After successful orbital insertion, the satellite was given the Japanese name Akebono (“Dawn”). Although originally designed for a lifetime of 2 years, the satellite is still in operation.

¹This figure appeared on the cover of *Geophysical Research Letters*, February, 1991, and is used with permission.

The primary objectives of the Akebono mission were to study auroral electron acceleration processes and global ionospheric plasma dynamics [Tsuruda and Oya, 1993]. To meet these objectives, the orbit of the satellite had to be designed to fulfill three criteria. Those criteria are that the satellite should visit:

1. all magnetic latitudes above 60 degrees invariant,
2. all magnetic local times, and
3. all altitudes between roughly 500 and 10000 km.

To fulfill the first criterion, Akebono was launched into an orbit with an inclination angle of 75° (the inclination angle is the angle between the orbital plane and the Earth's equatorial plane; a polar orbit has an inclination of 90°). This inclination has allowed it to sample the polar cap at magnetic latitudes up to 90° , with particular emphasis on the auroral latitudes. To meet the second criterion, the orbital plane of the satellite drifts so that all magnetic local times are covered in roughly an 8-month period. For the third criterion, the initial apogee altitude (highest altitude in the elliptical orbit) was 10 500 km, with perigee (lowest altitude) at 275 km, allowing extensive sampling both below and within the auroral acceleration region. The apogee altitude has been declining at a rate of roughly 200 km per year. In order that criterion 3 was met separately for differing latitudes (that is, so that the apogee is not always at the same latitude), the line of apsides (the line between apogee and perigee) drifts such that the apogee drifts from the northern hemisphere to the southern hemisphere and back again every 1.6 years. The orbital period is 3.5 hours, and the spacecraft is spin-stabilized, with a spin period of 8 seconds. The spin axis points in the sunward direction.

The scientific payload consisted of eight instruments, including electric and magnetic field detectors, two wave experiments, a low energy particle detector, an ion mass spectrometer, a thermal-energy electron detector and an imager. Seven of the instruments were developed and built by researchers at Japanese laboratories. The ion mass spectrometer (called the Suprathermal Mass Spectrometer, or “SMS”) was designed and built in Canada.

3.2 SMS Design and Thermal/Suprathermal Mode Operation

The scientific objective of the SMS program was to study the composition of the bulk plasma parameters (density, temperature, and velocity) of thermal and energetic ions. The instrument is a folded Bennett-type ion mass spectrometer that works in the 1-70 amu/ e and 0.1-4000 eV range, and is mounted on the side of the satellite (see figure 3.1). As the satellite spins, SMS can examine the incident ion population moving in various directions in the spin plane. In its thermal “fast-scan” mode the instrument measures the flux of H^+ , He^+ and O^+ at 8 energy steps between 0 and 32 eV and 32 angular steps in the spin plane of the satellite. There are several other modes which I will not describe here, but are described in detail by Whalen et al. [1990] and Yau et al. [1998]. SMS was designed and built at the National Research Council (Ottawa), SED systems (Saskatoon), and the Communications Research Laboratory (Japan), under the overall leadership of Dr. B. Whalen. The current principal investigator is Dr. A. Yau. Figure 3.2 is a schematic view of the instrument.

For each angular step, the instrument must be able to discriminate between

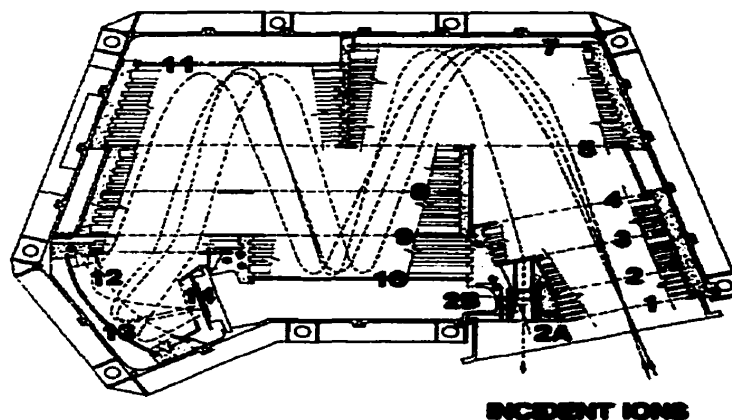


Figure 3.2: Schematic view of SMS [Yau et al., 1998, used with permission.]. Primary electrodes are numbered, and guard rings are shown in cutaway. Four possible ion trajectories are shown. Other dashed lines are gridded electrodes.

particles of different energy and species. This is accomplished in three stages. The first stage, consisting of electrodes 1 through 7, is the entrance aperture and retarding potential analyser. In the thermal mode, this section performs the energy selection, allowing through only ions with an energy greater than the retarding potential times the charge (qV_{RPA}) and less than 72 eV (RPA is an acronym for “Retarding Potential Analyser”, which is the type of energy analysis scheme used). The ions are then accelerated to roughly 1 keV, and sent to the second stage. The second stage, electrodes 5 and 8 to 11, can be tuned to accelerate only those ions that have a given velocity. Since the energy is known (1 keV), selecting a velocity is equivalent to selecting a mass. The ions are then sent to the third stage, which is the detection stage. In this stage, the ions are again sorted by energy, and only those ions that were accelerated in stage 2 are counted. So, for an ion to be detected, it must have an energy between qV_{RPA} and 72 eV, and a mass such that it is accelerated by the

second stage.

In the thermal fast scan mode, the second stage tuning is set to accelerate H^+ , and then V_{RPA} is quickly scanned through 8 steps in the 0 to 20 V range. The second stage is then tuned for He^+ and the V_{RPA} scanning is repeated. O^+ and either O^{++} or He^{++} are also scanned in the same manner. This entire process repeats 32 times in an 8-second spin. In the operation mode used in this study (mode 2A), such a thermal fast scan is performed every second spin. Alternate spins are used for the study of higher-energy ions.

3.2.1 Aperture and Energy Selector

As mentioned above, electrodes 1 through 7 perform the energy selection. Electrode 1 is the large-aperture entrance through which the ions enter the instrument. In mode 2A, it is biased at -3.3 V with respect to the spacecraft. This is done to offset the fact that low-energy ions could be reflected by a positive spacecraft potential, and therefore not seen by the instrument. The negative biasing is only partly effective, due to the large Debye length in the plasma (see, e.g., Drakou et al. [1997]). Measurements taken when the spacecraft potential was high are therefore excluded from the current study.

Electrode 2 is the retarding potential analyser. It is set at a voltage V_{RPA} with respect to electrode 1. Any ions which have an energy less than qV_{RPA} at electrode 1 are reflected back. This is the main energy selection method for the thermal modes.

Grids 2A and 2B form the small and medium apertures. These are used under high density conditions when the use of the large aperture (grids 1 and 2) would saturate the detector. All data collected for this study used large aperture mode,

where grids 2A and 2B were held at a high potential, to prevent entry of ions through the small and medium apertures.

Between grids 3 and 4, there is a 1 kV acceleration potential. Grids 5 and 7 reflect the ions into the second section. Any ion with more than 1072 eV energy (i.e. any ion that had more than 72 eV energy at electrode 1) will strike electrode 7 and be absorbed. Therefore, ions that curve around to the next section must have entered at electrode 1 with an energy between qV_{RPA} and 72 eV.

3.2.2 Bennet-type Velocity Selector

The second stage consists of electrodes 5 and 8 through 11, and is a 3-stage “folded” Bennett-type mass spectrometer [Bennet, 1950]. Electrodes 5,8 and 9 are biased to the same potential, while numbers 10 and 11 are positively biased to reflect the particles.

To select for a given velocity, a radio-frequency AC accelerating potential of 200 V peak-to-peak is applied at electrode 8. An ion travelling at the “resonant” velocity, and entering the system with the correct phase, will cross electrode 8 at the same time as the AC potential crosses through zero, and will gain energy on both sides of the electrode [Bennet, 1950; Whalen et al., 1990]. Such an ion will be accelerated by 435 eV before leaving the velocity selector at electrode 12. An ion not at the resonant velocity, or entering the system with an incorrect phase, will not be significantly energized, and may even lose energy.

Since the ions all enter the spectrometer with an energy of 1 keV, the accelerating potential can be tuned so that the resonant velocity corresponds to any mass in the range 1 to 70 amu/ e . This means that only ions of the selected species, and with

the correct entry phase, will be accelerated.

One complication arises in that the ions gain energy at each crossing of electrode 8, so the AC frequency at which electrode 8 is driven should therefore ideally increase for each crossing. This would be difficult in practice, however, because of considerations related to matching the phase of the AC signal. Fortunately, the mass resolution of the instrument was found to be adequate without introducing this complication.

3.2.3 Energy Analyser and Detector

Ions entering this last section are in one of two populations. Either they are ions that are of the selected species, which arrived at electrode 1 with an energy in the range qV_{RPA} to 72 eV, and which entered the velocity selector with the correct phase, or they are not. Those in the first category (call this population 1) arrive at electrode 12 with an energy of approximately 1435 eV, while those in the second category (population 2) are less energetic, typically around 1000 eV. The task of the final energy analyser is to discriminate those two populations.

Electrode 12 consists of three pieces. The first is a planar electrode opposite electrode 9. The second is a cylindrical electrode opposite electrode 13, and the third is a planar electrode opposite electrode 14. Ions enter from electrode 9, cross the field-free region inside electrode 12 and are focussed and energy dispersed in the cylindrical field between grids 12 and 13. This separates out the two populations; while both populations are focussed to a plane just behind electrode 14, those with a higher incident energy (i.e. population 1) are focussed to a lower location in figure 3.2 than those with a lower incident energy (i.e. population 2).

Ions leaving electrode 12 are accelerated another 1220 volts by electrode 14 before striking the detector, located immediately behind electrode 14, at the focal plane of electrode 13. The detector is a Micro-Channel Plate (MCP). The electron cascade produced by an ion strike on the SMS MCP produces roughly 10^6 electrons at the back of the MCP [Whalen et al., 1990]. The MCP efficiency² has, however, degraded over time (see figure 3.3). The MCP is divided into 16 pixels: 4 rows of 4 columns each. Ions from population 1 strike two specific columns on the MCP. Which of the four columns this is depends on the exact biasing voltages applied at grids 12 and 13. Early in the mission, columns 1 and 2 were used. However, repeated impacts of energetic particles eventually degraded the MCP in those columns, so the biasing was changed in March, 1993 so that columns 3 and 4 were used.

3.3 Construction of Velocity Distribution Functions

The most general method with which to characterize the particles at a given location is to specify the velocity distribution function. This is a function of 3 variables V_x , V_y and V_z , and specifies the number of particles at that location moving with a velocity between (V_x, V_y, V_z) and $(V_x + \delta V_x, V_y + \delta V_y, V_z + \delta V_z)$. In space plasmas, the assumption is usually made that the distribution function is symmetric with respect to rotations about the magnetic field direction. Such a distribution is said to be “gyrotropic”. For a gyrotropic plasma, the velocity distribution function (VDF) is a figure of revolution about the magnetic field direction once the guiding centre motion is subtracted (see chapter 2). The VDF can then be expressed as a function of only

²The MCP efficiency gives the number of electronic “counts” per incident particle.

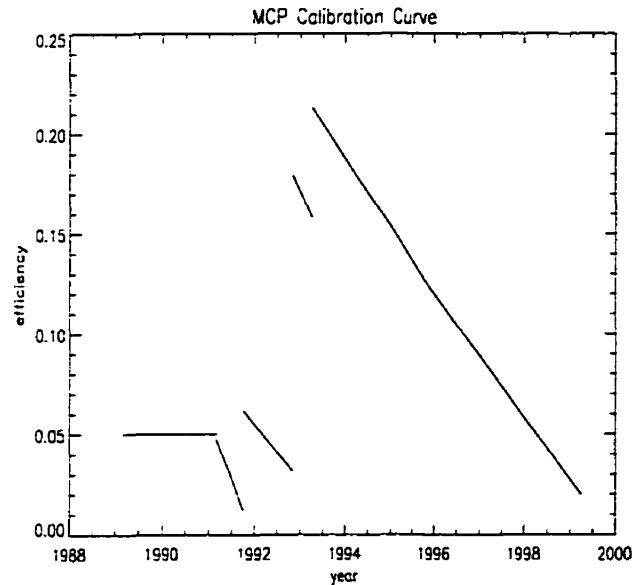


Figure 3.3: The efficiency of the microchannel plate detector as a function of time. Degradation can be seen throughout the lifetime of the instrument, as particles hit the MCP and physically damage it. Discontinuities in the curve arise when the biasing of the electrodes changes after a command issued from the ground. During the period from launch to February 1991, the MCP efficiency was held constant by changing the bias voltages.

2 variables: the velocity parallel to \vec{B} , denoted V_{\parallel} , and the velocity perpendicular to \vec{B} , denoted V_{\perp} .

In mode 2A, for every second satellite spin, the number of counts seen by the MCP at 32 angular positions and 8 energy steps is relayed to the ground stations for each of the four species. This section deals with how to get from this information to an approximate VDF for the plasma outside the instrument during that spin. Figure 3.4 is a flow chart summary of the data analysis that I have carried out. The overall idea of the analysis is to first find the distribution function in the spin plane of the

satellite. Then, providing the angle between $\vec{\mathbf{B}}$ and the satellite spin plane is small, the VDF is approximately given by the revolution of this function about $\vec{\mathbf{B}}$ after subtracting the projection of $\vec{\mathbf{E}} \times \vec{\mathbf{B}}$.

3.3.1 Spin Plane Count Distribution Functions

The first step to determining the VDF for a particular satellite spin was to determine the count distribution function in the spin plane of the satellite. Such a distribution gives the number of counts detected by the MCP as a function of velocity parallel and perpendicular to the projection of the magnetic field onto the spin plane.

Data directly from the satellite was first binned into an energy/spin angle count distribution function by determining the satellite orientation for each measurement in the spin. This function gives the number of counts recorded by the MCP as a function of the satellite spin angle and the particle energy at the entrance. The energy was then corrected for the effects of spacecraft (ram) velocity, spacecraft charging, and entrance aperture voltage biasing.

For the estimation of the spacecraft charging, we used the non-linear data fitting method of Drakou et al. [1997]. This method involves the assumptions that the plasma VDF assumes the form of a drifting Maxwellian, and that the spacecraft charging varies slowly over time (i.e. on a time scale of minutes). It must be pointed out that both of these assumptions are sometimes invalid. However, comparisons between the resulting estimate for the spacecraft potential and the potential measured by the electric field instrument (measurements which are not always available) have confirmed that the procedure is usually reasonable [A. W. Yau, private communication]. The effect of spacecraft charging was removed under the “thin sheath”

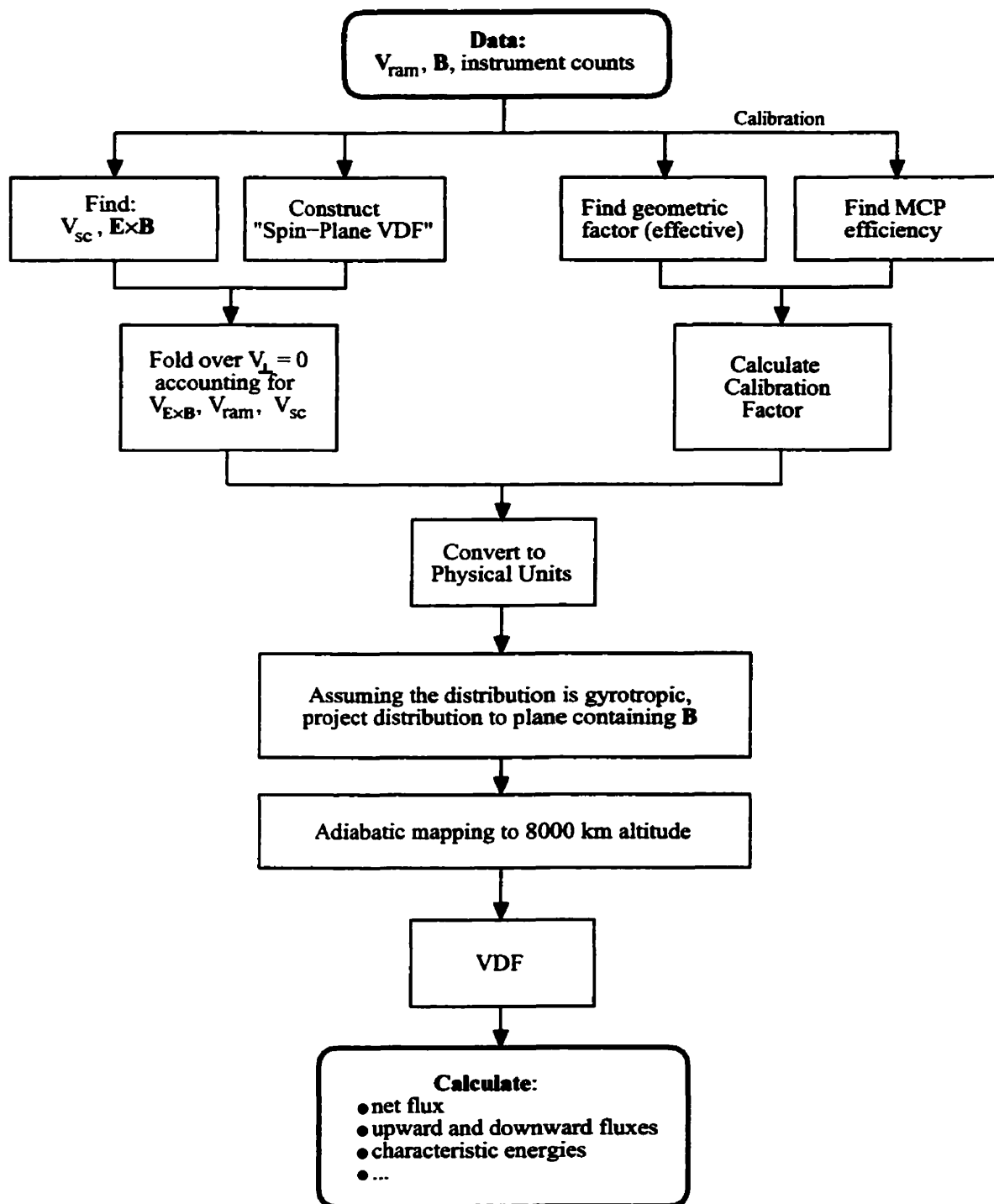


Figure 3.4: Flowchart for constructing velocity distribution functions from the SMS data.

approximation $KE_{\perp} = KE'_{\perp} - qV_{s/c}$ where KE_{\perp} and KE'_{\perp} are respectively the kinetic energies of the particle at the entrance aperture and outside the spacecraft sheath, and $V_{s/c}$ is the spacecraft potential.

As mentioned in section 3.3, the perpendicular drift velocity (at this altitude the $\vec{E} \times \vec{B}$ velocity completely dominates the gyroaveraged motion of the ions orthogonal to the magnetic field) must be removed to generate distribution functions in the guiding centre (GCS) frame of reference. The count distribution function was therefore first transformed from energy/pitch angle space to parallel/perpendicular velocity space. Although the sign for the perpendicular velocity is ambiguous, it will be seen below that this is not a problem. In the velocity space, the guiding centre drift velocity was next found by examining the counts in the perpendicular direction. Profiles of constant parallel velocity were combined and the peak of the resulting net profile, which is a function of the perpendicular velocity, was assumed to correspond to the spin plane projection of the guiding centre drift velocity. The peak of the distribution was determined by fitting a Gaussian distribution to the profile. If the distribution was not well approximated by a Gaussian, the drift velocity was determined from $\bar{v}_{\perp} = \sum_i v_{\perp}^i c_i / \sum_i c_i$, where v_{\perp}^i are the velocities of the perpendicular velocity bin centers and c_i are the counts associated with those bins. The estimate for \bar{v}_{\perp} was heavily affected by “holes” in the profile (e.g. missing data) but much less affected by heavy scatter, and as such constitutes a good complement to the Gaussian fitting procedure.

Once the drift velocity for the spin was identified, it was adjusted to fall on the nearest velocity bin boundary, and the spin plane count distribution was “folded” about the perpendicular drift velocity to increase the signal-to-noise ratio and yield

improved count statistics. This is why the ambiguity with regards to the perpendicular direction was irrelevant. The final spin plane count distribution function is a function of the parallel velocity and the perpendicular speed in the plasma frame of reference.

3.3.2 Differential Flux

The counts seen by the instrument are proportional to the differential flux arriving at the entrance aperture³. The conversion between the counts seen by an instrument and the differential flux may be as simple as multiplying by a constant referred to as the *geometric factor*, which gives the effective size of the detector. In this case, however, the conversion is somewhat more complicated, as the geometric factor is energy dependent. The conversion formula from counts to differential flux for the SMS instrument is

$$j(m, E, \alpha, \phi) d\Omega dE = \frac{\text{counts}}{\epsilon_{grid}\epsilon_{MCP}\epsilon_{phase}\tau A_x A_y \pi \sin^2 \left[\frac{c_1}{E^2 + c_2} + c_3 \right]} \quad (3.1)$$

where α is the pitch angle and ϕ is the particle gyrophase. The various empirical factors are given in table 3.1.

For subsequent integrations, the differential flux was assumed to fill the entire bin in which the measurement was taken, and was projected into the plane containing \vec{B} . Adjustments for the assumed loss cone size were found to make little difference in the calculated flux. Given that the selection criteria assured that \vec{B} was always contained within the field of view of the instrument, this adjustment was not made.

³Differential flux is the number of ions crossing a unit surface per unit time in a unit energy range, and spanning a unit solid angle.

Symbol	Quantity	Value
ϵ_{grid}	Total electrode grid transmission efficiency	0.314
ϵ_{MCP}	MCP efficiency	See figure 3.3
ϵ_{phase}	Phase acceptance efficiency	0.2
τ	Accumulation time	3.8 ms
A_x	Aperture opening (x)	5.5 cm
A_y	Aperture opening (y)	8.0 cm
c_1	Empirical fit coefficient	550 eV ² -degree
c_2	Empirical fit coefficient	70 eV ²
c_3	Empirical fit coefficient	1.0 degree
$d\Omega$	Instrument field of view	0.74 sr

Table 3.1: Physical SMS parameters needed for differential flux calculation.

3.3.3 Adiabatic Correction

As I pointed out in the introduction, my overall goal in working with the SMS data set was to obtain input for a study of the significance of the importance of the contribution of thermal and suprathermal ionospheric plasma to the magnetosphere. With that in mind, it was clear that I had to find a way that VDFs measured at different altitudes could be meaningfully compared. The energy and pitch angles of the ions evolve as they move up the magnetic field lines, according to equation 2.43. As such, the same plasma population will have a different VDF at a different altitude. In order to facilitate the intercomparison of VDFs from a range of altitudes, I “projected” each VDF to a common altitude of 8000 km. In order to do so, I invoked conservation of the first adiabatic invariant, and conservation of kinetic energy. I neglected the effects of any parallel electric fields, and presumed that the $\vec{E} \times \vec{B}$ drift dominated the guiding center motion orthogonal to the field line.

Applying conservation of the first adiabatic invariant (see section 2.5), $\mu = E_{\perp}^*/B$,

and conservation of energy between the observation and reference altitudes, it can be shown that the parallel energy at the reference altitude is given in terms of the parallel and perpendicular energies at the observation altitude by

$$KE'_{\parallel} = KE_{\perp}^* + KE_{\parallel} - KE_{\perp}^* \frac{B'}{B} + (KE_d - KE'_d) \quad (3.2)$$

$$KE'_{\perp}{}^* = KE_{\perp}^* + KE_{\parallel} - KE'_{\parallel} + (KE_d - KE'_d) \quad (3.3)$$

where KE_d denotes the $\vec{E} \times \vec{B}$ drift energy, a * indicates values in the guiding centre frame of reference (GCS) and primed quantities are quantities at the reference altitude. These equations allow the mapping of the energies from one altitude to another, providing B' and KE'_d are known. B' is given by the field models, while KE'_d also requires the electric field. Conservation of magnetic flux, combined with the fact that magnetic field lines are equipotentials, gives

$$E' = E \sqrt{B'/B}, \quad (3.4)$$

from which the drift velocity (and, hence, energy) at the reference altitude follows.

In mapping the VDF to a different altitude, I have assumed that the $\vec{E} \times \vec{B}$ drift dominates the guiding center motion orthogonal to the magnetic field and that there is no parallel electric field. While the former assumption is perfectly reasonable, the latter is often questionable. Short of modelling this process self-consistently, however, there is no way of dealing with the effects of the parallel electric field. Furthermore, there is no practical way of modelling these processes that would add anything substantive to the statistical study at hand.

3.4 Definition of Flux, Unidirectional Flux, Net Fluence and Unidirectional Fluence

To characterize the amount of plasma leaving the ionosphere, three quantities are calculated for each species for each observation: the *net flux* and the *upward and downward unidirectional fluxes*. The *upward unidirectional flux* (or simply *upward flux*) is the total number of ions that cross a unit area in a unit time, moving in the upward direction:

$$J_u(m) = -2\pi \iint_{\pi/2}^{\pi} j(m, E, \beta) \cos(\pi - \beta) \sin(\beta) d\beta dE \quad (3.5)$$

where $j(m, E, \beta)$ is the observed differential flux, β is the pitch angle and E is the energy. This is valid in the northern hemisphere, where the upward direction is $\beta = \pi$ (since field lines come down into the north pole). Note that J_u is always positive. Although this sign convention is opposite to some definitions (for example, [Yau et al., 1985]), I feel it is the more intuitive convention in the current context, where no data from the southern hemisphere have been used. The *downward unidirectional flux* is similarly defined, but involves only ions moving downward:

$$J_d(m) = -2\pi \iint_0^{\pi/2} j(m, E, \beta) \cos(\pi - \beta) \sin(\beta) d\beta dE. \quad (3.6)$$

J_d is always negative. The *net flux* is the total of J_u and J_d (i.e. the total number of ions going up minus the total number going down):

$$\Phi(m) = -2\pi \iint_0^{\pi} j(m, E, \beta) \cos(\pi - \beta) \sin(\beta) d\beta dE \quad (3.7)$$

$$\begin{aligned}
 &= J_u(m) + J_d(m) \\
 &= |J_u(m)| - |J_d(m)|.
 \end{aligned}$$

In most familiar situations, it is the net flux that is of interest. For example, if one is interested in the flow of air within a ventilation shaft, the net flux of air molecules times the area of the shaft gives the total flow of air through the shaft. The unidirectional fluxes, in contrast, incorporate the thermal motion of the molecules as well as the overall flow. Due to the high thermal speed, the unidirectional flux would be much larger than the net flux unless the air was moving supersonically through the duct. Since the air molecules move only a short distance before colliding with another air molecule and changing direction, the unidirectional fluxes are of limited interest.

In the current problem, however, the ions are unlikely to collide with anything before making it back to the equatorial plane. If the question pertains to the number of ions leaving the ionosphere, it is therefore the upward unidirectional flux that is of interest. This is what will be used for the tracing performed in chapter 6. However, if the question is how many ions leave the ionosphere compared with how many return, the net flux is of concern. This is primarily of interest for questions of the global mass budget.

Of course, for both of these questions, the flux must be integrated over some area of interest. The *(net) fluence* or *net outflow rate* is the net flux integrated over the area of interest. It is in units of ions per second, and defines the net number of ions flowing up from that region. The *upward unidirectional fluence* (or simply, *upward fluence*) is the upward flux integrated over the area of interest. It is also in units of

ions per second, and defines the number of ions in the region of interest that escape up past the measurement altitude per second.

3.5 Data Selection Criteria and Coverage

Low-energy ion outflow is an inherently difficult quantity to measure. There are a variety of issues that must be assessed before a record can be used. The data selection used in this study requires that each record was recorded:

1. in the altitude range from 6000 to 10000 km.
2. in the northern hemisphere.
3. at an invariant latitude above 60° .
4. in mode 2a, using the large aperture setting.
5. under spacecraft charging conditions such that the entrance grid was biased at least 1 volt negative with respect to the ambient plasma.
6. on a day when the MCP calibration was not changing.
7. with no detectable telemetry errors.
8. in a spin plane no more than 20° from the magnetic field direction.
9. under conditions such that the nonlinear fitting algorithm of Drakou et al. [1997] converged to an estimate of the spacecraft charging either for the record itself or for the records surrounding it.

1 317 916 mode 2a (large aperture) data points were available between October, 1989 and September, 1998. The required instrument calibration after 1998 was not known at the time of writing. Of these records, only 504 480 fulfilled the first three positional criteria. The remaining data filtering criteria reduced this number to 265 990, or 20% of the original data.

There are a few systematic bias and selection issues that arise from the above criteria. First of all, the requirement that the satellite be at apogee in the northern hemisphere means that data is taken in alternating 9-month periods (as the line of apsides drifts at a rate of 1 revolution every 18 months). This, combined with the low rate of precession of the orbital plane (8 months) makes the determination of seasonal trends subject to serious biasing problems (see section 5.4).

Secondly, the requirement that the spacecraft charging be low introduces a systematic bias toward higher-density plasma. The spacecraft charging is a monotonically decreasing function of density. Condition 5 in the above list therefore preferentially selects high-density conditions. Fortunately, the number of records rejected for this reason was small ($< 1\%$).

The requirement that the angle between the spin plane and the magnetic field direction be less than a certain threshold tends to reject records in the auroral zone either between roughly 9 and 15 local time or between roughly 21 and 3 local time. This is a consequence of the sun alignment of the spin vector. This also introduces a slight selection bias in favour of observations taken during lower magnetic disturbance levels in these regions. The data is binned by position and usually by magnetic disturbance level in the analysis, so this is not thought to be a significant issue. There is also a seasonal bias introduced by this requirement.

Finally, the last condition in the above list introduces a slight bias toward higher-density conditions, as the fitting algorithm requires a certain minimum number of counts to converge. Given that the number of excluded records is again low, the overall systematic bias is certainly less than the overall absolute instrument uncertainty, which has been estimated at roughly 30% [Yau et al., 1998].

Chapter 4

Observations of Ion Outflow from SMS: Statistical Theory and Model Formulation

4.1 Characterization of ion outflow

In practical terms, my overall objective is to use an appropriately reduced version of the SMS mode 2a¹ data set as input to a test-particle simulation of thermal and suprathermal ion outflow. The scientific objective that I am trying to meet by doing so is to determine the importance of the contribution of that ionospheric ion population and its role (if any) in magnetospheric dynamics. Ideally, the information required as input for this simulation is the distribution of upward moving ions, at some reference altitude, as a function of magnetic local time, magnetic latitude, particle energy, and pitch angle. One can think of this as a *global distribution function*. My task is a daunting one: the distribution function can assume a myriad of shapes, and differential flux values can vary over 4 orders of magnitude. The global distribution function will depend on the complicated set of ionospheric, exospheric, solar wind, seasonal, and diurnal conditions. Furthermore, Akebono observations are obtained only along satellite tracks across the polar and auroral regions at greater than three hour intervals, and in a restricted altitude and local time that evolves slowly, over the course of a given year.

The work that I present in this chapter is my very exploratory attempt to develop

¹See chapter 3

an empirical model of the ionospheric outflow, as a function of the state of the magnetosphere/ionosphere system, on the basis of the SMS mode 2a data set. Ideally, this model would account for the behaviour of the velocity distribution functions (VDFs); however, any model able to reproduce the above mentioned variability would require an extremely large number of degrees of freedom. This leads to what is known in statistics as the *curse of dimensionality*. The problem is that as the number of degrees of freedom increases, the amount of data required to fully characterize it increases dramatically.

From a practical standpoint, it is clear that any useful empirical model requires a low enough number of degrees of freedom that it can be meaningfully fit using the SMS data set, but have enough degrees of freedom so that it is useful for my purposes. In reality, trying to satisfy the above two conditions might not be possible. For example, it might be that I need to restrict the model such that the VDFs are assumed to be flowing Maxwellians (Gaussian distributions in velocity space with the mean displaced in the V_{\parallel} direction) that can be characterized by three parameters (density, temperature, and flow velocity). With only these three parameters, it would perhaps be possible to determine the statistical nature of each parameter, and also the interrelations between the parameters (e.g., “is the temperature sometimes correlated with the density?”). However, while the distribution functions sometimes resemble Maxwellians, it is more often that they do not. If I was to use this three parameter model of the VDFs, then, it would be important to determine whether the variability in the VDF shape was a significant consideration in the implementation of the test particle simulation.

It is extremely fortunate, then, that the fine details of the VDFs are actually

rather unimportant. It will be shown in section 6.3 that even dramatic changes in the shape of the distribution function create very small shifts in the supply of particles to the magnetotail. The important factor is the normalization of the distribution function. Specifically, the upward fluence of the source region is of primary importance. The remainder of this chapter will be devoted primarily to this issue, and the related issue of the characterization of the net flux. That is, *how much plasma is flowing out of the high-latitude ionosphere and what are the factors that affect this rate?*

4.2 Probability distribution of unidirectional flux

Since the fluence is an area integral of the flux, it is important to have a sense of the probability distribution of the latter in order to meaningfully discuss the former. Figure 4.1 is a histogram of measured O^+ net flux values. Figure 4.1a uses a linear x-axis, while 4.1b uses a logarithmic x-axis.

Although it would appear from figure 4.1a that the variance of the data is small, this is entirely misleading, since 20% of the data is not contained in the range of the x-axis. In fact, in order to draw a 95% confidence interval on figure 4.1a, the graph would need to be roughly 1.5 metres wide. To draw a 99% confidence interval, it would need to be about 6 metres wide.

Figure 4.1b is perhaps more useful for visualizing the distribution. The x-axis is logarithmic. Since the net flux can be negative or positive, this necessitates two graphs. Additionally, there are 15 360 measurements of zero flux, which cannot be plotted on either graph. Note that the bin centres are equally spaced on the

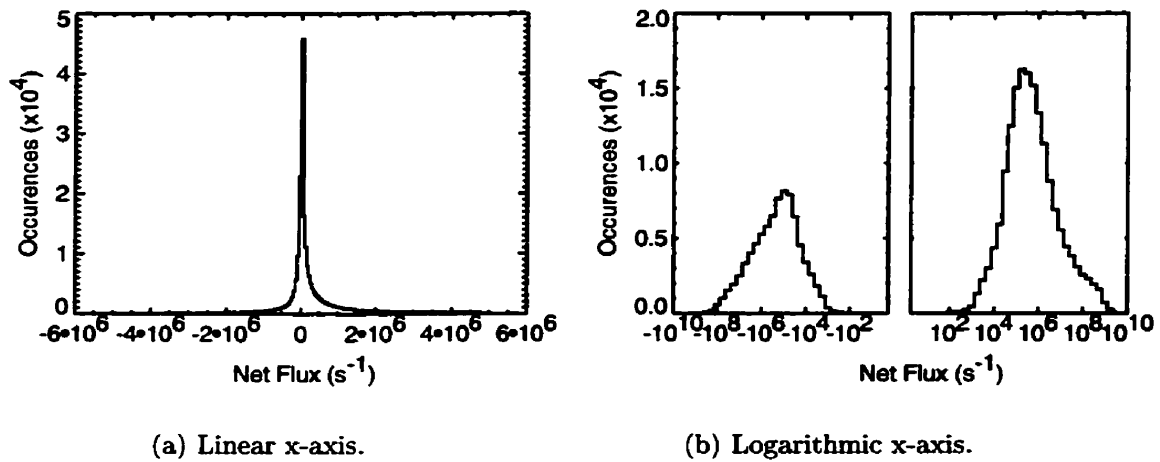


Figure 4.1: Histograms of measured O⁺ net flux values. Panel (a) uses a linear x-axis, while panel (b) uses a logarithmic x-axis. Since the data can be negative, this necessitates two graphs for panel b.

logarithmic scale, and the bin widths are therefore not constant². This is why the distribution looks bi-modal (as seen in figure 4.1a, it is not).

This distribution is heavy-tailed, in that the width of the distribution at the 95% confidence interval is much larger than its half-width would suggest. I tried fitting the distribution with many of the well-known distribution functions. Although the log-normal and inverse Gaussian distributions provided the best matches, none of the distributions was deemed adequate based on either graphical methods or χ^2 fitting. Table 4.1 lists some characteristics of the distribution.

The data is difficult to work with for three reasons. First, the distribution is heavy-tailed. Second, I could not fit a known distribution to the data. Third, as will be seen later (section 4.4.3), the data is not independently sampled. All of these factors increase the amount of data required to adequately determine such

²This histogram should not, therefore, be viewed as the probability distribution function.

Mean	$1.35 \times 10^7 \text{cm}^{-2}\text{s}^{-1}$
Standard Deviation	$9.95 \times 10^7 \text{cm}^{-2}\text{s}^{-1}$
2.5 th percentile	$-5.7 \times 10^7 \text{cm}^{-2}\text{s}^{-1}$
25 th percentile	$-0.016 \times 10^7 \text{cm}^{-2}\text{s}^{-1}$
Median	$0.037 \times 10^7 \text{cm}^{-2}\text{s}^{-1}$
75 th percentile	$0.43 \times 10^7 \text{cm}^{-2}\text{s}^{-1}$
97.5 th percentile	$80.8 \times 10^7 \text{cm}^{-2}\text{s}^{-1}$

Table 4.1: Characteristics of the net O^+ flux distribution.

parameters as the mean. The heavy demands placed on the data means that 265 990 available data points actually is not that much data.

4.3 Calculation of Mean Globally-Integrated Fluences

The standard approach to calculating fluences (e.g. Yau et al. [1985]; Abe et al. [1996]; Peterson et al. [2001]) is to simply divide the whole polar cap (above 60°) up into smaller regions, calculate the mean flux in each region, and multiply by the regional area to get the fluence:

$$F_{region} = \int_{region} J dA \approx A_{region} \bar{J}. \quad (4.1)$$

Total fluence from the entire polar cap is simply the sum of the regional fluences:

$$F = \sum_{region} F_{region}. \quad (4.2)$$

This calculation assumes that the sampling is unbiased only within each region, and does not require unbiased sampling of the entire space. As long as the regions are well-chosen, this method is simple, and gives a reliable unbiased estimate of the

average total fluence. Moreover, if the regions are chosen so that points within a region are statistically more similar to each other than to points outside the region, then the statistical uncertainty will also be reduced. Data can be sorted into categories by parameters of interest, and trends can then be found by comparing these categories.

The one major problem with this method is that because of the inherent temporal averaging, it does not in any way address the issue of the variance of the *instantaneous* fluence. That is, at every moment in time, the fluence is a well-defined quantity, but the above analysis gives only the mean of this quantity averaged over time under similar conditions. But how much could the instantaneous fluence vary from this mean? For example, if the average fluence is 10^{25} s^{-1} , would it be unusual for the instantaneous fluence F to be $5 \times 10^{25} \text{ s}^{-1}$? What about 10^{26} s^{-1} ? Such questions are critical for the assessment of the total ionospheric outflow.

The solution to this problem is not straightforward. There is no clearly-established method to use, and the lack of any multi-point measurements makes any answer somewhat uncertain. The method I have used is a Monte Carlo resampling scheme that takes into account the sizes of self-similar regions (“cells”), and is described in detail in 4.5.

Another, more surprising, problem is the estimation of errors for the average total fluence. Typically, the measurements have been treated as independent, and the uncertainty in the mean reported as $\sigma_{\bar{F}} = \frac{\sigma}{\sqrt{N}}$. However, this ignores the auto-correlation of the measurements, and therefore *significantly underestimates* the true uncertainty. This will be dealt with in section 4.4.

4.3.1 Division of the Polar Ionosphere into Regions

For the simple fluence-estimation method used in equations 4.1 and 4.2, as well as for the more elaborate method of section 4.5, it is necessary to divide the total region up into smaller (hopefully more statistically-uniform) regions. In this study, the polar region was divided into 10 regions, as shown in figure 4.2.

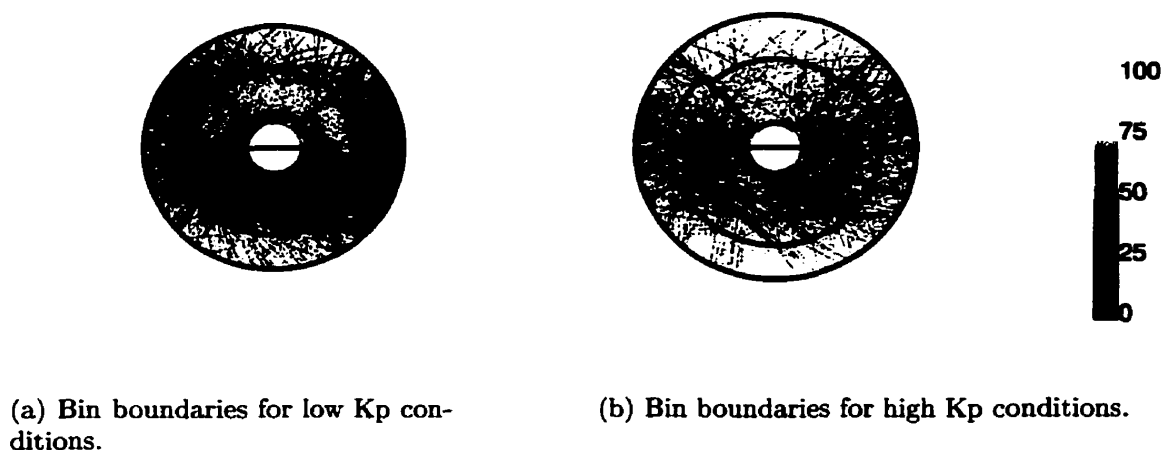


Figure 4.2: Polar cap regional boundaries for low Kp (a) and high (b) Kp conditions. Points shown are colour-coded observations of upward flux, and have invariant latitudes truncated at 85 degrees. Colour coding is by percentile. The top of the figure is in the sunward direction.

The boundaries of the bins were defined by examination of upward flux values, as in figure 4.2. The 10 regional bin boundary locations are functions of Kp, and generally correspond to known divisions of the ionosphere. Divisions are based, however, on observed changes in the character of the upward H^+ flux values and not on preconceived notions of where the bin boundaries should be based on other processes. Differences between these boundaries and more commonly used ionospheric regions

are primarily due to the high altitude of the observations. Oxygen bin boundaries seen in the data coincide with hydrogen bin boundaries.

Bins 1 through 4 are in the auroral zone, and are divided into day, night, dawn and dusk. Different processes are expected in each of these bins. Bin 5 contains the cusp. Bins 6 through 8 each contain some area that would be termed auroral zone and some area that would be termed polar cap. Bins 9 and 10 are polar cap bins. Note that in periods of enhanced convection, material from the cusp can be found “blown” into bin 9 by the $\vec{E} \times \vec{B}$ drift.

As stated above, the exact locations of the bin boundaries are functions of the magnetic activity, as gauged by Kp. This reflects the well-known fact that the auroral oval (the region in which aurora is expected) expands under enhanced magnetic activity. The exact region boundaries are given in table 4.2.

Region	Minimum ILAT	Maximum ILAT	MLT 1	MLT 2
1	65 - scale	74 - scale	9	15
2	65 - scale	72 - scale	4.5	9
3	65 - scale	72 - scale	19.5	4.5
4	65 - scale	72 - scale	15	19.5
5	74 - scale	83 + scale	9	15
6	72 - scale	81 + scale	4.5	9
7	72 - scale	81 + scale	19.5	4.5
8	72 - scale	81 + scale	9	19.5
9	81 + scale (see text)	90	6	18
10	81 + scale	90	18	6

Table 4.2: Regional boundaries for fluence analysis.

where

$$scale = 0.66 \overline{Kp} - 1. \quad (4.3)$$

Note that region 9 has an extra piece missing due to region 5 (as shown in figure 4.2). The minimum latitude of $65 - scale$ is higher than many similar studies, leading to a somewhat smaller total area. However, data below this latitude were frequently found to be contaminated by the radiation belts, and were therefore unusable in any statistical study.

The number of bins is much smaller than the number of bins typically used for similar studies (see, e.g. Norqvist et al. [1998]; Peterson et al. [2001]). However, it was found that the statistical errors grew too large for the analysis of section 4.5 if the area was divided into smaller regions than those presented. Since the estimation of the range of outflow levels was deemed an important goal, the binning was made coarsely, with the Kp-adaptive features discussed above. Moreover, the statistical fluctuations in the net flux are smaller for the larger, higher energy ranges upon which similar studies have focussed their attentions, which allows the use of smaller bins.

4.4 Error analysis of fluence estimates: Is there a significant trend?

Error analysis for the simple fluence estimator $\bar{F}_{region} = A_{region} \bar{J}$ is surprisingly complicated. The complication arises from the fact that the data are *not* independent. If they were independent, the central limit theorem implies that the estimate of \bar{J} , $\sigma_{\bar{F}}$, should be distributed as a Gaussian with a mean equal to the population mean and

a standard deviation of $\sigma_{\bar{F}} = \frac{\sigma}{\sqrt{N}}$. Appropriate error bars could then be constructed easily from a table of the normal distribution.

Each data point is *not*, however, independent. Flux values measured close together temporally are likely to be similar. In general, the data tends to arrange itself into clusters of values that are self-similar. This is exactly what one would expect physically; the processes that control the plasma populations work over large distances.

This grouping tendency results in a poorer estimate of the mean than if the tendency were not there. For comparison, consider a system that returns uniform random numbers between 0 and 1 in groups of 10. That is, the first measured value is chosen from $U([0, 1])$, the uniform distribution on $[0, 1]$. The next nine values are the same, then the eleventh is again chosen from $U([0, 1])$. Values 12 through 20 are equal to value 11, and so on. A set X of N values are selected in this way, and the mean is computed. Clearly, the uncertainty in this mean is not $\frac{\sigma}{\sqrt{N}}$, but rather $\frac{\sigma}{\sqrt{N/10}}$.

The situation in the data set of flux values is similar, except that the factor of 10 is not so easily computed. The following subsections present a method by which a meaningful uncertainty estimate can be determined.

4.4.1 The Bootstrap

In preparation for the next section, which will deal with a technique for estimating $\sigma_{\bar{F}}$ in context of the flux observations, I would like to introduce the concept of a simple bootstrap error estimate. The bootstrap technique, pioneered by Efron [1979], is a very general nonparametric technique for estimating uncertainties in

statistical estimators. Although exceedingly simple in basic principle and design, the bootstrap is surprisingly general and has been the subject of vigorous debate amongst statisticians since its inception.

Consider a random sample of n values $X = x_1, x_2, \dots, x_n$, taken independently from a population $F(x)$. A parameter Θ is to be estimated using the statistical estimator $\hat{\Theta} = \hat{\Theta}(x_1, \dots, x_n)$. There are effectively no restrictions on $\hat{\Theta}$ (see Hjorth [1994]). It could be as simple as the mean or the median, or as complicated as deemed necessary for the problem at hand.

Θ is first estimated in the normal manner using all of the available data. Next, a *bootstrap sample* of n values

$$X^* = X_1^*, X_2^*, \dots, X_n^*, \quad \text{where } X_i^* \in X \quad (4.4)$$

is randomly drawn *with replacement* from the sampled values X (recall that n is the number of original samples). Note that this means that one data value may contribute more than once to the bootstrapped sample, while others may not contribute at all. A new estimate of Θ is then computed from X^* :

$$\hat{\Theta}_1^* = \hat{\Theta}(X_1^*, \dots, X_n^*). \quad (4.5)$$

The process of bootstrap sample selection and estimation is then repeated B times ($B \gg 1$), yielding B estimates of $\hat{\Theta}^*$.

The distribution of $\hat{\Theta}^*$, computed through the bootstrap repetitions, asymptotically converges to the sampling distribution of $\hat{\Theta}$ and $\hat{F}(\hat{\Theta}^*)$ is consistent for $F(\Theta)$ under certain conditions (see Efron [1979]). In particular, confidence intervals com-

puted for $\hat{\Theta}^*$ asymptotically converge to confidence intervals for $\hat{\Theta}$. Therefore, once the bootstrap replications have been performed, the uncertainty in $\hat{\Theta}$ is fully characterized (in the limit of a large number of sample points).

There are many more uses for the bootstrap. For example, by comparing $\hat{\Theta}$ with the mean of the bootstrapped estimates $\sum_{i=1}^B \hat{\Theta}_i^*/B$, an estimate of the bias can be obtained. A good review of the bootstrap is given in Efron and Tibshirani [1993].

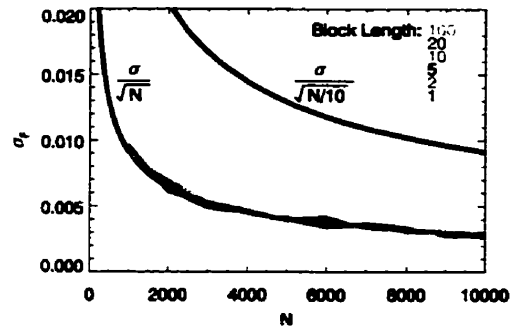
4.4.2 The Block Bootstrap

In the previous section(4.4.1), the sample population X was drawn *independently* from $F(x)$. I would now like to turn to the case of dependent sampling.

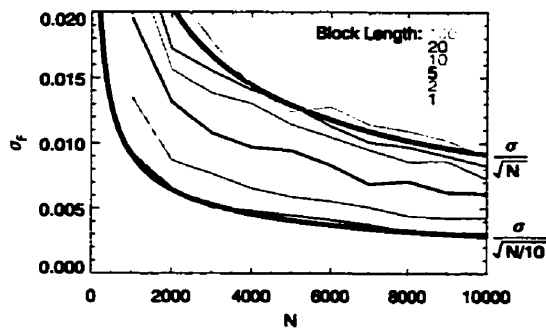
Consider once again the simple system discussed in section 4.4 that repeats one random number 10 times, then another one 10 times, and so on, and where the statistic of interest is the arithmetic mean, μ . A standard bootstrap interprets each data point as a completely independent observation, and gives excellent agreement with the (incorrect) normal theory error estimate $\frac{\sigma}{\sqrt{N}}$. This is shown in figure 4.3a as the red line.

Imagine now a variation on the bootstrap, however, whereby data is selected in blocks of ℓ consecutive data points each, rather than one at a time. As in the normal bootstrap, the total number of data points selected is equal to the total number of sample points (i.e. k blocks are selected, where $k\ell = n$), and blocks are selected with replacement. This is known as a block bootstrap, and seems to have been first discussed by Künsch [1989].

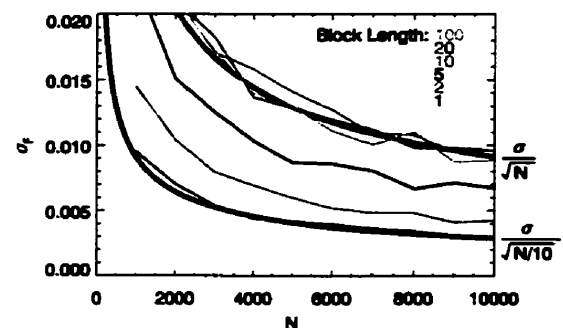
Figure 4.3a shows the results of a block bootstrap analysis on 10 data sets ranging from 1000 to 10000 data points each. The data sets were constructed by in-



(a) Independent data



(b) Repetitive data



(c) Repetitive data with cell alignment

Figure 4.3: Performance of the block bootstrap on synthetic data. The thick black lines mark $\frac{\sigma}{\sqrt{N}}$ and $\frac{\sigma}{\sqrt{N/10}}$, while the coloured lines mark $\sigma_{\bar{F}}$ as a function of the number of points. Different coloured lines indicate different block lengths. Panel (a) shows the block bootstrap used on independent data. In this case, regardless of the block length, the technique reproduces the correct normal theory estimate. Panel (b) uses non-independent data of the kind discussed in the text (repetitions in blocks of 10). At a block length of 1, the technique converges to the incorrect result $\sigma_{\bar{F}} = \frac{\sigma}{\sqrt{N}}$. As the block length increases, the curve approaches the correct result of $\sigma_{\bar{F}} = \frac{\sigma}{\sqrt{N/10}}$. Panel (c) shows how convergence can be enhanced by aligning the blocks with breaks in the data.

independently sampling from $U([0, 1])$. 300-iteration block bootstrap analyses were performed for each data set, with block lengths from 1 to 100. Thick lines have been drawn showing $\frac{\sigma}{\sqrt{N}}$ (the normal theory estimate) and $\frac{\sigma}{\sqrt{N/10}}$ for reference. For independent data, the block bootstrap gives an excellent estimation of σ_F as long as the block size is small compared to the sample size.

Figure 4.3b shows the performance of the block bootstrap with dependent data of the type discussed above, where every tenth data point is chosen at random from $U([0,1])$, and is then repeated 9 times. With a block size of 1 (i.e. a standard bootstrap), the estimate agrees with $\frac{\sigma}{\sqrt{N}}$. As the block size increases, the error estimate converges to the correct value of $\frac{\sigma}{\sqrt{N/10}}$.

If there is some way to align the blocks used for the bootstrap replication with the “blocks” in the data (in this case, to start each block one past an integer multiple of 10), the rate of convergence is increased. Figure 4.3c is the same as figure 4.3b, except that the bootstrap blocks have been aligned with the data.

4.4.3 Trend Analysis in the Fluence Data Using the Block Bootstrap

Various block bootstrap analyses of the net oxygen flux were performed, using different block lengths. As with the synthetic data, a consistent solution was asymptotically approached as the block length increased. This asymptotic solution was determined graphically, and was larger than the simple $\frac{\sigma}{\sqrt{N}}$ estimate by roughly a factor of 5. Block lengths of at least roughly 50 were required, providing the blocks were not allowed to span more than one orbit. If this condition was not applied, the technique generally failed. Eventually I decided to treat each orbit as a unit in the block bootstrap.

The number of bootstrap replications used was 300. Confidence intervals were extracted by taking the bootstrap replicate values of \bar{F} that fell at the required percentiles. These parameters (300 replications, using orbits as blocks) were used for all block bootstrap analyses that are discussed after this point in this work. Particularly, all bootstrap analyses reported in chapter 5 use these parameters.

Accurate uncertainty estimates are crucial when assessing trends seen in the data. Figure 4.4 examines 2 potential trends. Figure 4.4a looks at the net oxygen fluence, calculated by equations 4.1 and 4.2, as a function of the second of the minute when the measurement was taken. Although there is a 10% difference between the highest and lowest points, it is clear that there is no significant trend. Figure 4.4b, on the other hand, shows a clear dependence on the magnetic activity index Kp.

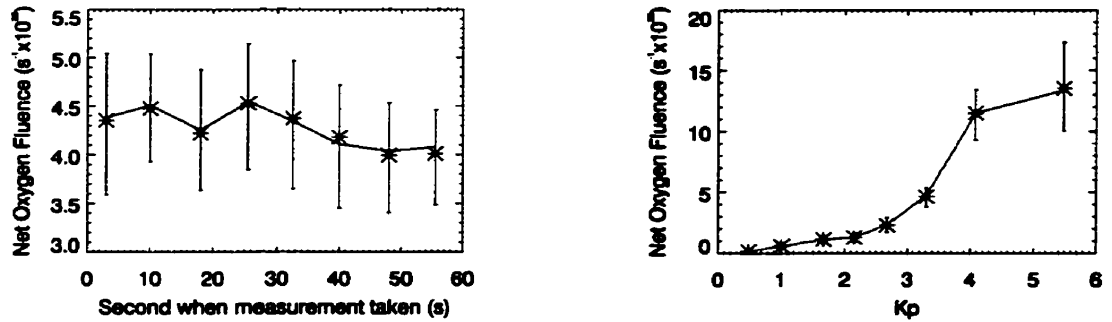


Figure 4.4: Net oxygen fluence as a function of a) second of the minute when the measurement was taken and b) Kp. Error bars are 95% confidence intervals estimated using bootstrapping. Lines for trends that are statistically significant from the following point at the 95 % level are marked in red. Stars mark the bootstrapped means (i.e. $\hat{\Theta}^*$), while the lines cross the error bars at the best estimate of the fluence (i.e. $\hat{\Theta}$).

4.5 Calculation of “Instantaneous” Fluence

For the problem of characterizing the ionospheric fluence, the mean fluence is not entirely sufficient. If the results are to be used to assess possible contribution to magnetotail dynamics, it is important to be able to assign probable upper and lower bounds on the fluence. Basically, is the system capable of supplying substantially more than the average ion flow?

It will be helpful to consider the two limiting cases. In the first limiting case, the flux is effectively constant across the entire extent of the polar ionosphere. In this case, $F = A_{region}J$, and the distribution of fluence values is simply the distribution of flux values multiplied by a scale factor. Using this model, without subdividing into regions, the mean total upward O^+ fluence would be $3.2 \times 10^{25} \text{ s}^{-1}$, but could vary (95 % confidence) between 0 and $4.0 \times 10^{26} \text{ s}^{-1}$. At the other extreme, if the polar ionosphere consisted of millions of tiny, independent cells, then any fluctuations would be averaged out, and the fluence would never vary substantially from the mean.

Clearly, neither of these limiting cases are physically reasonable. However, given the relatively large data set available, it would seem reasonable that some estimate could be made of how spatially variable the outflow is, and thereby reach an estimate for bounds on the instantaneous fluence. What is needed is an idea of how the system organizes itself. The flux measurements tend to be organized into “cells” that have a similar character for a number of records; the essential questions, then, are how large are these cells, and how are they related to nearby cells?

Ideally, two dimensional images of the ion outflow could clearly elucidate the spatial structure. What is available, however, are measurements on a one-dimensional

track that takes a finite length of time to traverse. Fortunately, the Akebono satellite transits the regions described in section 4.3.1 relatively quickly; less than ten minutes is typical. Judging from both ground-based observations and other satellite observations, it is certain that the system can change somewhat on time scales of this length, but also highly unlikely that it could frequently change dramatically at this time scale. I will therefore make the assumption that the system does not change significantly in the length of time it takes for the satellite to traverse one region. Certainly, there will be times when this is not true. However, this assumption should be valid for the vast majority of cases. Future work in this area may lead to more sophisticated treatments, but for this first attempt, this seems a reasonable starting point.

It is then necessary to unfold the one dimensional information from the satellite track into a two-dimensional picture of the cell sizes and relations. This is an example of a class of mathematical problems known as stereology. The simulation model will be described in section 4.5.4. First, however, I will describe the cellular structure seen in the data.

4.5.1 Definition and Detection of Plasma Cells

For estimating the variability of the instantaneous fluence, the most important characteristic of the data is its ability to organize itself into cells of similar flux values. A greater degree of self-organization means, perhaps counter-intuitively, a larger variability in the flux. It was therefore necessary to develop an algorithm to search through the data and find regions that were self-similar, which I refer to as cells.

The procedure by which cells were found was relatively simple. Cells were defined

as having the following characteristics:

1. A minimum length of 3 records.
2. A maximum allowed difference in the net flux from one record to the next within the cell of either 8 percentage points or $1 \times 10^5 \text{ s}^{-1}\text{cm}^{-2}$, whichever is greater.
3. A maximum time difference from one record to the next within the cell of 64 seconds.³

Regions matching these criteria and of length 3 records were first found, and then suitably joined together to maximize the length of the cells while subject to the above conditions. In cases where two cells could be joined by excluding one point in between them, this was done. Cells were determined independently for H^+ and O^+ , although the two generally coincided. Figure 4.5 shows a sample of data, with cells marked.

One problem with the cell detection method can be seen in the fourth cell marked in figure 4.5. In that cell, a significant upward trend can be seen inside the cell. It is then arguable whether this should be treated as one cell or several. Since the behaviour within such cells was likely caused by the same mechanism, it was decided not to break up cells like this.

Other methods for defining and detecting cells were tried. One promising method that gave similar results to the current one was to correlate the power spectra in a running window. Sudden changes in the power spectrum marked cell boundaries.

³SMS mode 2a data is sampled every 8 seconds. However, there are periods when the data is discarded as contaminated.

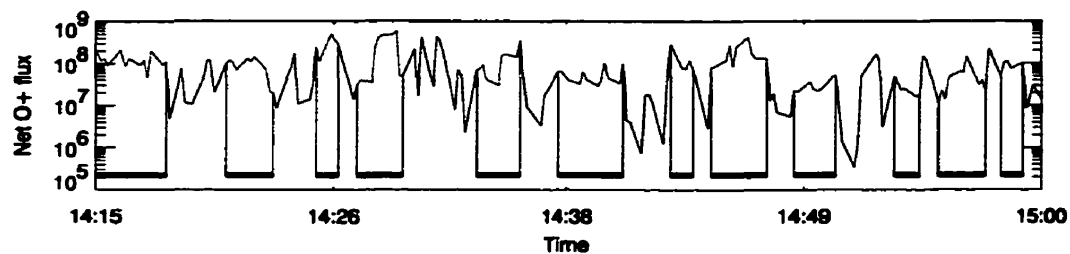


Figure 4.5: Cellular structure seen in the SMS O^+ net flux data. This data is taken from March 23rd, 1990, and shows a section of the pass when the satellite passed just northward of the expected cusp location. Cells, as determined by the search algorithm described in the text, are marked. Time is in hours.

Another method was to analyse the autocorrelation function. However, the current method was deemed equally (or more) effective, and simpler, than any of the other methods.

4.5.2 Cell Areas and the Wicksell Problem

Once the cells had been identified using the above method, the next issue was the stereological “unfolding” problem of how to infer 2-dimensional cell areas from the one-dimensional cell intersection lengths. For example, if the satellite encountered a cell of 400 km in length, what is the probable area of that cell?

The answer to that question clearly depends on the shape of the cell, which is an issue that will be dealt with in section 4.5.3. For now, assume that the cells are circular. The problem then assumes a form identical to a classic stereology problem first discussed by Wicksell [1925].

Let $f(x)$ be the probability distribution of cell diameters, and let $g(y)$ be the measured probability density of intersection lengths (chord lengths). If the cell is of diameter x , then the conditional probability density for observing a chord of length

y is

$$p(y|x) = \begin{cases} \frac{1}{x} \frac{y}{\sqrt{x^2-y^2}} & \text{if } y < x \\ 0 & \text{otherwise} \end{cases} \quad (4.6)$$

Then, using the total law of probability

$$p(A) = \sum_B p(A|B) p(B) \quad (4.7)$$

$g(y)$ is found by

$$g(y) = m^{-1} y \int_y^\infty (x^2 - y^2)^{-1/2} f(x) dx \quad (4.8)$$

where $m = \int x f(x) dx$ is the mean cell diameter. This is an Abel type integral equation, with inverse [Hall and Smith, 1988]

$$f(x) = -\frac{2m}{\pi} \frac{d}{dx} \left\{ \int_x^\infty (y^2 - x^2)^{-1/2} g(y) dy \right\}. \quad (4.9)$$

The integral in equation 4.9 has an analytic solution for $g(y) = \frac{1}{y^n}$, where n is an integer greater than zero. Note that since the mean cell diameter $m = \int x f(x) dx$ is required to be finite, the $n = 1$ term must be discarded, and a lower limit on the cell size must be imposed.

Figure 4.6 shows a histogram of the hydrogen cell sizes from the full data set. The red curve is a fit to the data of the form $f(x) = \sum_{i=2,3,4,5,6} \frac{c_i}{x^i}$, with a chi-square statistic of 1.15 on 77 degrees of freedom. This form was chosen because the solution is known (see previous paragraph), and it can adequately fit the data. The truncation of the series at $n = 6$ was chosen because this is the shortest series such that the χ^2 statistic is acceptable.

The partially obscured green curve is $f(x)$, the probable distribution of cell diameters. It has been “unfolded” from the red fitted curve by the use of equation 4.9. That is, the red curve is the fit to the observed chord lengths, and the green curve is the unfolded distribution of diameters.

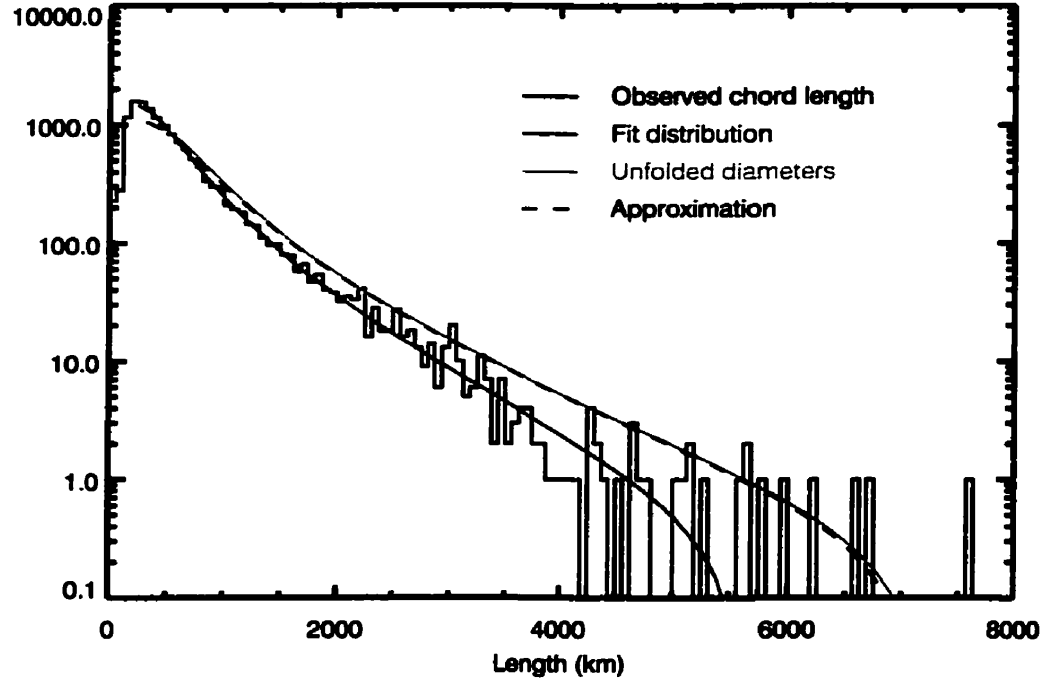


Figure 4.6: “Unfolding” the chord length distribution to a diameter distribution. The black histogram shows the observed chord lengths, while the red curve is the line of best fit to this histogram ($f(x) = \sum_{i=2,3,4,5,6} \frac{c_i}{x^i}$). The green and blue curves are the “unfolded” diameter distributions, which are, naturally, larger than the chord lengths. The green curve was unfolded using equation 4.9, while the blue curve uses equation 4.10.

The blue dashed curve is an extremely simple and intuitive approximation:

$$f(x) = g(x \alpha) \quad (4.10)$$

where α is the mean chord length for a circle of unit diameter: $\pi/4$. That is, if every observed cell chord length is simply multiplied by $4/\pi$, then the resulting distribution is an excellent approximation to the parent distribution of cell diameters (assuming circular cells).

4.5.3 Cell Shapes

Without 2-dimensional data, it is impossible to give a definitive answer as to the shapes of the cells. However, this is not considered to be a significant problem. First of all, the approximation 4.10 is reasonably robust with respect to varying cell shapes, as long as there is no consistent elongation in a direction defined with respect to the satellite path (as would be the case, for example, with auroral arcs). That is, if the cell orientations are random, and the shapes “reasonable”, then the approximation 4.10 is not a significant source of error when compared with other sources. For example, a Monte Carlo simulation of square cells yielded the approximation $f(x) = g(0.82 x)$, compared to $f(x) = g(\pi/4 x) \doteq g(0.79 x)$ for circular cells.

The issue of cell orientation can be resolved by comparing observed cell lengths on east-west passes through a particular region with cell lengths observed on north-south passes. Although this can only be done for the mid-latitude bins (due to orbital dynamics of the satellite), the observed cell size distribution was identical in both dimensions. In light of the above considerations, the simplest cell shape was chosen for the simulations: the circle.

4.5.4 Monte Carlo Estimation of Instantaneous Fluence

To create estimates of the instantaneous fluence, simulations were conducted whereby a given region was appropriately populated with cells, flux values were assigned to each cell, and the total fluence calculated. To conduct these simulations, a number of parameters had to be calculated from the data. These parameters are:

1. The joint probability of the cell size and flux.
2. The fraction of the total area occupied by cells.
3. The mean flux calculated from all observations that do not fall into cells.
4. The dependency of the flux in one cell on the flux in nearby cells.

Of these, the final item in the list is the most difficult to specify. A simple autoregressive scheme was attempted, but failed on a few issues. First of all, the extension of the time-domain technique of autoregression to the necessary two spatial dimensions is not a trivial task. Secondly, the autocorrelation function was found to be non-stationary. Finally, the autocorrelation function is often relatively constant (and large) from a lag of 1 up to the maximum lag possible for the orbit.

This final point implies that the process that tends to correlate one cell with its neighbour acts on a global scale. This suggests that what is needed is not an autoregressive model, but rather a model whereby a global state variable (or variables) sets the distribution from which individual cells are chosen more or less independently. Fortunately, it seems possible in this case to use state variables which can be independently observed. The magnetic activity index, K_p , and the solar activity index $F_{10.7}$ are a good choice. Selecting only data such that these parameters fall

in a limited range reduces the autocorrelation coefficients by a factor of 5. Although future work may incorporate a more sophisticated model, the model I will be using for calculations in the following sections treats each cell as independent. This will tend to *underestimate* the variability of the instantaneous flux⁴.

The first item in the above list also requires attention. To adequately specify a joint distribution function inherently requires much more data than to specify two one-dimensional probability distributions. The question, then, is whether the cell flux is a function of the cell size. Figure 4.7 shows the distribution of the mean flux observed in the cell given the intersected cell length (chord length), for all observed H⁺ cells:

$$P(F|x) = P(x, F)/P(x) \quad (4.11)$$

where x is the cell length and F is the fluence.

Two things can be seen from this figure. First of all, the cell flux is relatively independent of the cell size; $P(X|x)$ is uniform across all x values. Secondly, the full data set contains barely enough cells to adequately characterize the cell size / cell flux joint distribution function. The two variables were therefore treated independently.

For the Monte Carlo estimation of fluence, the following steps were required to initialize the simulations:

1. The distribution of cell intercept lengths was fit with an exponential distribution⁵.

⁴ Assuming a positive correlation between cells.

⁵ A lower cutoff threshold of 25 km was imposed for reasons of normalization of the distribution function. This cutoff value has little effect on the calculated fluence, and is much smaller than any cell that could be observed by the instrument.

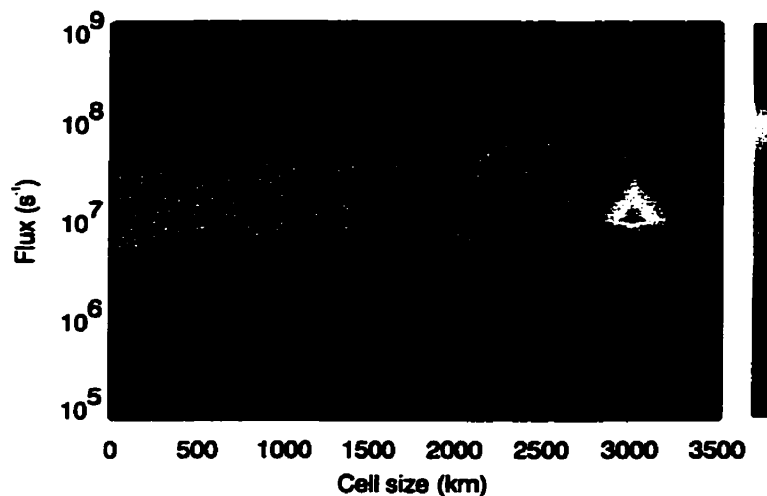


Figure 4.7: The conditional probability of upward H^+ flux given cell size. The colour scale is linear.

2. The distribution of cell sizes was determined using approximation 4.10.
3. The mean fraction of data points located in cells along the orbit within the region was found. This was typically about 45 %, with a very small variance.
4. The distribution of cell flux was determined numerically, and smoothed with a moving (boxcar) average of length 2 percentage points.
5. For each orbit, the mean of all points in the region but not in cells was computed. The mean and variance of these “interstitial mean fluxes” (which appeared Gaussian distributed) was calculated.

Then, to populate the region with cells and determine a fluence:

1. Cell sizes were chosen from the fit distribution until an area equal to 45% of the regional area was covered.

2. Each cell was independently assigned a mean flux using the numeric distribution of cell fluxes.
3. The total fluence from the cells was calculated as the sum of the cell areas times the mean fluxes.
4. The mean interstitial flux was chosen from a Gaussian curve with parameters based on the measured interstitial fluxes.
5. The mean interstitial flux was multiplied by the area of the region not contained in cells, and this quantity was added to the cellular fluence to obtain a total fluence.

This procedure was repeated roughly 5000 times in each region, thereby generating a probability distribution model for the instantaneous fluence. The distributions were typically non-Gaussian, with a longer tail at large fluence values. The mean and 95% confidence intervals were used to describe the distribution.

Chapter 5

Observations of Ion Outflow from SMS: Results

5.1 Factors that may affect ion fluence

The total ion outflow is not a random process. There are physical processes that drive the particle energization and physical processes that govern the number of particles available at typical energization altitudes. *A priori*, there are therefore certain factors that are expected to be correlated with the global fluence rate. For example, the solar Extreme Ultraviolet (EUV) flux is responsible for a large portion of the energy input to the ionosphere, and could therefore be expected to correlate with the global fluence.

Table 5.1 lists the factors that will be explored in this chapter, and gives a cursory explanation of why a relation might be expected. This is by no means an exhaustive list, nor do I believe an exhaustive list is even possible without decades of research. The reasons given in the final column are intended only as a potential justification for why these particular variables were examined, and do not imply anything further.

There are two questions to assess with regards to the relationship between an external factor and the observed flux. First of all, “is there a statistically significant relationship at all?”. This is assessed using the *uncertainty in the mean fluence*, which must be estimated by the block bootstrap technique of section 4.4.2. Secondly, “if there is a statistically significant relationship, how does it compare with the instantaneous variance?” This is assessed using the Monte Carlo technique outlined

Parameter	Section	Possible Connection with Fluence
Solar EUV flux F _{10.7}	5.2	Cause of photoionization and therefore ion formation. Affects ionospheric scale height and neutral atmospheric temperature.
Magnetic Activity K _p Dst	5.2 5.2.2	Related to parallel electric fields and wave activity in ionosphere. Affects centrifugal acceleration mechanism.
Solar Wind IMF Orientation IMF Magnitude Ram pressure Density Velocity	5.3.1 5.3.2 5.3.3 5.3.3 5.3.3	Primary energy source for the magnetosphere. Primary driver of ionospheric currents.
Season	5.4	Affects hemispheric energy budget. Modulates effectiveness of solar EUV flux.

Table 5.1: List of some external factors which may affect global fluence.

in section 4.5. In looking at the results in this chapter, it is critically important to remember the distinction between the *instantaneous variance* and the *uncertainty in the mean fluence*.

Some relations, such as the relation between K_p and fluence, are quite pronounced, and the significance of the trend is easily established. In such cases, I divided the independent variable (e.g. K_p) into a number of levels (typically 6), and estimated the instantaneous variance at each level. There are, however, more subtle trends, such as the trends seen with IMF orientation. For these trends, I again broke the independent variable into a number of levels, but focussed instead on the uncertainty in the mean fluence at each level. That is, for pronounced trends,

I have asked the question “how much could the instantaneous fluence vary about the observed relation?”, whereas for subtle trends, I have asked the question “is there a significant trend at all?”

5.2 Global Fluence as a Function of Magnetic and Solar Activity

The ions detected at Akebono have their source in the topside polar ionosphere, and must generally be energized in order to reach the high altitude of the satellite. The ionospheric conditions are modulated by the solar EUV flux, and the energization mechanisms are modulated by the electrostatic conditions present in the low-altitude magnetosphere. There are other factors, but these are perhaps the most primitive. It is therefore natural to seek a relationship between the fluence and measures of solar EUV flux and magnetic activity.

A convenient proxy measure of solar EUV flux is known as $F_{10.7}$. It is a measure of the solar flux at the radio frequency wavelength of 10.7 cm measured at Penticton, Canada, and closely tracks the EUV flux. The 11 year solar periodicity is clearly distinguishable; near solar minimum, typical values are about 75, whereas near solar maximum, typical values range from 180 to 270. At solar maximum, the 27 day periodicity can also be clearly seen (see figure 1.4).

A convenient measure of magnetospheric magnetic activity is known as Kp. It is derived from fluctuations in the magnetic field seen on the ground at mid-latitudes. It is a 3-hour average, and the index is given on a near-logarithmic integer scale ranging from 0 to 9. The index can be appended with either a ‘+’, a ‘-’, or nothing

at all (e.g. '2-', '2', '2+') to further refine the scale. Kp values of 0 or 1 reflect a quiet magnetosphere. Values of 2 or 3 reflect a moderately active magnetosphere, and values of 4 or above reflect high activity. Kp values of 7 or above are quite uncommon.

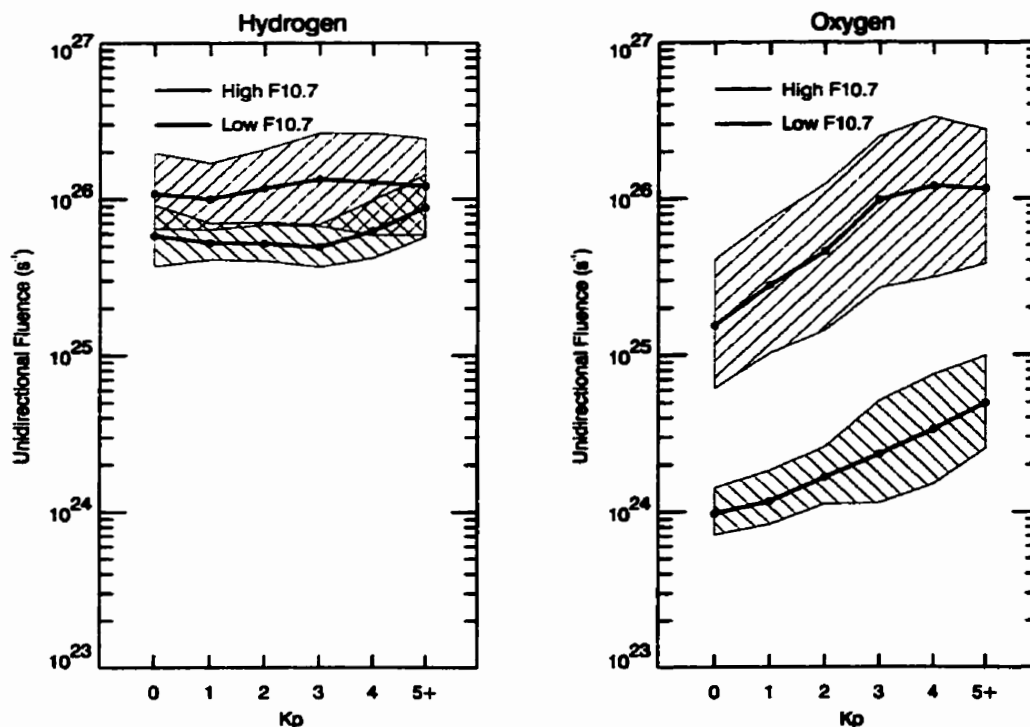


Figure 5.1: Relationship between Kp and upward O⁺ and H⁺ fluence for both solar minimum and solar maximum conditions. Thick solid lines are averages of binned data; shaded regions show the range of instantaneous variability based on the Monte Carlo simulations. Data is point-wise, in bins centred on integer values of Kp. Circles mark the bin centres.

Figure 5.1 shows the observed relationship between Kp and the total upward fluence at both solar minimum conditions ($F_{10.7} < 100$) and solar maximum conditions ($F_{10.7} > 150$). The mean outflow for the given conditions is given along with

the estimated instantaneous variance (5th and 95th percentiles from Monte Carlo simulations). It should be stressed that the main trend lines use all relevant data, and are independent of the Monte Carlo simulations. The variance is based on the Monte Carlo simulations.

Both the solar EUV flux and the magnetic disturbance affect the oxygen ions much more strongly than the hydrogen ions. Both indices cause the oxygen fluence to change by an order of magnitude, while the hydrogen fluence changes by at most about 50 %.

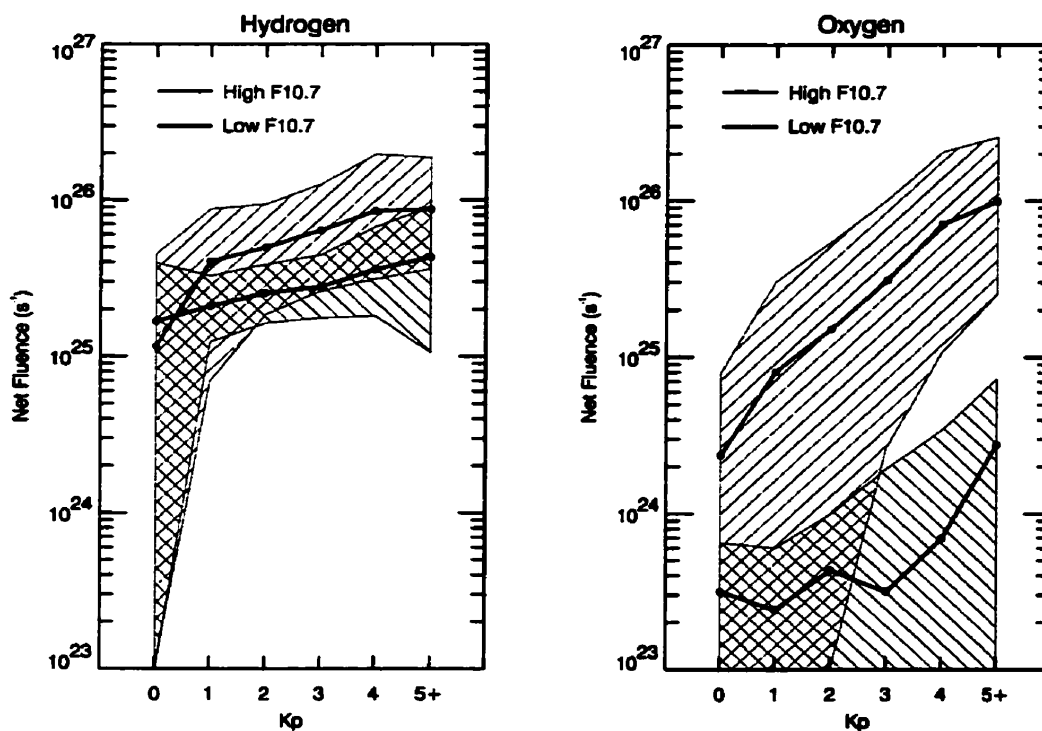


Figure 5.2: Relationship between Kp and net O⁺ and H⁺ fluence, in the same format as figure 5.1.

Figure 5.2 shows the effect of F_{10.7} and Kp on the total *net* fluence. Again, the

oxygen is much more variable. At solar maximum, the effect of Kp is to change the fluence by almost two orders of magnitude. The effect at low F_{10.7} is not quite as dramatic, but is still significantly larger than the roughly factor of two increase seen in the hydrogen. Again, both the mean and the instantaneous variability are given. Values less than zero have been plotted as 10²³.

Figure 5.3 shows the regional dependence of the flux. The four plots in the upper left of each figure show the relative contribution of each bin, after correcting for its area. That is, the colour is coded as

$$\frac{F_i}{A_i} / \sum_i \frac{F_i}{A_i} \propto J_i. \quad (5.1)$$

A few things about these plots are noteworthy¹.

1. For both species and under all conditions, the cusp contributes the largest fluence.
2. The dawnside auroral zone is also an important outflow region, especially for O⁺.
3. Changes in Kp do not affect the spatial distribution of either H⁺ or O⁺ outflow, other than to move the location of the auroral oval (i.e. bin boundary movement in section 4.3.1).
4. The cusp contributes a larger fraction of the O⁺ total fluence at solar maximum. No practical difference in regional distribution can be seen for H⁺.

¹These are observations only; no statistical test was applied.

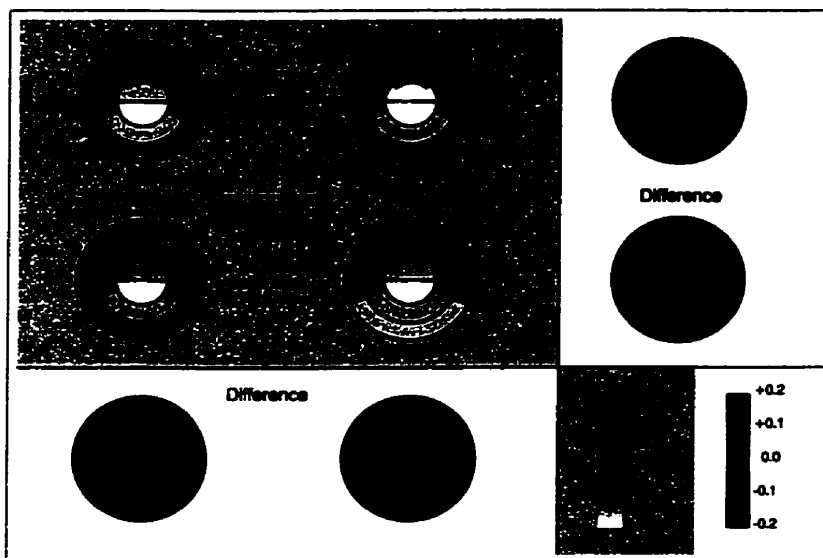
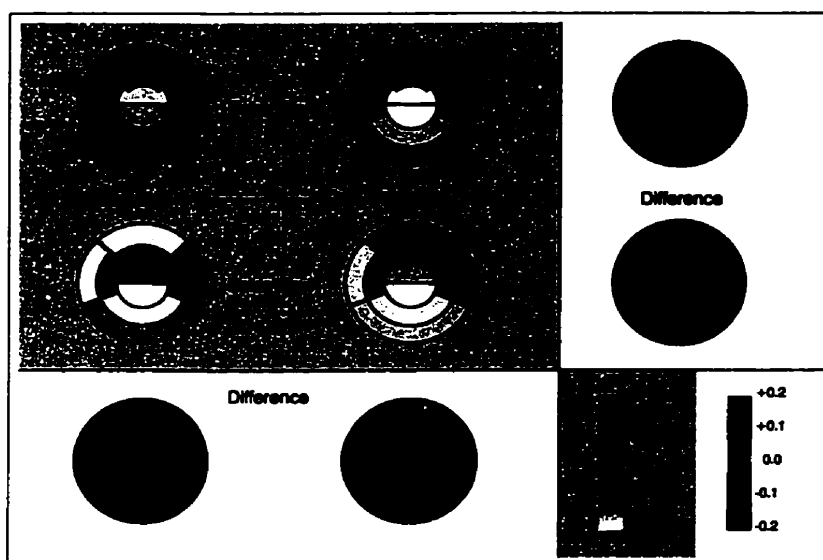
(a) Upward H^+ fluence.(b) Upward O^+ fluence.

Figure 5.3: Regional dependence of upward O^+ and H^+ fluence, as a function of K_p and $F_{10.7}$. The 4 plots in the upper left of each panel show the relative contribution of each bin. The scale on the left applies to these panels, and is dimensionless. The remaining plots show differences between the panels, using the scale on the right.

Region	Fractional Area	Fractional upward fluence		
		H ⁺	O ⁺ (Solar Min)	O ⁺ (Solar Max)
1	0.151	0.17	0.16	0.05
2	0.093	0.12	0.16	0.13
3	0.185	0.16	0.19	0.15
4	0.093	0.11	0.10	0.03
5	0.071	0.15	0.09	0.27
6	0.062	0.08	0.07	0.15
7	0.124	0.07	0.12	0.04
8	0.062	0.07	0.05	0.06
9	0.071	0.04	0.02	0.09
10	0.087	0.02	0.04	0.01

Table 5.2: Regional dependence of upward fluence for low Kp.

Tables 5.2 and 5.3 give the relative importance of each region for low Kp and high Kp conditions, respectively. The area of each region is expressed as a fraction of the total area. Likewise, the fluence is expressed as a fraction of the total fluence. Oxygen fluence is split for low and high $F_{10.7}$, although hydrogen fluence is not (due to the small variation).

5.2.1 Curve Fit to $F_{10.7}$ and Kp Dependence

The lines on figures 5.1 and 5.2 are roughly parallel, suggesting that the effects from changing Kp are separable from the effects from changing $F_{10.7}$, and that a solution of the form

$$F(F_{10.7}, Kp) = A f(F_{10.7}) g(Kp) \quad (5.2)$$

is possible. The one exception where this separation of variables is not expected to yield a good fit is in the case of the net O⁺ fluence, where the curve for high $F_{10.7}$

Region	Fractional Area	Fractional upward fluence		
		H ⁺	O ⁺ (Solar Min)	O ⁺ (Solar Max)
1	0.150	0.19	0.13	0.15
2	0.092	0.14	0.25	0.13
3	0.184	0.12	0.17	0.10
4	0.092	0.12	0.14	0.04
5	0.074	0.17	0.11	0.31
6	0.064	0.09	0.08	0.12
7	0.129	0.07	0.06	0.04
8	0.065	0.07	0.05	0.06
9	0.067	0.02	0.01	0.04
10	0.082	0.01	0.01	0.01

Table 5.3: Regional dependence of upward fluence for high Kp.

is not parallel to the curve for low $F_{10.7}$.

Furthermore, the Kp dependence follows a relatively straight line on the semi-logarithmic plots, suggesting $g(Kp) = \exp(C Kp)$. This form was fit using data from limited $F_{10.7}$ ranges, yielding consistently similar coefficients, and values of χ^2 such that $P(\chi^2 > \chi_{obs}^2) > 0.2$. The '+/-' modifications to the index were dealt with by adding or subtracting 0.3 to the value (e.g. '3-' becomes 2.7).

The Kp dependence could then be adjusted for, and the functional dependence of $f(F_{10.7})$ examined. The determination of the trend in $F_{10.7}$ is inherently a more difficult problem, as the question arises of whether the temporal evolution of the instrument calibration is reproduced by simply taking into account the MCP efficiency shown in figure 3.3. The curve is roughly exponential, but with a somewhat dubiously high point near $F_{10.7} = 150$. When points near this peak were excluded and an exponential curve fit, the χ^2 statistic was found to be acceptable. Below are the equations of best fit for the various fluences. Values of χ^2 indicate a good fit for

both upward fluences, and for net H⁺ fluence. The fit for net O⁺ is not as good, with a reduced χ^2 value of 3.5, with 6 degrees of freedom. Table 5.4 lists the coefficients for a fit of the form

$$F = a e^{b F_{10.7} + c Kp} . \quad (5.3)$$

Fitting was done with a gradient-expansion algorithm for a non-linear least squares fit. The method is based on one given in Bevington and Robinson [1992] (which is in turn based on Marquardt [1963]), and computes standard deviations of the fitted parameters.

Fluence	a	b	c
O ⁺ , unidirectional	$(1.9 \pm 0.2) \times 10^{23}$	0.025 ± 0.005	0.42 ± 0.15
O ⁺ , net	$(0.6 \pm 0.1) \times 10^{23}$	0.027 ± 0.002	0.53 ± 0.24
H ⁺ , unidirectional	$(2.7 \pm 0.1) \times 10^{25}$	0.008 ± 0.001	0.03 ± 0.09
H ⁺ , net	$(1.05 \pm 0.05) \times 10^{25}$	0.008 ± 0.001	0.18 ± 0.09

Table 5.4: Coefficients of best fit for fluence as a function of Kp and F_{10.7} . The functional form is $F = a e^{b F_{10.7} + c Kp}$. Standard deviations of the coefficients are given based on Marquardt method.

Or, dropping both the uncertainty estimates and any terms likely to be insignificant,

$$\begin{aligned}
 F_{O+,uni} &= 1.9 \times 10^{23} \exp[0.42Kp] \exp[0.025F_{10.7}] \\
 F_{O+,net} &= 0.6 \times 10^{23} \exp[0.53Kp] \exp[0.027F_{10.7}] \\
 F_{H+,uni} &= 2.7 \times 10^{25} \exp[0.008F_{10.7}] \\
 F_{H+,net} &= 1.1 \times 10^{25} \exp[0.18Kp] \exp[0.008F_{10.7}]
 \end{aligned} \quad (5.4)$$

5.2.2 Dst Dependence

Another measure of magnetic activity is Dst. Dst is an index calculated from magnetic fluctuations recorded at low-latitude observing stations. It responds more strongly to storm activity than Kp, but is less sensitive to higher-latitude phenomena such as substorms. Quiet time Dst values are greater than about - 20; disturbed conditions are below about - 40. Figure 5.4 shows the dependence of the upward fluence on Dst. The format is essentially the same as the format for figure 5.1. One minor difference is that Dst is continuous, whereas Kp is discrete. For figure 5.4, 15 Dst bins between -65 and 5 were created. Each bin contained the 15 000 points below the bin centre and the 15 000 points above the bin centre. Bins were allowed to overlap, so that the reported fluence is, in effect, a running average. The same 30 000 points were used for the Monte Carlo determination of the instantaneous variance as were used for the average. The similar instantaneous variance values when compared to the Kp comparison (figure 5.1) demonstrates that Dst performs as well as Kp as a predictor of upward flux. For O⁺ fluence estimation, either Kp or Dst must be combined with F_{10.7} .

5.3 Global Fluence as a Function of Solar Wind Parameters

An enduring question in the field of ion outflow study is the question of how much control the interplanetary magnetic field (IMF) has on the fluence. In general, periods when the IMF points in the southward direction ($B_z < 0$) tend to be associated with a more active magnetosphere. The reason for this is that magnetic reconnection is more effective when x-type reconnection can take place at the subsolar point,

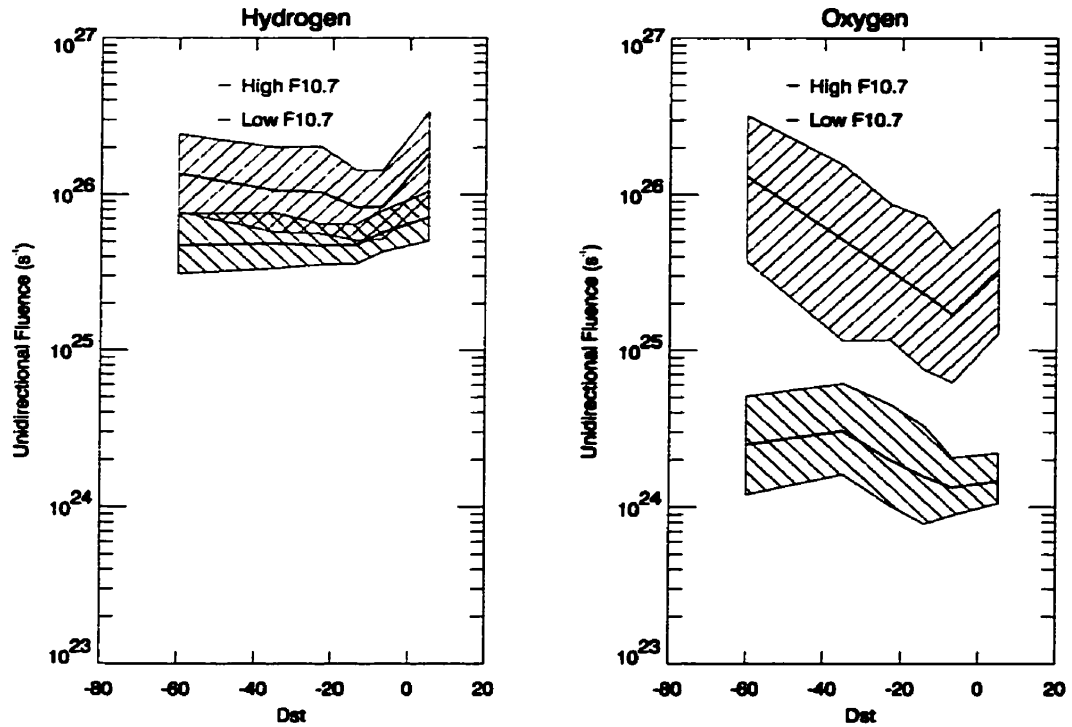


Figure 5.4: Dst dependence of the upward O^+ and H^+ fluence, in the same format as figure 5.1. A moving average has been used with a width of 30 000 data points.

which is only possible when the IMF is pointed southward².

Previous studies (e.g. Abe et al. [1996]) have tried to find a relationship between the z component of the IMF and the fluence, and have met with mixed results. Rather than examining the three components separately, I have chosen to analyse separately by the magnitude and the orientation. The orientation is given by two angles. The *clock angle* is the angle between the GSM z axis and the projection of the IMF on the y - z plane (i.e. $\tan^{-1}(B_y, B_z)$). The *cone angle* is the angle between the IMF and the GSM x axis. Clock angles near π , when in conjunction with cone angles near $\pi/2$, are associated with enhanced magnetospheric reconnection, and

²Lobe reconnection for northward IMF is not thought to be as efficient.

hence enhanced convection electric fields. It may thus be reasonably supposed that such conditions might lead to increased outflow. Since it will be seen that the trends are small, I have examined the behaviour by using the simple mean fluence estimator and the block bootstrap error analysis method.

Two other commonly used solar wind parameters are the solar wind velocity and density. With these two parameters, the *dynamic pressure* can be calculated. The dynamic pressure is the mechanical pressure exerted by the solar wind on the magnetosphere. It is equal to nv^2 , where n and v are the solar wind density and velocity, respectively. Occurrences of high dynamic pressure are often associated with magnetic storms.

5.3.1 Dependence on IMF Orientation

To search for IMF orientation effects, the effects of Kp and F_{10.7} were first removed by using the appropriate equation from equation 5.4 to scale each data point to the mean Kp and F_{10.7} conditions for the entire data set (Kp = 2.6 and F_{10.7} = 131)³. The data was then binned into eight groups by clock angle, with the bin sizes chosen so that each group had an equal number of data points. Error analysis was performed on each group using the block bootstrap method of section 4.4.3. 300 bootstrap replications were performed.

In none of the four cases (H⁺ and O⁺, net and unidirectional fluence) could a trend be seen. Furthermore, the null hypothesis that all eight groups were drawn from the same population was tested using a χ^2 test. Values for the reduced χ^2 statistic ranged from 0.17 to 1.4. There is therefore no reason to reject the null hypothesis in

³The analysis was also performed by correcting only for F_{10.7}, with similar results.

any of the four cases. *No statistically significant trend was seen relating the fluence to the clock angle.*

The data was then binned into only two bins: data for which the clock angle was within $\pi/4$ of northward and within $\pi/4$ of southward. The two cases were again compared with a χ^2 statistic, and again the null hypothesis could not be rejected. Based on the observed standard deviations, the test was powerful enough to detect differences as small as 10%. The result confirms that *if there is a difference in fluence between northward IMF conditions and southward IMF conditions, it must be less than 10%.*

A similar analysis was carried out with the cone angle. The results were slightly more ambiguous. There appears to be a weak tendency to lower fluence when the cone angle is small ($< \pi/4$). The trend appears in all four fluences (H^+ and O^+ , unidirectional and net), and is a factor of about 20%. These trends are barely deemed statistically significant by the χ^2 test, and should be treated with some skepticism.

Finally, a subset of the data was extracted such that the cone angle was between $\pi/4$ and $3\pi/4$. This subset was once again analysed for clock angle dependence. Again, no clock angle dependence was found.

5.3.2 Dependence on IMF Magnitude

A similar analysis to the orientation was carried out for the magnitude of the IMF. Again, 8 bins were used, with the same number of data points in each bin. The same χ^2 test of the null hypothesis as was described in the previous section was applied.

No trend could be seen in the H^+ data, and the χ^2 test indicated that the null hypothesis could not be rejected. The O^+ results, however, showed an increase in

fluence with increasing magnetic field strength. Figure 5.5 shows this trend for the upward fluence. Net fluence follows the same trend. Note that the effects of $F_{10.7}$ and K_p have been removed using equation 5.4. The reduced χ^2 value for the null hypothesis was 5.5 for 7 degrees of freedom, indicating rejection.

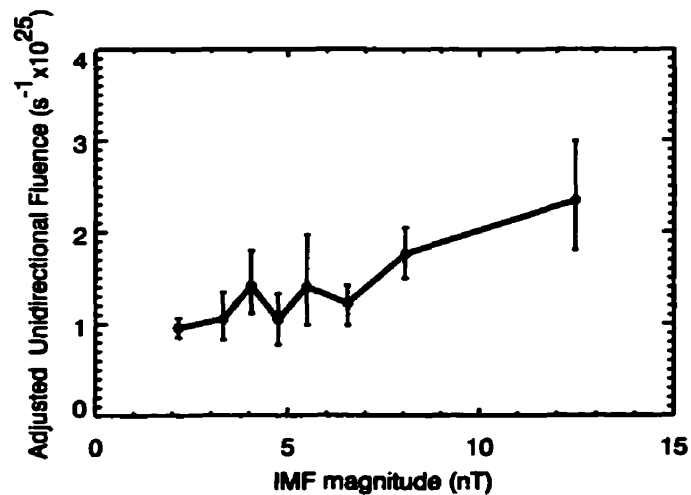
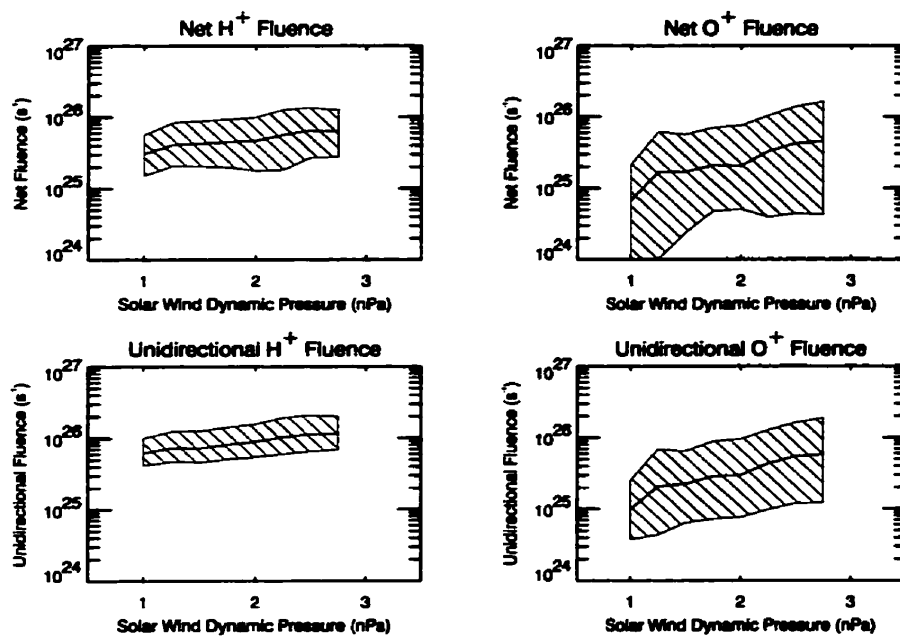


Figure 5.5: Upward O^+ fluence as a function of interplanetary magnetic field strength. Error bars are based on block bootstrap analysis, and mark 95% confidence intervals. The effects of $F_{10.7}$ and K_p have been removed.

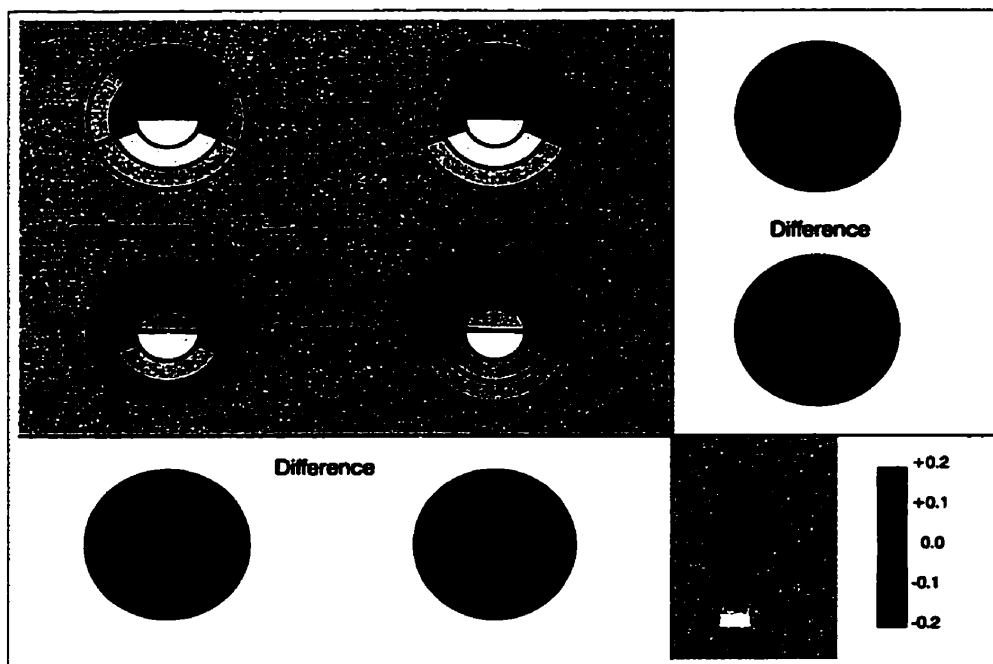
5.3.3 Dependence on Solar Wind Dynamic Pressure

The clearest relationship between the fluence and any solar wind parameter is the relation with the dynamic pressure. Figure 5.6 shows the observed trend, with instantaneous variance estimates from the Monte Carlo technique of section 4.5

The trends hold even when K_p and $F_{10.7}$ dependencies have been subtracted, although more strongly for H^+ than for O^+ (as the O^+ K_p and $F_{10.7}$ dependencies are stronger). In fact, it could perhaps be argued that the dynamic pressure is a better predictor of H^+ fluence than K_p . The relative importance of each region



(a) Net and upward fluences as a function of pressure.



(b) Regional dependence of the upward fluence, in the same format as figure 5.3

Figure 5.6: Dependence of H^+ and O^+ fluence on solar wind dynamic pressure. The format is the same as figure 5.4. Again, a 30 000 point moving average has been used.

remains unaffected by a change in the dynamic pressure, showing that it is a global change and not a frontside process, as might be expected. The relative importance of the cusp for O^+ outflow does, however, increase as the dynamic pressure increases.

The trends also hold independently for both the solar wind velocity and density; higher velocities and densities result in higher fluence. A reasonable correlation also exists with the solar wind electric field ($E_{SW} = v_{SW}B_{SW}$).

Figure 5.6b also shows an interesting difference between the hydrogen outflow and the oxygen outflow: the different relative strengths of the cusp. The cusp has a higher ratio of O^+ to H^+ than the rest of the ionosphere.

5.4 Seasonal Dependencies of Global Fluence

Given the dependence seen on $F_{10.7}$, it is clear that the solar EUV flux plays an important role in setting the outflow rates in O^+ , and a minor role for H^+ . It would therefore not be surprising if there were a dependence on season, as well.

Unfortunately, the Akebono orbit is not ideal for studying seasonal dependencies. The local time precession of the orbital plane is roughly 8 months, which means that the regional coverage is dependent on the month. For example, no passes through region 1 occurred in July. This creates biasing difficulties for the fluence estimator.

This problem can be partially eliminated by using fluence values that have been adjusted for $F_{10.7}$ and K_p . This was done; values were scaled to $K_p = 2.6$ and $F_{10.7} = 131$ using equations 5.4. However, the annual trend was not particularly clear when the year was broken into 8 groups. Therefore, the data was simply broken into two groups. The winter group covered the months from October to March (inclusive) and

the summer group covered the other months. Table 5.5 compares the two groups. Error analysis was done by block bootstrap. The error distribution was normal; two standard deviations are given as the uncertainty. The only statistically significant difference seen was in net H^+ fluence, which is higher in the summer by a factor of about 20%. I am somewhat skeptical of this result. The multiple tests performed in this section increase the likelihood of false positive identifications of differences (so-called “type I errors”). More work needs to be done on the seasonal effects.

	Adjusted Upward Fluence		Adjusted Net Fluence	
	H^+	O^+	H^+	O^+
summer	9.1 ± 0.8	1.6 ± 0.3	5.5 ± 0.4	0.9 ± 0.3
winter	9.2 ± 0.6	1.2 ± 0.2	4.3 ± 0.4	0.7 ± 0.1
difference	0.1 ± 1.0	0.4 ± 0.4	1.2 ± 0.6	0.2 ± 0.3

Table 5.5: Seasonal dependence of fluence. Confidence intervals are 2σ , where σ is obtained from the block bootstrap error analysis.

5.5 Summary of results

At the start of this chapter, table 5.1 listed a few of the factors that may influence the global fluence, and gave reasons why a correlation might be suspected. After examining each of these factors, I will conclude this chapter with a list of the observed trends. Table 5.6 lists the observed effect of each variable on the unidirectional fluence.

Parameter	Section	Size of effect on unidirectional fluence	
		H ⁺	O ⁺
Solar EUV flux F _{10.7}	5.2	Exponential dependence. Factor of ~2.	Exponential dependence. Factor of ~15.
Magnetic Activity Kp	5.2	No observed effect.	Exponential dependence. Factor of ~5.
Dst	5.2.2	No observed effect.	Factor of ~2 at low F _{10.7} . Factor of ~4 at high F _{10.7} .
Solar Wind IMF Orientation	5.3.1	No observed effect.	No observed effect.
IMF Magnitude	5.3.2	Factor of ~1.2.	Factor of ~2.
Ram pressure	5.3.3	Factor of ~2.	Factor of ~2.
Density	5.3.3	Factor of ~2	Factor of ~1.5.
Velocity	5.3.3	Factor of ~1.3	Factor of ~1.3.
Season Summer/Winter	5.4	No observed effect.	No observed effect.

Table 5.6: Observed factors affecting unidirectional fluence. Trend sizes reported are roughly between the 10th and 90th percentiles. Solar wind and seasonal trends have had the effect of Kp and F_{10.7} removed.

Chapter 6

Trajectories of Outflowing Ions

Once the ions have passed by the altitude of the Akebono satellite, there are a number of different scenarios which can occur. Ions that have a very low energy at Akebono are likely to be gravitationally trapped. Many of these ions will undergo “skipping” trajectories, whereby they will fall back toward the Earth, then be magnetically reflected back up to higher altitudes and repeat the process. Ions at higher energies at lower latitudes will travel on dipolar field lines to the opposite hemisphere before bouncing back. Higher energy ions at high latitudes may make it far back into the magnetotail, eventually encountering the central plasma sheet (CPS). It is these ions that are primarily of interest in the current study.

Ions that encounter the CPS more than $10 R_E$ tailward of the Earth will interact nonadiabatically with the tightly curved magnetic field in that region. In general, this interaction will energize and chaotize the particles, completely transforming the cold ionospheric plasma and mixing it with other plasma sources. After this interaction, the concept of ions of “ionospheric source” becomes murky at best. The characterization of the ionospheric supply of particles to the (mid-)distant magnetotail is thus best addressed by understanding the transport of this plasma to the furthest place where it is still conceptually a well-defined population: immediately before the first encounter with the CPS (this surface is sometimes termed the Plasma Sheet Boundary Layer (PSBL)).

6.1 Trajectory Tracing Technique

Rather than attempting to understand the behaviour of the ions during extremely dynamic conditions, I would like to concentrate on more typical conditions. I have therefore excluded any energization by transient processes (such as wave-particle interaction, field-aligned electric fields and time-varying electric and magnetic fields) that may be encountered between the ionosphere and the CPS. The fluxes and energies derived in this study therefore define the “zeroth-order” behaviour: the behaviour in reasonable, although stationary, electromagnetic fields. Differences between these and observed energies and flux patterns could provide evidence of wave energization and the effect of dynamic processes at the time of observation.

Ion trajectories were integrated using the complete first-order guiding centre equations of motion (equation 2.43) using a fourth-order Runge-Kutta-Fehlberg integration technique [Stoer and Bulirsch, 1993; Press et al., 1993]. Step size was determined adaptively with a tolerance of 0.01 %. Trials with other step sizes showed this to be a sufficiently conservative tolerance level.

The magnetic field was modelled by the long-tail version of the Tsyganenko [1987] field. This is a well-known empirical model that gives the external magnetic field¹ as a function of Kp and the dipole orientation of the Earth. An internal field must be added to this in order to obtain the total field. In this study, a dipolar field was used for the internal field, and the dipole tilt was always set to zero. Figures 2.4 and 2.5 show field lines and strengths traced using this field model.

The electric field was found by mapping the Weimer [1995] electric potential

¹The external field is the magnetic field generated by currents in the magnetosphere, as opposed to the *internal field*, which is the field generated by the Earth’s core.

model into the magnetosphere under the assumption of magnetic field line equipotentials. Rather than perform the computationally expensive task of tracing back three field lines for every step, a grid of electric field estimates was constructed prior to the particles being introduced to the system. Electric fields were then found using a cubic spline interpolation.

This electric field gridding technique greatly increased the computational speed, but inherently introduces some numerical errors into the field. Traces performed using the interpolated field from the grid were compared to traces performed by tracing back field lines to the ionosphere each time the electric field was needed. Although there were small differences in the paths, the parameters (energy, position, etc.) tabulated at the CPS were very similar.

The Weimer potential model uses spherical harmonic functions to fit an empirical electric potential to a large database of measurements. Inputs to the model are IMF magnitude and clock angle, solar wind velocity and the dipole orientation of the Earth. Figure 6.1 shows a map of the ionospheric potential for a southward IMF condition, with the typical “two-cell” pattern.

6.2 General Characteristics of the Trajectories

Figure 6.2 shows the trajectory of a typical oxygen ion originating from the dayside auroral zone and a typical hydrogen ion originating from the nightside auroral zone. The trajectories are overlaid on a magnetic map of the noon-midnight meridian, showing both the field lines and the colour-coded field magnitude. The trajectories are colour-coded by energy, which varies from 10 eV at the Earth to ~ 250 eV at the

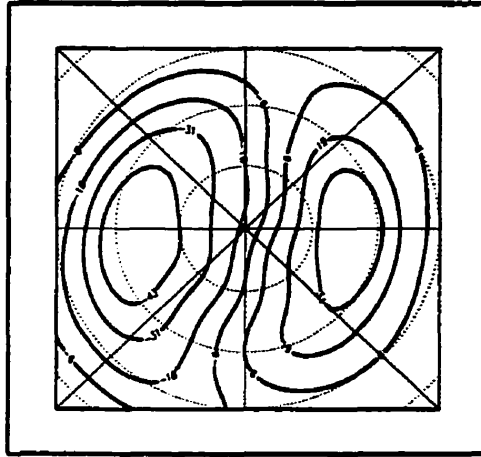


Figure 6.1: Electric potential contour plot of the high-latitude ionosphere under southward IMF conditions, using the Weimer [1995] model.

terminus of the oxygen trace, and ~ 35 eV at the terminus of the hydrogen trace. The travel time for the O^+ ion is approximately 3 hours, while the H^+ completes its path in about an hour. These parameters are highly dependent on the electric field, which was relatively small in the trace shown.

The O^+ ion starts from the dayside auroral zone at Akebono altitude with enough energy that it is not gravitationally trapped. As it travels up the field line, it is swept back toward the tail by the $\vec{E} \times \vec{B}$ drift. Initially, it is on field lines that close on the dayside, but eventually $\vec{E} \times \vec{B}$ drifts past the cusp and onto tail lobe lines. Note that if it had originated somewhat lower in latitude, or if the electric field were somewhat weaker, then it would not have reached the cusp. In this case, the trajectory would arc sunward, with the particle reaching the equatorial plane sunward of the Earth.

Once the O^+ ion passes the cusp, it begins to pick up energy by a process known as *centrifugal acceleration* [Cladis, 1986]. This is an acceleration in the parallel direction, given by term 4 in equation 2.43. In fact, it was subject to this acceleration



Figure 6.2: Trajectory of typical CPS-populating H^+ and O^+ ions, shown in the noon-midnight meridian. The O^+ ion originates in the dayside auroral zone, while the H^+ ion originates in the nightside auroral zone. The background shows the magnetic field lines, as well as the colour-coded field strength. The trajectory is colour-coded by energy.

before it reached the cusp as well, but the acceleration was in a direction such that it was losing energy. The centrifugal acceleration continues as the particle moves through the lobes. Eventually, the particle is moving at a roughly 45 degree angle to the field lines, with an energy of about 300 eV, when it encounters the CPS at a distance of slightly less than $40 R_E$ downtail and the tracing is stopped.

From this trace as a starting point, it is possible to look at the effect of changing initial conditions. If the initial magnetic latitude is decreased, the final position moves tailward until a point is reached where the particle does not cross the cusp. Conversely, if the latitude is increased from this initial position, the particle crosses the equatorial plane nearer to the Earth. If the energy of the particle is increased, it crosses the tail further and further back until eventually, as with position, it fails to cross the cusp and is swept to the dayside. In the limit of very high energy, the

guiding centre of the particle follows the field line to a high level of precision. If the initial energy is decreased, the particle crosses the equatorial plane closer to the earth. Changing the pitch angle has no effect on the trajectory.

The trajectory of the H^+ ion is quite different from the trajectory described above. For a hydrogen ion to have the same energy as an oxygen ion, its speed must be four times as great. Consequently, the H^+ ion travels much closer to the field line and is not nearly as affected by the $\vec{E} \times \vec{B}$ drift. Being on straighter field lines that do not cross the cusp, the centrifugal acceleration is less important, and it gains only a small amount of energy during its transit to the CPS (see Delcourt et al. [1994]; Delcourt [1994]).

One very interesting (and surprising) feature of this dynamic system is that all particles reaching a certain position in the tail have approximately the same velocity, regardless of their initial position and *velocity*. This is sometimes referred to as the *velocity filter effect* [Cladis, 1986], although it is usually applied only to particles originating from the same location. For example, there are other combinations of initial position and energy that would result in a particle crossing the tail at the same position as in figure 6.2. However, all of these combinations result in the same final energy. This is not entirely surprising, given that the initial energy is an insignificant fraction of the final energy. This makes it difficult, however, to trace particles backward in time from the tail to the ionosphere. A small change in the initial energy causes the mapping to go to an entirely different place in the ionosphere (or not to reach the ionosphere at all) . This type of backward tracing should only be done for high-energy particles, where this effect is not pronounced.

Equally interestingly, this self-ordering effect means that the population that

reaches a given location in the CPS can come from a wide range of initial energies, positions and pitch angles. This will have important implications in the next section.

6.3 Flux at the Plasma Sheet: Dependence on the Form of the Source Velocity Distribution Function

I stated in section 4.1 that the shape of the VDF is relatively unimportant in determining the supply of ions to the CPS. In this section, I explore this issue.

As briefly described above, the particles that populate a given location in the CPS come from a wide range of different locations, pitch angles and energies. Figure 6.3 shows the initial locations of all simulated O^+ ions that eventually reach the CPS within a box of area $4 R_E^2$ centred on $(-10, 2) R_E$. The conditions for the trace were low K_p , and southward IMF. All of these ions have a final energy of about 400 eV and a final pitch angle very close to 0. The left panel shows the initial position of the particles, colour coded by initial energy. The right panel shows the initial positions colour coded by initial pitch angle.

The population seen at the tail consists of particles that come from a wide variety of initial conditions. The (unidirectional) flux at the tail is therefore related to the sum of the differential flux under all of these initial conditions. Specifically, since the final position is not a function of the initial pitch angle, the flux seen at the tail is related to the flux at the ionosphere integrated over pitch angle. Moreover, since the initial energy in figure 6.3 spans the full thermal range (above a gravitationally-trapped cutoff), the flux distribution is actually averaged over a phase space hyper-volume that completely spans the pitch angle dimension, and lies at an angle in the

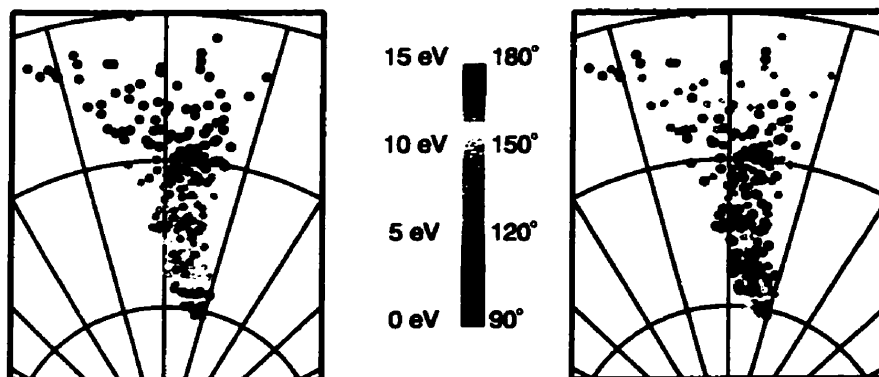


Figure 6.3: Locations, energies and pitch angles of O^+ ions that will eventually reach the plasma sheet near $(x, y)_{GSM} = (-10, 2)R_E$. Dots mark the initial geomagnetic condition, and are colour-coded by initial energy on the left and by initial pitch angle on the right.

energy and position dimensions such that all energies above a threshold are included in the averaging, although not independently of position. If it is assumed that the distribution in energy space is only a weak function of position on the scale size of the averaging, then it follows that *the flux seen at a given location in the tail is related to the mean upward flux integrated over the appropriate region of the ionosphere, and is independent of the shape of the velocity distribution function*. This is the key, in some sense, to the entire study. Without this averaging, the shape of the VDF would be required, thereby increasing the statistical demands on the data set beyond what it could adequately describe.

The conclusion that the distribution function is largely irrelevant was tested by assuming a variety of different forms for it and then calculating the resulting flux seen at the CPS using the tracing techniques described above. The simulations confirmed

that the only way to change the flux at the CPS was to change the total flux above the gravitationally-trapped threshold.

Another way to view this result is as a direct consequence of Liouville's theorem from statistical mechanics, which states that phase space density is conserved along a trajectory. In the case of ion outflow, the position space volume goes from a relatively small volume at the ionosphere to a much larger volume at the CPS. To conserve the density in phase space, this means that the velocity space volume at the ionosphere must be larger.

6.4 Simulation Method

A Monte Carlo method was employed to sample the velocity distribution functions at the ionosphere. Initial positions for the roughly 1 million test particles were chosen at random at an altitude of 8000 km, and initial velocities and pitch angles were randomly selected with a maximum velocity of 15 km/s for O⁺ and 60 km/s for H⁺ (19 eV).

Each trajectory was weighted by its upward flux, using the statistical model developed in chapters 4 and 5. The distribution was assumed to be a flowing Maxwellian with a flow speed of 5 km/s and a temperature of 5 eV. Although this temperature is slightly higher than the expected instantaneous temperature (see Abe et al. [1993]), it is consistent with the distribution obtained when a large number of measured VDFs are averaged together.

Trajectory traces were terminated when one of six conditions was met:

1. The particle became non-adiabatic. This was monitored by using the adia-

baticity condition $\kappa = \sqrt{\frac{R_c}{R_{Lmax}}} > 3$ [Büchner and Zelenyi, 1986; Delcourt and Belmont, 1998], where R_c is the radius of curvature and R_{Lmax} is the maximum Larmor radius. No particle was found to become non-adiabatic prior to encountering the CPS .

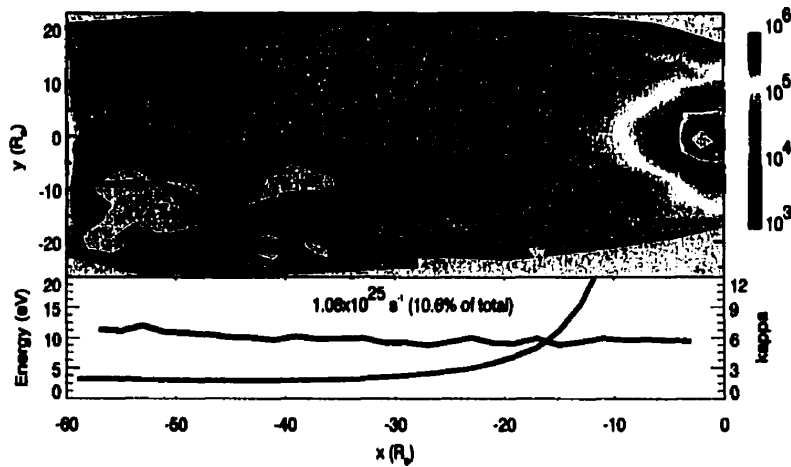
2. The particle reached a distance of more than $60 R_E$ downtail.
3. The particle was gravitationally trapped. A particle was deemed to be gravitationally trapped if either its altitude dropped below 600 km or if, after two hours flight time, it had not reached a radial distance of more than $2 R_E$.
4. The particle crossed the magnetopause, found numerically from the envelope of field lines traced from the Earth. No more than about 10 % of the trajectories were stopped for this reason.
5. The particle crossed the equatorial plane or entered the CPS. The upper boundary of the CPS was taken to be at $z = 3 R_E$ for $x < -15 R_E$, and at the plane $z = x/7.5 + 1 R_E$ inside of $-15 R_E$. This boundary corresponds, in the tail, to the location where particles begin to experience the intense acceleration characteristic of the CPS.

6.5 Ionospheric Flux Seen at the Plasma Sheet

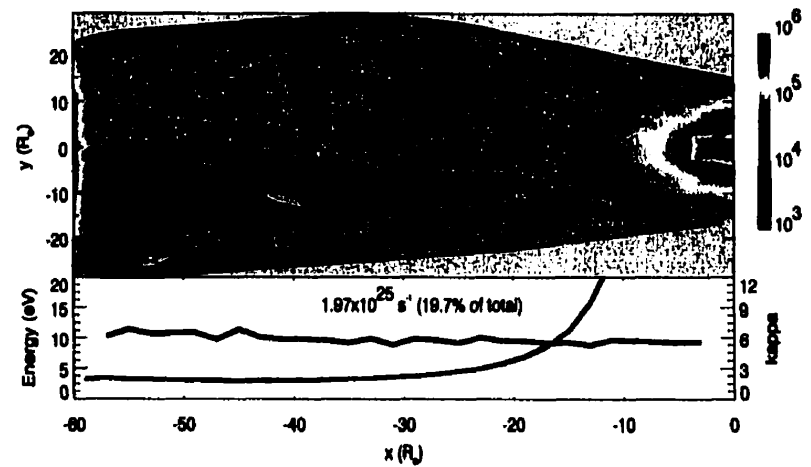
Trajectory simulations were conducted for four different electromagnetic field conditions, corresponding to Kp values of 1 and 5, and IMF clock angles of 0° (northward) and 180° (southward). The IMF magnitude was 8.0 nT for all traces, and the solar wind speed was 400 km/s. The weighting for the traces was consistent with solar

maximum conditions; solar minimum conditions show the same patterns, but with absolute flux values that are an order of magnitude lower. Hydrogen absolute flux values are lower by a factor of 2.

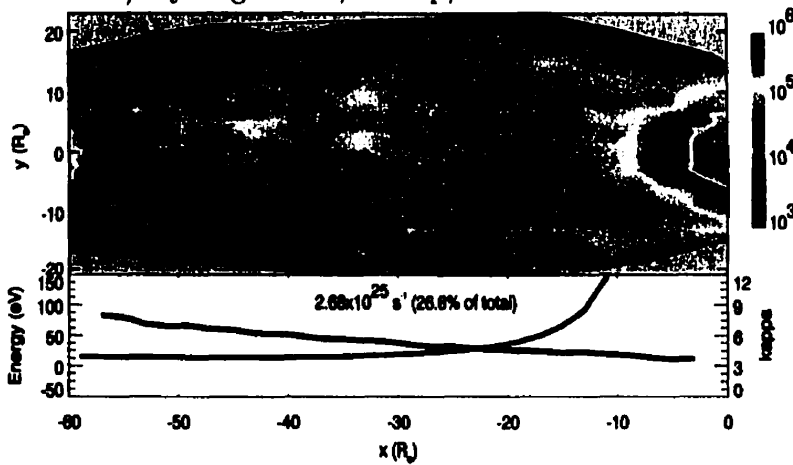
The unidirectional flux seen at the CPS was tallied for each simulation, and is shown in figures 6.4 and 6.5. Also shown are the mean energy and the adiabaticity parameter κ , calculated for particles within $10 R_E$ of the noon-midnight meridian. Where κ is greater than three, it is represented as a blue line; below three, it is red. Particles with κ less than three (in the red region) will interact nonadiabatically with the current sheet, and as such have a much greater ability to play a role in the dynamics of the CPS. The total fluence of such particles is printed on each figure. Note that particles are stopped at $-60 R_E$, so all flux tailward of $-60 R_E$ is included in the $x=-60$ bins.



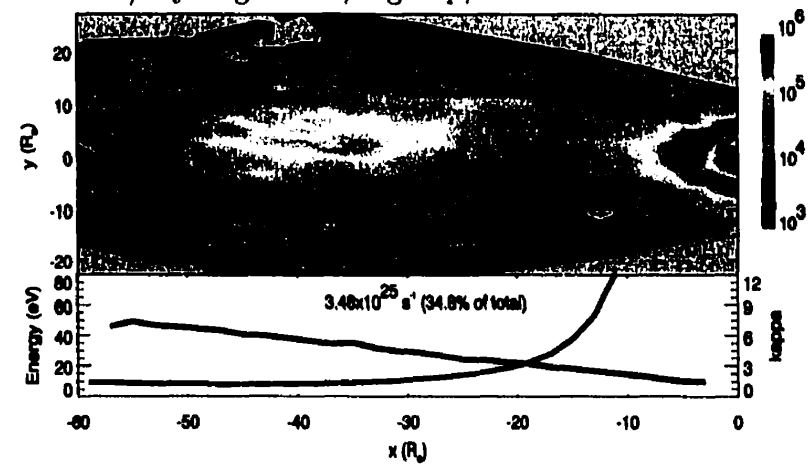
a) Hydrogen flux, low k_p , northward IMF.



b) Hydrogen flux, high k_p , northward IMF.

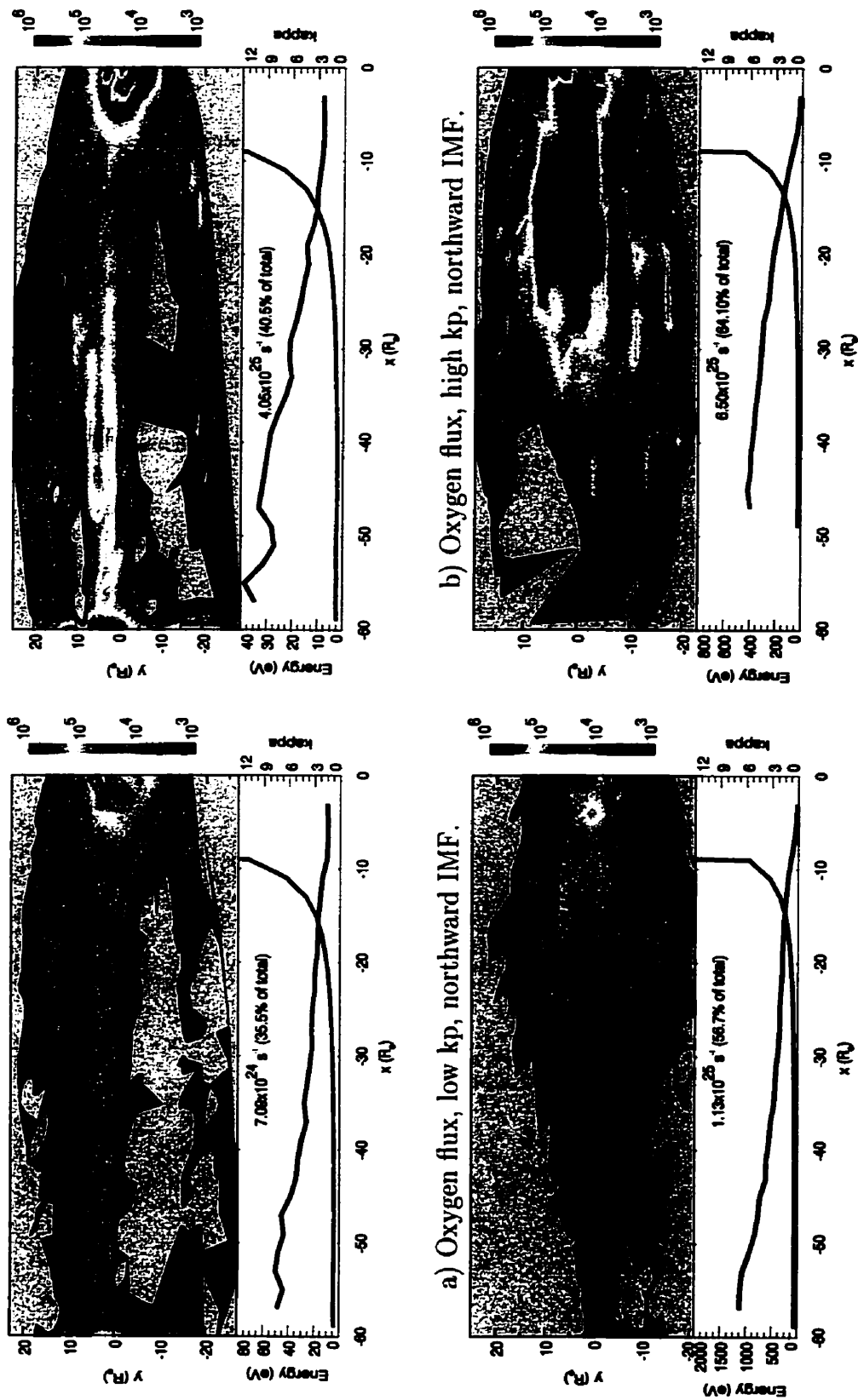


c) Hydrogen flux, low k_p , southward IMF.



d) Hydrogen flux, high k_p , southward IMF.

Figure 6.4: Supply of ionospheric H^+ to the CPS. Each colour contour plot shows the simulated flux of H^+ across the plasma sheet boundary. The line plots show the average energy and κ parameter of particles crossing the CPS near $y=0$. The black line shows the energy, while the other line is colour-coded for $\kappa > 3$ (blue) and $\kappa \leq 3$ (red).



a) Oxygen flux, low kp, northward IMF. b) Oxygen flux, high kp, northward IMF.
 c) Oxygen flux, low kp, southward IMF. d) Oxygen flux, high kp, southward IMF.

Figure 6.5: Supply of ionospheric O^+ to the CPS, in the same format as figure 6.4.

Typical values for the unidirectional flux are on the order 10^5 ions $\text{s}^{-1}\text{cm}^{-2}$. Although it is impossible to make a direct comparison, these numbers are generally consistent with the densities reported by Cladis and Francis [1992]. Typically, the total “available” flux (i.e. flux with $\kappa < 3$ that will interact non-adiabatically with the neutral sheet) represents 10% to 70% of the total unidirectional ionospheric outflow. Morphologically, slightly more flux is injected duskward of the noon-midnight meridian, a trend which is more pronounced with northward IMF. This is a consequence of the typically “twisted” electric potential at the ionosphere, which is reproduced in the Wiemer model (see, e.g., figure 6.1).

The largest differences between the four simulations are seen when comparing those with southward-oriented IMF to those with northward-oriented IMF. The difference is particularly striking for O^+ . *Both the flux and average energy of O^+ injected into the CPS earthward of $30 R_E$ are drastically higher for southward IMF as compared to northward.* This increased loading of the CPS is a result of the enhanced convection electric field leading to stronger centrifugal acceleration. The effect is only marginally seen for H^+ . This result may have important implications in the field of substorm triggering, and will be discussed in more detail in chapter 7.

Differences between periods of high and low K_p are much more subtle. There seems to be slightly less energization of the O^+ ions at higher K_p . This may be due to the greater magnetic field strength decreasing the $\vec{E} \times \vec{B}$ drift speed and thereby decreasing the centrifugal acceleration. Particles also generally encounter the CPS closer to the earth at lower K_p , consistent with the reasoning above.

Variation of the instantaneous flux in the model comes primarily through variation in the instantaneous ionospheric outflow rate, characterized in chapter 5. These

fluctuations are roughly an order of magnitude. Similar variation could be expected in the CPS supply rate. Individual satellite measurements will exhibit much larger variation, although it is beyond the scope of this study to characterize this.

Chapter 7

Discussion and Conclusions

7.1 Implications for Magnetospheric Dynamics

The results of the simulations show a substantial supply of ions from the ionosphere into the central plasma sheet. Some of these will be captured, some not. Of course, one could ask the question “is it really important to understand whether the CPS plasma comes from the ionosphere or the solar wind?” I suggest that the primary reason is this: in order to understand the behaviour of the CPS, it is critical to understand the behaviour of the systems that supply it with mass and energy, and the behaviour of the CPS is in turn of key importance to the dynamics of the magnetosphere.

7.1.1 Mass Budget: Is this an Important Plasma Population?

Chappel et al. [1987] suggested that the ionospheric outflow could fully supply the plasma for the magnetosphere, commenting in his conclusions that future research into this supply mechanism would need to elucidate “its strength, its composition, its energy, and its angular distributions.” Since then, it has become much more widely accepted that the ionosphere contributes a significant, and sometimes dominant, proportion of ions to the magnetosphere, at least in the near-earth regions [Moore and Delcourt, 1995; Daglis and Axford, 1996; Horwitz and Moore, 1997].

Delcourt et al. [1989] quantitatively modelled the ionospheric-source ions in a somewhat similar manner to the current work, although he allowed the particles to pass through the neutral sheet. The results showed clearly that not only was the ionosphere a major particle source, but that the energy densities of ionospheric ions in the neutral sheet were high enough to play an active role in instabilities in that region. Calculated velocities and densities are compatible with those reported here, as well as with an earlier study by [Peterson et al., 1981] demonstrating a substantial O^+ component of the CPS plasma, a clear indicator of ionospheric supply.

It is hardly surprising, then, that the current study indicates a substantial amount of ions entering the CPS. Typical fluences are on the order of 10^{25} s^{-1} for both H^+ and O^+ . Perhaps a more intuitive understanding of the magnitude of this fluence can be obtained by means of a crude estimate of the refilling time for the CPS. Assuming a CPS density of 2 cm^{-3} , a thickness of $5 R_E$ and an area of $800 R_E^2$, the total number of particles in the CPS is about 2×10^{30} . A typical supply rate of $4 \times 10^{25} \text{ s}^{-1}$ (10^{25} s^{-1} each for H^+ and O^+ , with 2 contributing hemispheres) would refill this amount in about 14 hours, assuming no leakage and that all of the flux is trapped (two very questionable assumptions). Observed refilling times after large storms are on the order of a few days. Clearly, this is an important factor in the mass budget of the magnetosphere.

7.1.2 Geophysical Dependencies: What Controls the Supply?

The simulations show a number of factors that control the supply of ionospheric ions to the CPS. These factors are:

1. *The solar EUV flux.* As $F_{10.7}$ increases, the number of O^+ ions leaving the

ionosphere increases by an order of magnitude, causing an order of magnitude increase in the O^+ flux at the CPS. There is also a much smaller increase in H^+ flux. This is in agreement with Lennartsson [1989], who examined the $F_{10.7}$ dependence of ions in the CPS directly by using data from the ISEE-1 satellite in the CPS, and found a significant increase in the O^+ / H^+ ratio as $F_{10.7}$ increased.

2. *The magnetic disturbance level*, as measured by either Kp or Dst. As the value of Kp increases from quiet time values to active time values, the flux of O^+ to the CPS increases by a factor of about 7. This is in agreement with in-situ measurements by Lennartsson et al. [1993], who also finds a factor of about 7.
3. *The solar wind dynamic pressure*. As the dynamic pressure increases, the ionospheric supply of both H^+ and O^+ also increases by a factor of about 4. The subsequent increase in the electric field was not modelled, although by comparing with traces where the electric field was increased due to IMF direction, it can be concluded that ion supply is increased as the dynamic pressure increases. This agrees with a third in-situ study of Lennartsson's, [Lennartsson, 1995].
4. *The solar wind orientation*. In contrast to the other effects in this list, the solar wind clock angle does not change the outflow rate from the ionosphere. However, the particle trajectories are modified in such a way that the flux across the surface of the CPS is moved closer to the Earth. At first this might seem to disagree with the results of Lennartsson [1995], who showed that the peak O^+ differential flux observed in-situ in the tail is not a function of IMF B_z .

However, Lennartsson's objective is to examine the ionospheric fluence, and not the unidirectional fluence at the CPS; these measurements have therefore been effectively averaged over a plane in the y - z direction. The conclusions are therefore identical: the ionospheric fluence is not a function of IMF B_z .

7.1.3 Dynamic Responses: Possible Substorm Connections

With a better understanding of the transport process, it is possible to address the issue of the response of the CPS to this input. In particular, an important issue is whether the ionospheric outflow could act as a substorm trigger.

Baker et al. [1982] have suggested that increased O^+ densities during active times could enhance the growth rate of the ion tearing mode instability, due to the larger gyroradius of O^+ relative to H^+ . This tearing mode instability could act as a substorm trigger.

Cladis and Francis [1992] proposed that, in response to increased parallel O^+ pressure, a large-scale inductive electric field could be set up opposing the convection electric field. Since O^+ injection into the CPS occurs only in a limited area, velocity shears would be set up along the flanks of the injection region. These regions could then drive velocity shear instabilities that could act as a substorm trigger.

Daglis et al. [1996] note that there is a strong correlation between the O^+ energy density in the near-earth tail and auroral electrojet activity during substorms. They propose the existence of fast, efficient ionospheric feeding of the near-earth tail in response to increased solar wind-magnetosphere coupling, which could in turn trigger an onset.

The issue of substorm triggering in response to ion flow conditions is beyond the

Distance (R_E)	O^+ (B_z North) $10^{24} s^{-1}$	O^+ (B_z South) $10^{24} s^{-1}$	H^+ (B_z North) $10^{24} s^{-1}$	H^+ (B_z South) $10^{24} s^{-1}$
-10	0.21	2.32	0.0	0.0
-15	0.67	6.75	0.0	0.0
-20	4.1	17.2	0.0	0.0
-25	6.7	22.8	0.07	2.0
-30	10.1	31.0	1.7	6.0
$-\infty$	40.4	63.1	19.7	34.8

Table 7.1: Effective CPS particle supply Earthward of the distances indicated.

scope of this study. The results shown in figures 6.4 and 6.5, however, beg certain questions.

7.1.4 A Conjecture

Substorms are inherently a nightside auroral latitude phenomenon. As such, the critical region to understand is the region between about $8 R_E$ and $30 R_E$. In the current disruption model [Lui, 1996], the inner to middle part of this region is where the current breakdown occurs. In the near-Earth neutral line model [Baker et al., 1996], the middle to outer part of this region is where the neutral line forms.

Table 7.1 summarizes the “effective” fluence in this region as a function of IMF B_z direction. Here, “effective” means only that $\kappa < 3$, implying nonadiabatic motion when the particles encounter the CPS. The data is the same as was used for figures 6.4 and 6.5, and is taken for disturbed ($K_p = 5$) conditions.

Consider the sequence of events of a “classic” externally-triggered substorm [Cann et al., 1977; Lyons, 1996]. In this well-studied case, the IMF is southward for a considerable period of time before turning abruptly northward. Immediately after

the northward turning, the substorm is triggered.

Using table 7.1, it can be seen that *the initial IMF southward period loads the critical region with O^+* . In-situ studies have shown that O^+ can become the dominant species in such conditions (98 % by mass in one example shown in Peterson et al. [1981]). With its larger gyroradius, it is likely that O^+ would be the dominant neutral sheet current carrier, even in less extreme examples.

The northward turning of the IMF would then shut off the supply of charge carriers to the critical region of the CPS. Although it is not shown, it seems possible that this could disrupt the cross-tail current system. At the very least, the withdrawal of the supply of carriers might force the system to reconfigure in such a way as to “pull in” carriers from other areas such as the more distant tail. Many believe that the disruption of the cross-tail current is the first stage in triggering a substorm (see Lui [1996] and references therein).

The typical reason why many do not believe ionospheric oxygen to be important for substorm dynamics is the issue of timing. It takes two to three hours for O^+ ions to travel from the ionosphere to the tail; substorm triggering happens in a few minutes. If the above scenario implied that the IMF turning reduced the ionospheric output, which then triggered the substorm when the supply in to the CPS was subsequently reduced, this would be a fatal flaw in the argument¹. In the above scenario, however, the ionospheric source strength stays constant; the *trajectories* change to reduce the flux at the CPS. The time delay between the IMF turning and the cutoff of the current carriers is then on the timescale of the change in the electric

¹Daglis and Axford [1996] proposes fast, efficient feeding of O^+ to the tail, but this requires time-dependent electrodynamic effects not considered in the present study.

field, which can occur in minutes.

This scenario is certainly speculative, and is meant to suggest future directions of research. Clearly, much more work would need to be done to evaluate whether this conjecture is even tenable.

7.2 Evaluation of the Source Model

7.2.1 Comparison with Other Reported Measurements

Given the low energy range of the SMS instrument, it is somewhat difficult to compare the observations to other estimates of fluence found in the literature. Additionally, fluences reported in the literature are typically net fluences, and often vary in order of magnitude from one publication to another.

The most direct comparison would be to the work of Abe et al. [1993] and Abe et al. [1996] (especially the latter). Both of these studies also use the SMS instrument in the declining period of $F_{10.7}$, although with a very different data analysis technique. The results of these studies are in good agreement with the results presented in chapter 5. Absolute net fluxes are similar to those reported herein, and the fluence trend with K_p is also similar (the net H^+ trend is slightly more pronounced in the current work). Different regional binning of the data combines with a large statistical uncertainty to make regional comparisons uncertain. Abe et al. [1996] reports a trend associated with IMF B_z , which is in disagreement with the results above. The scatter of the data points in figure 3b of that paper raises some questions regarding the statistical significance of the trend, which is an issue not addressed in that paper.

Two other studies that find similar fluences are Yau et al. [1985] and Collin et al. [1989] (the latter is referenced in Peterson et al. [2001]; see also Collin et al. [1984]). Both of these studies, using data from the DE 1 satellite, give expressions for fluence as a function of K_p and $F_{10.7}$ which can be compared to equations 5.4. Agreement is generally good. Collin et al. [1984] find a similar dependence on K_p , although a significantly higher overall O^+ flux and less $F_{10.7}$ dependence. H^+ results are nearly identical. Yau et al. [1985] also find a smaller $F_{10.7}$ dependence, and still higher overall O^+ fluences. Estimated H^+ fluences are also slightly higher. It should be noted that the DE 1 energy range is from about 10 eV to 17 keV, which makes the comparison less meaningful.

Peterson et al. [2001] reports recent results from the POLAR spacecraft showing significantly lower fluxes of both H^+ and O^+ than previous results. Their O^+ results are quite compatible with my results, while my H^+ fluences are more similar to those reported by Yau et al. [1985] and Collin et al. [1989]. The POLAR orbit is somewhat more suitable for studies of seasonal effects. H^+ and O^+ are reported to have summer/winter ratios of 0.9 and 1.0 respectively, which are within the error bars of my results.

Norqvist et al. [1998] reports upward O^+ fluences observed from the Freja spacecraft in the declining phase of the solar cycle in a paper devoted to examining the sources of the outflow. The energy range was more suitable to comparison with the current results: 1 eV to 4.3 keV. The altitude was much lower, however: around 1700 km. The integrated fluence results agree for intermediate K_p , although the reported influence of K_p is more dramatic than the K_p dependence seen in the other papers. The K_p dependence reported here agrees more closely with the other papers.

7.2.2 Strengths and Weaknesses

The main strength of the outflow model (see chapters 4 and 5) is that it includes an estimate of instantaneous variability of the fluence, which is something that has never before been attempted. The modification of the bin sizes and locations by K_p is an improvement on static binning, allowing more meaningful comparisons of regional distribution. The statistical analysis of the geophysical dependencies has been performed with improved error estimation, which has removed ambiguities in the interpretation of trends (notably trends with IMF direction). In contrast with other studies done using SMS data, it does not assume a Maxwellian distribution, removing an assumption that is often invalid, but introducing other problems.

The most obvious weakness in the source model is that the cell size determination is important to the results and difficult. It is uncertain whether the scheme used to find the cells is appropriate. The Monte Carlo model for the outflow is crude, and likely does not incorporate some dependencies that exist in the data. The removal of the assumption of a Maxwellian distribution also comes at a cost, which is that the flux integration may underestimate the low energy contribution². It is also difficult to deal with instrument response and spacecraft charging at low energies. The angular resolution of the instrument is low, which introduces uncertainties in the integration over pitch angle space. Finally, the uncertainties in the absolute calibration are significant, and almost certainly drift in time in a way not entirely captured by the MCP calibration.

²Note that this is not a problem for estimation of ion supply to the CPS, as these ions would almost certainly be gravitationally trapped anyway.

7.3 Evaluation of the Tracing Model

7.3.1 Comparison with Other Reported Results

The design of the tracing simulations differs in a critical way from all similar studies: the traces are stopped when the ion is about to enter the CPS. Perhaps the closest comparison is with the work of Delcourt et al. [1989], who traced the 3-dimensional ion trajectories with the full guiding centre equations of motion in the magnetic model of Mead and Fairfield [1975] and the electric potential model of Volland [1978]. Particles were allowed to travel through the current sheet and bounce at the conjugate hemisphere. The derived ion energies and densities are not inconsistent with either observation or the current work.

7.3.2 Strengths and Weaknesses

I would consider the main strength of the model to be the termination of the traces immediately before the Plasma Sheet Boundary Layer. This neatly divides the problem into discrete pieces that can reasonably be assessed, rather than dealing with the problem monolithically.

The model cannot account for wave/particle interactions or parallel electric fields. In some sense, this is a weakness, as these are certainly important. On the other hand, it is always useful to understand the “zeroth-order” solution, which in some sense is what this provides. A similar criticism is that the model is not self-consistent; the particles influence the fields in which they travel.

The primary weakness of the model is its reliance on statistical empirical models of the electric and magnetic fields. While valid in some sense as a time average of the

field configuration, it is debateable whether the instantaneous fields through which the particles are moving *ever* resemble the Tsyganenko [1987] and Weimer [1995] field models used. The $\vec{\mathbf{E}} \times \vec{\mathbf{B}}$ drift is perhaps not well characterized by the average fields: $\langle \vec{\mathbf{E}} \times \vec{\mathbf{B}} \rangle \neq \langle \vec{\mathbf{E}} \rangle \times \langle \vec{\mathbf{B}} \rangle$. Additionally, both models are poor in the cusp region, which is a critical region for O^+ energization . Another weakness is that the gridding of the electric field prior to simulation, while computationally efficient, is perhaps questionable.

7.4 Main Conclusions

The primary contributions of this thesis to the field of space physics are:

1. The elucidation of the IMF control of the ionospheric contribution to the plasma sheet. Specifically, the increased flux near $15 R_E$ under southward IMF is a potentially important result.
2. The description of the response of the ionosphere to changing solar wind conditions is important, and was identified as a key issue in the definitive review papers of André and Yau [1997] and Yau and André [1997]. The null result of relation with IMF clock angle is important, as is the positive correlation with both solar wind ram pressure and solar wind magnetic pressure.
3. The assessment of the variability of the instantaneous ionospheric fluence has never before been done, and begins to answer the question of whether the average outflow rates given both herein and elsewhere in the literature are meaningful.

4. The maps of flux into the CPS given in figures 6.4 and 6.5 are useful for questions of total mass budget. The integrated fluences are also useful.
5. The ionospheric outflow measurements offer another independent measurement of total O^+ fluence. The total fluence estimates given herein are typically intermediate between the higher fluences seen on DE 1 and the lower fluences seen on Freja and POLAR.
6. The study generally validates the K_p , $F_{10.7}$ and Dst dependencies seen on DE 1 and POLAR.
7. The outflow estimates act as a good complement to the work of Abe et al. [1996] by estimating fluxes in a completely different manner using a somewhat expanded data set from the same instrument.
8. The seasonal dependencies of the ion fluences are explored. Little correlation is found.

7.5 Directions for Further Study

There are several directions for further study. A few questions immediately arise:

1. Can a better understanding be reached of the self-organizing cellular features seen in the data?
2. What are the source mechanisms for the statistical outflow (see André and Yau [1997]; Norqvist et al. [1998])? What is the relation of this to the first question?

3. How can the various satellite measurements of flux be reconciled?
4. Are the CPS fluxes still seen in a more self-consistent model (see Ashour-Abdalla et al. [1998] for an example of particle tracing in time-dependent situations with MHD inputs)?
5. Can the effects of field line “sloshing”, whereby field lines are allowed to move under pseudo-random electric field perturbations, be included? Does this offer a significant source of energy? Is it comparable to the centrifugal acceleration?
6. Can the particle motion through the cusp be effectively modelled (see Delcourt et al. [1994])?
7. What happens to the particles when they hit the neutral sheet (see Delcourt and Belmont [1998])?
8. Does the conjecture of section 7.1.4 hold up under closer scrutiny?
9. More generally, what is the role of ionospheric oxygen in the substorm and storm cycles?

The foundations of this work are a careful statistical analysis of the ionospheric fluence and a simple but reasonable model for transporting these ions to the CPS, *and no further*. This constitutes an interesting framework for ionosphere-CPS interaction, with which it may be possible to explain a key step in the complicated process of substorm triggering. Whether or not this conjecture holds up under closer scrutiny cannot be addressed at this time; however, the fact that such an issue can be raised at all illustrates the utility of the fundamental philosophy underlying the study: *with*

a careful framework, one can address complex problems using simple tools. It is my hope that the simple structure and results of this thesis may prove useful in the complex field of space physics.

Bibliography

- T. Abe, S. Watanabe, B. A. Whalen, A. W. Yau, and E. Sagawa. Observations of polar wind and thermal ion outflow by Akebono/SMS. *J. Geomag. Geoelectr.*, 48: 319–325, 1996.
- T. Abe, B.A. Whalen, A.W. Yau, R.E. Horita, S. Watanabe, and E. Sagawa. EXOS-D (Akebono) SMS observations of the polar wind. *J. Geophys. Res.*, 98:11,191–11,203, 1993.
- H. Alfvén. *Cosmical Electrodynamics*. Clarendon Press, Oxford, 1950.
- M. André and A.W. Yau. Theories and observations of ion energization and outflow in the high latitude magnetosphere. *Space Sci. Rev.*, 80:27–48, 1997.
- M. Ashour-Abdalla, J. Raeder, M. El-Alaoui, and V. Perroomian. Magnetotail structure and its internal particle dynamics during northward IMF. In A. Nishida, D. N. Baker, and S. W. H. Cowley, editors, *New Perspectives on the Earth's Magnetotail*, Geophys. Monogr. Ser., vol. 105, pages 77–95, Washington, D. C., 1998. AGU.
- W. I. Axford. The polar wind and the terrestrial helium budget. *J. Geophys. Res.*, 73:6855–6859, 1968.
- D. N. Baker, E. W. Hones, D. T. Young, and J. Birn. The possible role of ionospheric oxygen in the initiation and development of plasma sheet instabilities. *Geophys. Res. Lett.*, 9:1337–1340, 1982.

- D. N. Baker, T. I. Pulkkinen, V. Angelopoulos, W. Baumjohann, and R. L. McPherron. Neutral line model of substorms: Past results and present view. *J. Geophys. Res.*, 101:12975–13010, 1996.
- K. B. Baker and S. Wing. A new magnetic coordinate system for conjugate studies at high latitudes. *J. Geophys. Res.*, 94:9139–9143, 1989.
- W. Baumjohann and R. A. Treumann. Trapping conditions for energetic particles incident on a tangential discontinuity surface. *Planet. Space. Sci.*, 35(4):483–5, 1987.
- W. H. Bennet. Radio frequency mass spectrometer. *J. Appl. Phys.*, 21:143, 1950.
- P. R. Bevington and D. K. Robinson. *Data reduction and error analysis for the physical sciences*. McGraw-Hill, 2 edition, 1992.
- L. Biermann. Kometenschweife und solare korpuskular-strahlung. *Zs. F. Astrophys*, 29:274–286, 1951. Reference to this paper is based on a review of solar wind physics by A. J. Dessler in *Physics of the Magnetosphere*, Edited by Carovillano, McClay, and Radoski. Springer Verlag, 1967.
- J. E. Borovsky, M. F. Thomsen, and R. C. Elphic. The driving of the plasma sheet by the solar wind. *J. Geophys. Res.*, 103:17617–17639, 1998.
- J. Büchner and L. M. Zelenyi. Deterministic chaos in the dynamics of charged particles near a magnetic field reversal. *J. Geophys. Res.*, 92:13456, 1986.
- M. N. Cann, R. L. McPherron, and C. T. Russell. Characteristics of the association

- between the interplanetary magnetic field and substorms. *J. Geophys. Res.*, 82: 4837, 1977.
- Chapman and Ferraro. A new theory of magnetic storms. *Nature*, 126(3169):129–130, 1932.
- C. R. Chappel, T. E. Moore, and J. H. Waite, Jr. The ionosphere as a fully adequate source of plasma for the earth's magnetosphere. *J. Geophys. Res.*, 92:5896–5910, 1987.
- F. F. Chen. *Introduction to Plasma Physics and Controlled Fusion*, volume 1. Plenum Press, New York, 2 edition, 1984.
- J. B. Cladis. Parallel acceleration and transport of ions from polar ionosphere to plasma sheet. *Geophys. Res. Lett.*, 13:893–896, 1986.
- J. B. Cladis and W. E. Francis. Distribution in magnetotail of O⁺ ions from cusp/cleft ionosphere: A possible substorm trigger. *J. Geophys. Res.*, 97:123–130, 1992.
- H. L. Collin, W. K. Peterson, A. W. Yau, and E. G. Shelley. An empirical model of ionospheric ion output as a function of solar EUV and magnetospheric activity. Paper presented at IAGA meeting, International Association of Geomagnetism and Aeronomy, Exeter, U. K., 1989.
- H.L. Collin, R.D. Sharp, and E.G. Shelley. The magnitude and composition of the outflow of energetic ions from the ionosphere. *J. Geophys. Res.*, 89:2185–2194, 1984.

- C. M. Cully and E. F. Donovan. A derivation of the gradient (∇b) drift based on energy conservation. *Am. J. Phys.*, 67(10):909–11, 1999.
- I. A. Daglis and W. I. Axford. Fast ionospheric response to enhanced activity in geospace: Ion feeding of the inner magnetotail. *J. Geophys. Res.*, 101:5047–5065, March 1996.
- I. A. Daglis, W. I. Axford, S. Livi, B. Wilken, M. Grande, and F. Søråas. Auroral ionospheric ion feeding of the inner plasma sheet during substorms. *J. Geomagn. Geoelectr.*, 48:729, 1996.
- D. C. Delcourt. Centrifugal effects near the frontside magnetopause. *J. Geophys. Res.*, 99:8585–8591, 1994.
- D. C. Delcourt and G. Belmont. Particle dynamics in the near-earth magnetotail and macroscopic consequences. In A. Nishida, D. N. Baker, and S. W. H. Cowley, editors, *New Perspectives on the Earth's Magnetotail*, Geophys. Monogr. Ser., vol. 105, pages 193–210, Washington, D. C., 1998. AGU.
- D. C. Delcourt, C. R. Chappell, T. E. Moore, and J. H. Waite, Jr. A three-dimensional numerical model of ionospheric plasma in the magnetosphere. *J. Geophys. Res.*, 94:11893–11920, 1989.
- D. C. Delcourt, T. E. Moore, J. A. Sauvad, and C. R. Chappel. Nonadiabatic transport features in the outer cusp region. *J. Geophys. Res.*, 99:5681–5689, 1994.
- E. F. Donovan. *Modelling distributed magnetospheric currents*. Phd thesis, U. Alberta, 1993.

- E. Drakou, A.W. Yau, and T. Abe. Ion temperature measurements from the Akebono suprathermal mass spectrometer: Application to the polar wind. *J. Geophys. Res.*, 102:17,523–17,539, 1997.
- B. Efron. Bootstrap methods: Another look at the jackknife. *Ann. Statist.*, 7:1–26, 1979.
- B. Efron and R. J. Tibshirani. *An Introduction to the Bootstrap*. Chapman & Hall, London, 1993.
- T. Gold. Motions in the magnetosphere of the earth. *J. Geophys. Res.*, 64:1219–1224, 1959.
- H. Goldstein. *Classical Mechanics, 2nd ed.* Addison-Wesley, Reading, Massachusetts, 1980.
- P. Hall and R. L. Smith. The kernel method for unfolding sphere size distributions. *J. Comput. Phys.*, 74:409–421, 1988.
- J. S. Urban Hjorth. *Computer Intensive Statistical Methods*. Chapman & Hall, London, 1994.
- C. Hoffmeister. *Zs. F. Astrophys.*, 23:265, 1943.
- J. L. Horwitz and T. E. Moore. Four contemporary issues concerning ionospheric plasma flow to the magnetosphere. *Space Sci. Rev.*, 80:49–76, 1997.
- J. D. Jackson. *Classical Electrodynamics, 2nd ed.* John Wiley & Sons, New York, 1975.

- M. C. Kelley. *The Earth's Ionosphere*. Academic Press, San Diego, 1989.
- M. Kruskal. Advanced theory of gyrating particles. In *Plasma Physics, Lectures Presented at the Seminar on Plasma Physics Organized by and Held at the International Center for Theoretical Physics, Trieste from 5 - 31 October 1964*, pages 91–102, Vienna, 1965a. IAEA.
- M. Kruskal. Elementary orbit and drift theory. In *Plasma Physics, Lectures Presented at the Seminar on Plasma Physics Organized by and Held at the International Center for Theoretical Physics, Trieste from 5 - 31 October 1964*, pages 67–90, Vienna, 1965b. IAEA.
- H. R. Künsch. The jackknife and the bootstrap for general stationary observations. *Ann. Statist.*, 17:1217–1241, 1989.
- S. M. Lea and J. R. Burke. *Physics: The Nature of Things*. Brooks/Cole Publishing, Pacific Grove, 1997.
- O. W. Lennartsson. Statistical investigation of IMF B_z effects on energetic (0.1 to 16-keV/e) magnetospheric O^+ ions. *J. Geophys. Res.*, 100:23621–23635, 1995.
- O. W. Lennartsson, D. M. Klumpar, E. G. Shelley, and J. M. Quinn. Experimental investigation of possible geomagnetic feedback from energetic (0.1 to 16-keV/e) terrestrial O^+ ions in the magnetotail current sheet. *J. Geophys. Res.*, 98:19443–19454, 1993.
- W. Lennartsson. Energetic (0.1 to 16-keV/e) magnetospheric ion composition at different levels of solar $F_{10.7}$. *J. Geophys. Res.*, 94:3600–3610, 1989.

- A. T. Y. Lui. Road map to magnetotail domains. In A. T. Y. Lui, editor, *Magnetotail Physics*, pages 3–9. Johns Hopkins University Press, 1987.
- A. T. Y. Lui. Radial profiles of quiet time magnetospheric parameters. *J. Geophys. Res.*, 97:19325–19332, 1992.
- A. T. Y. Lui. Current disruption in the earth's magnetosphere: Observations and models. *J. Geophys. Res.*, 101:13067–13088, 1996.
- L. R. Lyons. Substorms: Fundamental observational features, distinction from other disturbances, and external triggering. *J. Geophys. Res.*, 101:13011–13025, 1996.
- D. W. Marquardt. An algorithm for least-squares estimation of nonlinear parameters. *J. Soc. Ind. Appl. Math.*, 11(2):431–441, 1963.
- G. D. Mead and D. H. Fairfield. A quantitative magnetospheric model derived from spacecraft magnetometer data. *J. Geophys. Res.*, 80:523, 1975.
- T. E. Moore and D. C. Delcourt. The geopause. *Rev. Geophys.*, 33(2):175–209, May 1995.
- D. R. Nicholson. *Introduction to Plasma Theory*. John Wiley & Sons, New York, 1983.
- P. Norqvist, M. André, and M. Tyrland. A statistical study of ion energization mechanisms in the auroral region. *J. Geophys. Res.*, 103:23459–73, 1998.
- T. G. Northrop. *The Adiabatic Motion of Charged Particles*. Wiley-Interscience, New York, 1963.

- E. N. Parker. Interaction of the solar wind with the geomagnetic field. *Phys. Fluids*, 1:171–187, 1958.
- W. K. Peterson, H. L. Collin, A. W. Yau, and O. W. Lennartsson. Polar/toroidal imaging mass-angle spectrograph observations of suprathermal ion outflow during solar minimum conditions. *J. Geophys. Res.*, 106:6059–6066, 2001.
- W. K. Peterson, R. D. Sharp, E. G. Shelley, and R. G. Johnson. Energetic ion composition of the plasma sheet. *J. Geophys. Res.*, 86:761–767, 1981.
- W. H. Press, S. A. Teukolsky, W. T. Vetterling, and B. P. Flannery. *Numerical Recipes in C : The Art of Scientific Computing*. Cambridge University Press, 1993.
- H. Rishbeth and O. K. Garriott. *Introduction to Physics of the Ionosphere*. Academic Press, New York, 1969.
- G. Rostoker. Geomagnetic indices. *Rev. Geophys. and Space Phys.*, 10:935–950, 1972.
- R. D. Sharp, W. Lennartsson, W. K. Peterson, and E. G. Shelley. The origins of the plasma in the distant plasma sheet. *J. Geophys. Res.*, 87:10420, 1982.
- E. G. Shelley, R. G. Johnson, and R. D. Sharp. Satellite observations of energetic heavy ions during a geomagnetic storm. *J. Geophys. Res.*, 77:6104, 1972.
- J. Stoer and R. Bulirsch. *Introduction to Numerical Analysis, second edition*. Springer-Verlag, New York, 1993.

- K. Tsuruda and H. Oya. Introduction to the EXOS-D (Akebono) project. *J. Geophys. Res.*, 98:11123–11125, 1993.
- N. A. Tsyganenko. Global quantitative models of the geomagnetic field in the cislunar magnetosphere for different disturbance levels. *Planet. Space Sci.*, 35:1347–1358, 1987.
- E. Ungstrup, D. M. Klumpar, and W. J. Heikkila. Heating of ions to superthermal energies in the topside ionosphere by electrostatic ion cyclotron waves. *J. Geophys. Res.*, 84:4289–4296, 1979.
- H. Volland. A model of the magnetospheric electric convection. *J. Geophys. Res.*, 83:2695, 1978.
- D. R. Weimer. Models of high-latitude electric potentials derived with a least error fit of spherical harmonic coefficients. *J. Geophys. Res.*, 100:19595–19607, 1995.
- B.A. Whalen, J.R. Burrows, A.W. Yau, E.E. Budzinski, A.M. Pilon, I. Iwamoto, K. Marubashi, S. Watanabe, H. Mori, and E. Sagawa. The Suprathermal Ion Mass Spectrometer (SMS) onboard the Akebono (EXOS-D) satellite. *J. Geomag. Geoelectr.*, 42:511–536, 1990.
- S. D. Wicksell. The corpuscle problem. *Biometrika*, 17:84–99, 1925.
- A.W. Yau and M. André. Sources of ion outflow in the high latitude ionosphere. *Space Sci. Rev.*, 80:1–25, 1997.
- A.W. Yau, E. Drakou, M.J. Greffen, D.J. Knudsen, and E. Sagawa. Radio-frequency ion mass spectrometer measurements of ion composition, velocity and temper-

ature: the EXOS-D suprathermal mass spectrometer. *Geophys. Monogr.*, 102: 307–312, 1998.

A.W. Yau, E.G. Shelley, W.K. Peterson, and L. Lenchyshyn. Energetic auroral and polar ion outflow at DE 1 altitudes: magnitude, composition, magnetic activity dependence, and long-term variations. *J. Geophys. Res.*, 90:8417–8432, 1985.